Étude par microscopie électronique et spectroscopie de films minces catalytiques pour micro piles à combustibles

Jaroslava Lavková

UNIVERSITE DE BOURGOGNE

&

CHARLES UNIVERSITY IN PRAGUE

UFR Sciences et Technique Mirande, Laboratoire Interdisciplinaire Carnot de Bourgogne, Ecole doctorale Carnot-Pasteur

&

Department of Surface and Plasma Science, Faculty of Mathematics and Physics

THÈSE

Pour obtenir le grade de

Docteur de l'Université de Bourgogne

Discipline: Chimie-Physique

par

Jaroslava Lavková

le 27/05/2016

Electron Microscopy and Spectroscopy Study of Nanostructured Thin Film Catalysts for Micro-fuel Cell Application

Directeur de thèse

Valerie Potin

Iva Matolínová

To Margarétka Datková..

Acknowledgment

First of all I am very grateful to my supervisors Valerie Potin and Iva Matolínová for their guidance, motivating discussion and helpful advices during my study. I appreciate their effort on international cooperation and coordination of the present cotutelle thesis.

I would like to thank all my colleagues from Surface Science group and Nano/SIOM team for receiving me into very friendly and helpful working environment. Special thanks to Ivan Khalakhan, Martin Dubau, Agnès Birot, Sylvie Bourgeois and Vladimír Matolín.

Last but not least, thanks belong to my family and dearest, especially to Martin, as I appreciate his support and patience during my studies.

I declare that I carried out this doctoral thesis independently, and only with the cited sources, literature and other professional sources.

I understand that my work relates to the rights and obligations under the Act No. 121/2000 Coll., the Copyright Act, as amended, in particular the fact that the Charles University in Prague has the right to conclude a license agreement on the use of this work as a school work pursuant to Section 60 paragraph 1 of the Copyright Act.

In Prague, 1.4.2016 Jaroslava Lavková

Abstract

Present doctoral thesis is focused on investigation of novel metal-oxide anode catalyst for fuel cell application by electron microscopy and associated spectroscopies. Catalysts based on Pt-doped cerium oxide in form of thin layers prepared by simultaneous magnetron sputtering deposition on intermediate carbonaceous films grown on silicon substrate have been studied. The influence of the catalyst support composition (a-C and CN_x films), deposition time of CeO_x layer and other deposition parameters, as deposition rate, composition of working atmosphere and Pt concentration on the morphology of Pt-CeO_x layers has been investigated mainly by Transmission Electron Microscopy (TEM). The obtained results have shown that by combination of suitable preparation conditions we are able to tune the final morphology and composition of the catalysts. The composition of carbonaceous films and Pt-CeO_x layers was examined by complementary spectroscopy techniques – Energy Dispersive X-ray Spectroscopy (EDX), Electron Energy Loss Spectroscopy (EELS) and X-ray Photoelectron Spectroscopy (XPS). Such prepared porous structures of Pt-CeO_x are promising as anode catalytic material for real fuel cell application.

Keywords: cerium oxide, platinum, fuel cell, magnetron sputtering, Transmission Electron Microscopy

Abstrakt

Předložená dizertační práce se zabývá studiem nových katalyzátorů na bázi kov-oxid vhodných pro použití v palivových článcích na straně anody. Platinou dopovaný oxid ceru připravený magnetronovým naprašováním ve formě tenkých vrstev na uhlíkových mezivrstvách nesených křemíkovým substrátem byl zkoumán prostřednictvím mikroskopických a spektroskopických metod. Vliv složení uhlíkového nosiče (a-C a CN_x filmy), depozičního času CeO_x vrstvy a dalších depozičních parametrů, např. depoziční rychlosti, složení pracovní atmosféry a Pt koncentrace na morfologii Pt-CeO_x vrstev byl studován převážně pomocí transmisní elektronové mikroskopie (TEM). Získané výsledky ukazují, že vhodnou kombinací depozičních podmínek jsme schopni vyladit výslednou morfologii a kompozici katalyzátoru. Složení uhlíkových filmů a Pt-CeO_x vrstev bylo studováno spektroskopickými technikami – energiově-disperzní spektroskopií (EDX), spektroskopií charakteristických ztrát elektronů (EELS) a rentgenovou fotoelektronovou spektroskopií (XPS). Takto připravené porézní struktury vrstev Pt-CeO_x jsou slibným katalytickým materiálem na straně anody pro reálné aplikace v palivových článcích.

Klíčové slova: cer oxid, platina, palivové články, magnetronové naprašování, transmisní elektronový mikroskop

Résumé

Les piles à membrane polymère à échange de protons (PEMFC) sont une des techniques les plus prometteuses pour une production d'électricité propre et efficace à partir d'hydrogène. Les applications de cette nouvelle génération de piles à combustibles concernent aussi bien des applications portables et nomades telles que smartphones, ordinateurs portables, électronique embarquée que des applications domestiques ou dans les transports. A ce jour, le platine utilisé comme catalyseur est considéré comme le seul choix possible pour un rendement élevé et stable. En conséquence, suite à des ressources limitées en platine, la fabrication des piles à combustible reste coûteuse et la production industrielle généralisée impossible. Pour cette raison, une diminution substantielle de la quantité de Pt incorporée et donc la recherche de nouveaux matériaux d'anode à faible coût avec une activité élevée sont nécessaires. Des systèmes à base d'oxyde de cérium dopés au platine avaient été présentés comme étant des catalyseurs actifs pour l'oxydation du CO, la production d'hydrogène, l'oxydation de l'éthanol et la décomposition de méthanol. Au cours de ce travail, de nouveaux concepts pour la fabrication des piles à combustible ont été développés : la quantité de platine incorporée a été fortement diminuée conduisant à la production de nouveaux matériaux d'anode. Enfin, des catalyseurs à base de platine ont été déposés non pas sous la forme usuelle de nanopoudres mais sous forme de films minces fortement poreux sur substrat silicium.

Au cours de cette thèse, le système Pt-CeO_x a été étudié. Des échantillons non dopés puis dopés avec une faible quantité de platine ont été élaborés puis caractérisés en vue d'une application comme catalyseurs pour piles à combustibles. L'obtention de ces matériaux avec des propriétés sur mesure implique la maîtrise totale de leurs conditions de croissance. Afin d'étudier ces nouveaux composés de taille nanométrique, la microscopie électronique en transmission (MET) a été un outil précieux, qui a permis d'apporter des informations très précises sur la morphologie des films minces, la composition chimique et la structure à l'échelle atomique. Le cérium possède un double degré d'oxydation (+III/+IV), ce qui explique ses très bonnes propriétés catalytiques. Des analyses par spectrométrie de

photoélectrons X (XPS) ainsi que par spectroscopie de pertes d'énergie des électrons (EELS) ont été effectuées afin de déterminer son degré d'oxydation.

Le premier chapitre de la thèse présente l'état de l'art concernant les piles à combustibles de type PEMFC, leurs principaux avantages et limitations. Un descriptif des principaux catalyseurs ainsi que de leurs supports est réalisé.

Le deuxième chapitre de la thèse présente la méthode de pulvérisation cathodique magnétron utilisée pour l'élaboration des films minces. Ce chapitre est aussi dédié aux méthodes de caractérisation utilisées ainsi qu'aux détails techniques des conditions opératoires. Outre les conditions d'élaboration et de préparation des échantillons, il est principalement axé sur les microscopies électroniques à balayage et en transmission et sur les techniques spectroscopiques que sont la spectroscopie dispersive en énergie de rayons X, la spectroscopie de pertes d'énergie des électrons et la spectrométrie de photoélectrons X.

Le troisième chapitre consacré aux résultats ainsi qu'à leur discussion est divisé en quatre parties. La première partie s'intéresse à différents types de support du catalyseur : substrat de silicium, feuillet de carbone, couches intermédiaires de carbone amorphe pur ou azoté. Différents échantillons ont été élaborés sur ces substrats sous forme de couches minces; l'objectif étant d'augmenter la surface spécifique du dépôt afin d'augmenter sa réactivité. Ces échantillons ont été caractérisés par microscopie électronique et leur morphologie a été particulièrement étudiée en lien avec les conditions d'élaboration. Le film mince élaboré sur substrat silicium peut présenter un caractère poreux dans des conditions d'élaboration spécifiques; en particulier, quand une couche intermédiaire de carbone ou de CN_x amorphe est insérée. De plus, il est possible de contrôler la morphologie du dépôt en maitrisant les paramètres d'élaboration. En fait, la morphologie variée observée résulte de deux phénomènes simultanés : d'une part, l'attaque du substrat intermédiaire de carbone par le plasma d'oxygène et d'autre part, le dépôt de l'oxyde de cérium dopé platine

La deuxième partie de ce chapitre porte sur la caractérisation des films minces de CeO_x déposés sur les différents supports présentés précédemment. Une étude cristallographique a été menée, mettant en évidence outre la présence majoritaire de la structure fluorite de CeO_2, la présence de différentes structures telles que Ce_7O_{12} et CeC_2. Ces films minces de CeO_x ont été caractérisés par

spectroscopie de pertes d'énergie des électrons et par spectrométrie de photoélectrons X afin de déterminer en particulier le degré d'oxydation du cérium. Dans le cas d'un dépôt d'oxyde de cérium réalisé sur un substrat de silicium recouvert d'une couche intermédiaire de carbone, le traitement des spectres EELS indique que le cérium se trouve majoritairement sous forme Ce^{4+} excepté à la surface et à l'interface avec le substrat de carbone où il est observé sous forme Ce^{3+}. Ces résultats sont en excellent accord et complètent les résultats obtenus par XPS.

La troisième partie porte sur l'étude du catalyseur constitué par des films minces de CeO_x dopé platine. L'influence de la concentration en platine sur la morphologie, la cristallographie et la structure électronique des dépôts est étudiée et discutée. Le caractère poreux des films est confirmé en utilisant une couche intermédiaire de carbone amorphe et/ou de CN_x ainsi qu'en contrôlant les paramètres d'élaboration. Au début du processus d'élaboration, une faible quantité de (Pt-)CeO_x est déposée et l'attaque du substrat par le plasma d'oxygène est le procédé dominant. Il y a ensuite croissance des grains de (Pt-)CeO_x qui protègent partiellement la surface du substrat et une structure de type "cheminée de fée" peut être obtenue. Une étude cristallographique des couches minces de Pt-CeO_x a mis en évidence par microscopie électronique haute résolution outre les structures précédentes la présence de multiples composés à base de Ce-O-Pt (Pt, PtO_2, $CePt_2$, $CePt_5$). La composition élémentaire des couches ainsi que leur structure électronique ont été étudiées par EDX et XPS.

Enfin, en vue d'une application comme anode, pour piles à combustible, les films minces ont été déposés par pulvérisation cathodique exactement dans les mêmes conditions sur un substrat spécifique de nano-GDL. De façon similaire, leur morphologie est caractérisée par une importante surface spécifique, obtenue grâce à l'adjonction des couches intermédiaires de carbone et CN_x. La présence de cette importante surface réactionnelle est particulièrement prometteuse en vue d'une application comme catalyseurs pour PEMFC.

Mots clefs : Oxyde de cérium, platine, pile à combustible, pulvérisation cathodique magnétron, microscopie électronique en transmission

Table of Contents

Introduction

One of recent trends in renewable energy investment is the development of new energetic systems using hydrogen; well known as hydrogen economy. Fuel cell technology based on hydrogen offers clean, efficient and reliable power generation and it can be used in wide range of portable, stationary and transport applications, from battery chargers to home heating and power to cars. One of the main advantages is the replacement of fossil fuel and thus, emission of pollutants decrease. Arguably, fuel cells represent the most versatile energy solution ever invented.

With a wide-spreading popularity of portable devices and their miniaturization, the demand for a high-density power source is increasing. To satisfy this demand, micro-fuel cell devices (μ-FC) may have sufficient potential to replace existing batteries whose energy capabilities are limited by the amount of stored chemicals. Moreover, the fuel cell efficiency is higher at smaller scales. However, the system cost is still a big limitation, as efficient but costly catalyst material, platinum, is required. Platinum (Pt) is the versatile element used in catalysis that efficiently mediates a multitude of chemical reactions. Unfortunately, Pt is a rare element and its high price, exceeding that of gold, limits large-scale applications. Therefore, not surprisingly, the goal of reducing the amount of Pt is the major driving force in the catalysis research.

One of the very promising alternate materials is cerium oxide (CeO_x), which has recently been gaining a lot of research attention. Cerium oxide is valued for its high oxygen storage capacity, i.e. ability to easily release, store or transport oxygen accompanied by transition between two stable states, Ce^{3+} and Ce^{4+}, and for its ability to enhance the activity of transient metal and metal oxide catalysts.

In addition to a high efficiency of the catalyst material, it is also necessary to ensure the highest specific surface area of the catalyst. The size, structure and morphology of the catalyst surface depend mainly on the methods and parameters of its preparation, as well as on the chosen substrate. Carbon has been proven to be a suitable catalyst carrier. Due to their superior electrical and physical properties,

carbon materials are of interest for developing modified nanostructured surfaces with high specific area, for example, by plasma treatments. Moreover, carbon is a commonly used material in FC in the form of microfibers of a gas diffusion layer (GDL).

The present doctoral thesis is focused on electron microscopy and spectroscopy investigation of novel metal-oxide anode catalysts for FC applications. The aim of this work is to study morphological changes and structural composition of Pt-doped CeO_x layers prepared by magnetron sputter deposition on carbonaceous substrates. Characterization of these thin films, control of their elaboration and optimization procedures and properties of such catalysts represent main goals. Understanding the growth mechanisms of catalytic layers is one of the most important targets of the investigation because it would permit more efficient development of new systems suitable for real fuel cell application.

In order to investigate the catalytic system at nanoscale, Transmission Electron Microscopy (TEM) has been chosen as a suitable technique. Morphology of layers prepared by magnetron sputtering is examined first by Scanning Electron Microscopy (SEM) by acquiring sample top-view images, and subsequently by TEM observations of cross-sectional lamellas prepared by using Focused Ion Beam (FIB). Crystallography studies are performed by High Resolution TEM (HRTEM). Chemical information is obtained via spectroscopy techniques implemented in a microscope, as Energy Dispersive X-ray Spectroscopy (EDX) and Electron Energy Loss Spectroscopy (EELS). Furthermore, X-ray Photoelectron Spectroscopy (XPS) is used as one of the most powerful analytic technique for detailed information of electronic structure and chemical composition of the catalyst. Combination of microscopy and spectroscopy techniques allows us to find the relation between morphology, structure and composition of the catalyst.

The content in this thesis is divided into three chapters. Chapter 1: State of Art starts from a brief overview of FC technology and presents the major challenges and limitations, which need to be overcome. The main principles of experimental techniques are given in Chapter 2. In addition, descriptions of used apparatus, as well as the most important parameters are presented there. Chapter 3 presents the

main results of the work and includes discussion of obtained findings. This chapter is divided in four parts, dealing with catalyst layer itself.

The first part of Chapter 3 deals with carbonaceous supports prepared by magnetron sputtering in argon or nitrogen atmosphere. It is shown by EELS and XPS techniques that the composition of carbonaceous films has an influence on the final catalyst morphology observed by TEM. Attention is focused on nitrogen content in the CN_x layers and investigation of oxygen plasma etching effect on carbonaceous films morphology is also carried out. During magnetron sputtering of CeO_x layers, an influence of deposition conditions as deposition time of cerium oxide, deposition rate and composition of working atmosphere on morphology of prepared catalytic layers is studied. Due to the variation in preparation parameters, we are able to distinguish different processes occurring during the magnetron sputtering of CeO_x layers and to propose a growth model. By finding equilibrium between the cerium oxide deposition and the oxygen plasma etching of carbon, which are taking place simultaneously, it is possible to tune catalyst morphology.

The second part is solely focused on catalyst layers, however for simplicity only CeO_x layers have first been grown and studied. The crystallography studies highlight the presence of cerium oxide crystallites. In addition, cerium carbides crystals are observed in the catalyst-carbon interface. Variation in crystal size depending on their localization, thickness and porosity of the catalyst layer is discussed. These parameters have also an influence on cerium stoichiometry. By EELS and XPS spectroscopy, it is found out that thinner layer is more reduced, the less continuous layer is the less stoichiometric one. Cerium reduction is related to the layer porosity, particle size and cerium-carbon interaction.

The third part of Chapter 3 is extended to Pt-doped CeO_x layers. An influence of platinum concentration on morphology, crystallography and electronic structure of the catalyst is studied. Morphological changes are observed with regard on the type of the catalyst support. Moreover, the more Pt added, the more metallic platinum clusters are observed by HRTEM. Such crystallites are of small size (2 nm) and located in deeper areas of porous structure. However, the XPS techniques, as a very surface sensitive method is not sufficient for their detection. On the other side, it is shown that doping CeO_x by small Pt concentrations (6%) leads to well dispersed ionic Pt species and Pt-Ce alloys formation.

Last part of Chapter 3 includes application of herein studied catalyst layers as a sufficient material for anode in FC. The commercial GDL surface is tuned by deposition of carbonaceous carrier followed by magnetron sputtering of Pt-CeO_x layers onto it. Such prepared catalyst reaches high surface area due to the porous structure and well dispersed platinum ions in cerium oxide matrix. From this perspective, presented manner of catalyst preparation, cerium oxide magnetron sputtering together with application of carbonaceous interlayers, represents promising technology for μ-FC devices.

Finally, the results and findings on microscopy and spectroscopy studies of novel Pt-doped cerium oxide based anode catalysts for fuel cell application are summarized in Conclusion part.

1 State of Art

1.1 Proton Exchange Membrane Fuel Cell

Fuel cells (FCs) are expected to become a promising technology for clean and efficient power sources in the near future. Recently, FCs have attracted wide attention due to their high power density, good chemical/thermal stability and environmentally friendly operation, which are classified into the "iron triangle" of performance, durability and cost [1]. Yet, the main obstacle to the commercialization of fuel cells is the high cost of platinum that is by far the most effective element used for FC catalysts and lifetime that is related to the degradation of the component material as catalyst support and catalyst itself [2]. Thus, it is essential to overcome these limitations.

By definition, the fuel cell is an electrochemical apparatus that converts chemical energy of fuel to electrical energy without fuel combustion [1]. There are many types of FCs classified usually by the electrolyte employed in the cell. An exception to this classification is the Direct Methanol Fuel Cell (DMFC), in which methanol is directly electrochemically oxidised. The other groupings are done by operating temperature, type of fuel, etc. The following list consists of the most widely used types of FC devices and their typical electrolyte and fuel, respectively:

- Alkaline Fuel Cells (AFC) – KOH, hydrogen,
- Proton Exchange Membrane Fuel Cell (PEMFC) – perflourocarbonsulfonic acid ionomers (Nafion®), hydrogen,
- Direct Methanol Fuel Cells (DMFC) – without electrolyte, methanol,
- Phosphoric Acid Fuel Cell (PAFC) – phosphoric acid, hydrogen,
- Molten Carbonate Fuel Cell (MCFC) – molten carbonates (LiK, LiNa), hydrogen,
- Solid Oxide Fuel Cell (SOFC) – ceria-, zirconia-, or yttria- supported electrolyte, hydrogen [3].

Our attention is focused on one of the most promising FC types, the Proton Exchange Membrane Fuel Cells (PEMFCs). This kind of FC was the first to be used

in space in Gemini program as a power source and also to provide the astronauts with clean drinking water [3]. It works at low temperature and as a fuel hydrogen is used. The reactions taking place in PEMFCs can be examined as follows: On the anode side, hydrogen is decomposed into protons diffusing through electrolyte to a cathode side, and electrons, which move through circuit towards the cathode and produce electrical current. On the other side of the apparatus, at the cathode, oxygen is electro-reduced to produce O^{2-} ions and consume electrons, whereas oxygen ions react with protons to form water molecules [4]:

Anode:	H_2	➔	$2H^+ + 2e^-$	(1.1)
Cathode:	$1/2O_2 + 2e^-$	➔	O^{2-}	(1.2)
Overall:	$1/2O_2 + H_2$	➔	H_2O	(1.3)

Electrolyte serves as a barrier to gas diffusion, to prevent the direct chemical combustion; however, ions can migrate across it. In a PEMFC a thin permeable polymeric membrane (e.g. Nafion® - perfluorisulfonic acid-PTFE copolymer), called Proton Exchange Membrane (PEM), is used as an electrolyte. The polymeric membrane together with the anode and cathode electrodes constitutes the Membrane Electrode Assembly (MEA), the most important part, in other words the central core of the fuel cell. A gas diffusion layer (GDL) is closely connected to the electrodes to supply gaseous reactants, oxygen and hydrogen. The schematic illustration of PEMFC arrangement is displayed in Fig. 1.1.

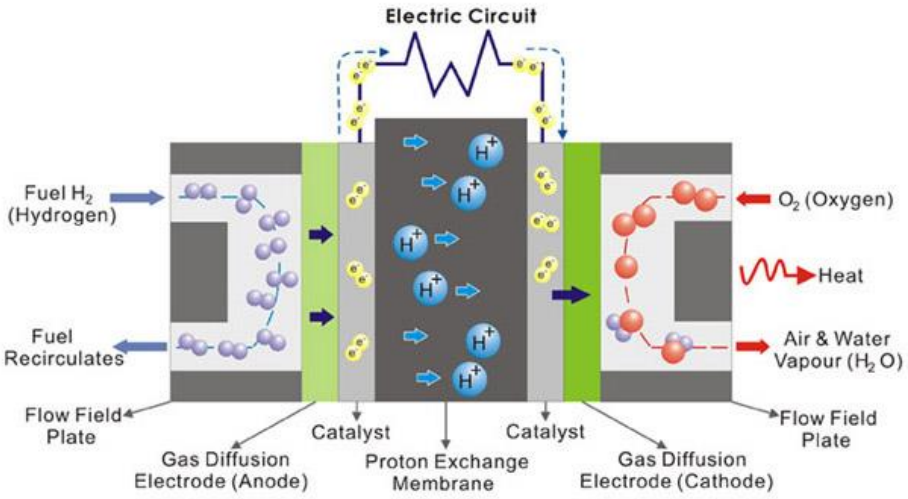

Fig. 1.1 Schematic illustration of PEMFC arrangement; taken from [5].

The main advantages of fuel cells lie in the high efficiency, the absence of moving parts, leading to no noise pollution, no emissions of environmental pollutants such as SO_x, NO_x, CO_2, CO, and as waste is only pure water. In contrary of benefits, only disadvantage of fuel cells is their higher costs; however, this problem can be solved by applying new technologies proposed in following chapters.

1.2 Catalysts for Anode Side of PEMFC

Platinum is one of the most versatile elements in catalysis and related application fields, as e.g. in fuel cell technology, due its high efficiency for large number of chemical reactions; however, its high costs limits the large-scale applications and wide spreading. In PEM fuel cells, Pt is typically used for both reactions, i.e. on anode and cathode sides. While our research is focused on improvement of the both electrodes [6, 7], herein, we will present only investigations on novel materials as anode catalyst, as the cathode part is not a subject of this thesis.

Nowadays, the Pt loading in commercially used FC anodes is in the range of 2-4 $mg.cm^{-2}$. Such catalyst exhibits excellent long-term stable performance, in spite of very high costs.

In order to decrease costs related to noble metal, two strategies can be applied to tackle this challenge: First, to use platinum as effective as possible. As only surface atoms take part in on-going catalytic reactions, this requirement can be met by well-dispersed platinum up to single atoms so that each of them will be exposed to reactants. Different dispersion methods have been adopted by many researchers [2, 8, 9]. In most cases, systems of Pt/C - metallic platinum particles in range of 2-6 nm dispersed by wet, electrochemical techniques among a carbon film as a catalyst support is used [8-11]. Regrettably, particles show a strong tendency to agglomerate and sinter [2, 9]. Second idea is to replace partially platinum by other less expensive materials. In an effort to decrease platinum amount, a PtRu catalyst was investigated [4, 12, 13]. It was shown that adding ruthenium can reduce Pt loading in an anode catalyst down to 0.05 $mg.cm^{-2}$ [13]. Moreover, Ru helps to overcome the problem of PEMFC anode catalyst poisoning by carbon monoxide (CO) [4, 13-15] present in fuel due to the manufactured processes. High concentration of CO can cause FC performance degradation. Instead of platinum replacement by metal, many oxides have been studied as materials to promote Pt catalytic activity, e.g. SnO_2 [16], WO_3 [17, 18], etc. These studies showed promising effect of oxides on platinum activity for PEMFC performance.

1.3 Support of Catalyst

An ideal support of catalysts for PEMFC should combine good electrical conductivity with high specific area and porosity for reactive gases [19]. Carbon-based materials are generally used in advance as a catalyst support due to their variety of properties.

Carbon-based materials are able to occur in ordered or amorphous structures due to three different hybridizations of carbon atoms, sp^3, sp^2 and sp^1 (Fig. 1.2). In the sp^3 configuration, as in diamond, each of valence electrons of carbon atom is assigned to a tetrahedrally directed sp^3 orbital, which makes a strong σ bond to an adjacent atom. On the other side, in sp^2 configuration, as in graphite, three of the four valence electrons enter trigonally directed sp^2 orbitals, which form bonds in a plane. The fourth electron of the sp^2 atom lies in a π orbital lying perpendicularly to the σ bonding plane. This π orbital forms a weaker π bond with another π orbital.

Such π bonding is also called unsaturated bonding. In the sp^1 configuration, as in acetylene, two electrons are assigned to linearly directed sp^1 hybrids, which form σ bonds and the other two are placed in π_y and π_z orbitals [20, 21]. Depending on bonding, various physical and chemical properties can be evinced.

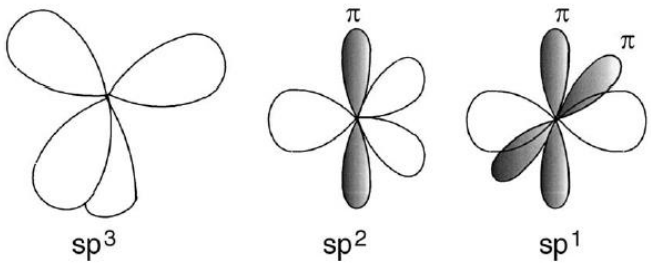

Fig. 1.2 Carbon hybridization; taken from [20].

Nowadays, a gas diffusion layer composed of a macroporous carbon fibre paper coated with microporous amorphous carbon black (*e.g.* Vulcan XC-72R) formed of small grains with size of 50-250 nm has been proven to be a suitable carbon carrier for catalytic layers [22-25]. Beside low costs of carbon black, the advantages consist mainly of the good electron conductivity and the large surface area [19, 22, 26]. However, it is not conclusively ideal material for a catalyst support due to the fast surface oxidation under PEMFC working conditions, especially, during the start-up and shut-down of the fuel cell [27-29]. It was shown [9, 30] that water electrolysis and carbon oxidation resulted in CO and CO_2 formation, which have a high influence on the degradation of carbon black. The electrochemically caused corrosion of carbon decreases the electrical conductivity and, therefore, the contact area with noble metal is decreased as well. The attachment of catalytic particles is weakened, which results in their sintering and agglomeration [2, 27]. Subsequently, it has negative influence on the FC performance.

Beside carbon black, nitrogen-doped carbon materials, mostly in form of carbon nanotubes [31-34], were reported as a possible catalyst support alternative. Carbon nitride (CN_x) films exhibit higher hardness, elasticity [35, 36] and better electric conductivity [36-38] compared to amorphous carbon (a-C). It was shown [39, 40] that with the rising amount of nitrogen in carbon layers, proportion of π bonds between carbon and nitrogen atoms is increased. Accordingly, as a result of higher conductivity, better metal-support interaction between CN_x and a catalyst is

achieved and thus, catalyst activity, its stability and durability in PEMFC reactions are increased [31, 32, 41].

1.4 Platinum Doped Cerium Oxide Catalyst Layers

Cerium oxide, one of the very promising materials, which has recently been gaining a lot of researchers' attention [42-44], is valued for its high oxygen storage capacity, i.e. ability to easily release, store or transport oxygen accompanied by transition between two stable states Ce^{4+} and Ce^{3+} [45, 46], and for its ability to enhance the activity of transient metal and metal oxide catalysts [47-49]. Stoichiometric cerium oxide, usually called ceria, CeO_2, has the cubic fluorite structure as displayed in Fig. 1.3 a). Its space group is Fm-3m (n°225) and the parameter cell is equal to 0.541 nm. When treated in a reducing atmosphere, CeO_2 is known to form a continuum of oxygen-deficient, nonstoichiometric CeO_{2-x} oxides (with $0 \leq x \leq 0.5$). Cerium itself (Ce) is a metal that belongs to the lanthanide group and has the valence orbital electron configuration $4f^1\ 5d^1\ 6s^2$. The valence orbital electron configuration differs for stoichiometric cerium oxide, CeO_2, as Ce in 4^+ state has empty *4f* orbital, and in case of reduced cerium oxide, Ce_2O_3 with cerium in 3^+ state has one electron in the *4f* orbital. The structure of Ce_2O_3 is trigonal (Fig. 1.3 b), with space group P-3m1 (n°150) and the parameter cell of a = 0.389 nm and c = 0.607 nm [47].

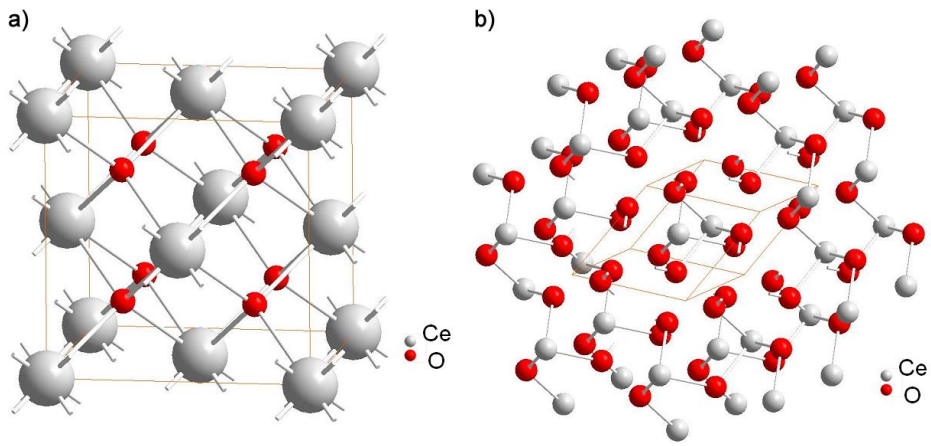

Fig. 1.3 Schematic illustration of CeO_2 fluorite structure a) and Ce_2O_3 trigonal structure b) [50].

Cerium oxide doped by platinum is used as a catalyst in oxidation processes like oxidation of CO contaminants from automotive exhaust gases [51, 52], water-gas shift reactions [53], oxidation of ethanol [54], and decomposition of methanol [55]. Such a high oxidation activity of Pt–CeO_x can be explained by metal–oxide interaction, thus electron transfer from the Pt nanoparticles to the support and oxygen transfer from CeO_x to Pt [56].

In our research we are focused on the Pt-CeO_x thin films system prepared by a simple elaboration technique based on magnetron sputter deposition on carbon supports [57-59]. As it was mentioned above, most studies on catalysts deal with alloys prepared via wet chemical methods. Thin films techniques are not common in catalysis development yet, since they are generally considered incompatible with the preparation of catalysts with large surface area. On the contrary, we have shown that we are able to prepare extremely porous structures on carbonaceous substrates by suitable choice of deposition conditions, catalyst materials and substrates [60-62]. Moreover, magnetron sputter deposition technique allows us to combine any elements by simply co-sputtering and tune their concentrations. As a result of our effort, we reached catalytic material of very porous structure with Pt loading around 2 $\mu g.cm^{-2}$, which is about 1000-times less than in case of commercial anodes. Such catalyst was found to be very active in a PEMFC giving the specific power of such prepared anode catalyst comparable to commercial one [63].

Bibliography of Chapter 1.

[1] S.J. Peighembardoust, S. Rowshanzamir, M. Amjadi, *Int. J. Hydrogen Energy* 35 (2010) 9349.

[2] Y. Shao, G. Yin, Y. Gao, *J. Power Sources* 171 (2007) 558.

[3] L. Carrette, K.A.Friedrich, U. Stimming, *ChemPhysChem* 1 (2000) 162.

[4] S.M. Haile, *Acta Mater.* 51 (2003) 5981.

[5] G-Energy Technologies Sdn. Bhd. www.g-energy.com.my

[6] M. Vorokhta, I. Khalakhan, M. Vaclavu, G. Kovacs, S.M. Kozlov, P. Kus, T. Skala, N. Tsud, J. Lavkova, V. Potin, I. Matolinova, K.M. Neyman, V. Matolin, *Appl. Surf. Sci.* 365 (2016) 245.

[7] R. Fiala, M. Vaclavu, M. Vorokhta, I. Khalakhan, J. Lavkova, V. Potin, I. Matolinova, V. Matolin, *J. Power Sources* 273 (2015) 105.

[8] M.S. Saha, R. Li, X. Sun, *J. Power Sources* 177 (2008) 314.

[9] X. Yu, S. Ye, *J. Power Sources* 172 (2007) 145.

[10] K. Lee, J. Zhang, H. Wang, D.P. Wilkinson, *J. Appl. Electrochem.* 36 (2006) 507.

[11] S. Litster, G. McLean, *J. Power Sources* 130 (2004) 61.

[12] E. Antolini, *Mater. Chem. Phys.* 78 (2003) 563.

[13] H.A. Gasteiger, J.E. Panels, S.G. Yan, *J. Power Sources* 127 (2004) 162.

[14] P. Costamagna, S. Srinivasan, *J. Power Sources* 102 (2001) 242.

[15] N.P. Brandon, S. Skinner, B.C.H. Steele, *Annu. Rev. Mater. Res.* 33 (2003) 183.

[16] A. Katayama, *J. Phys. Chem.* 84 (1980) 376.

[17] P. Shen, A. Tseung, *J. Electrochem. Soc.* 141 (1994) 3082.

[18] J. Rajeswari, B. Viswanathan, T. Varadarajan, *Mater. Chem. Phys.* 106 (2007) 168.

[19] A.L. Dicks, *J. Power Sources* 156 (2006) 128.

[20] J. Roberston, *Mater. Sci. Eng., R* 37 (2002) 129.

[21] J. Robertson, Prog. *Solid St. Chem.* 21 (1991) 199.

[22] L. Cindrella, A.M. Kannan, J.F. Lin, K. Saminathan, Y. Ho, C.W. Lin, J. Wertz, *J. Power Sources* 194 (2009) 146.

[23] J.H. Chun, K.T. Park, D.H. Jo, S.G. Kim, S.H. Kim, *Int. J. Hydrogen Energy* 36 (2011) 1837.

[24] C. Santoro, A. Agrios, U. Pasaogullari, B. Li, *Int. J. Hydrogen Energy* 36 (2011) 13096.

[25] V. Metha, J.S. Cooper, *J. Power Sources* 114 (2003) 32.

[26] R. Borup *et al*., *Chem. Rev.* 107 (2007) 3904.

[27] H. Tang, Z. Qi, M. Ramani, J.F. Elter, *J. Power Sources* 158 (2006) 1306.

[28] Y. Shao, J. Wang, R. Kou, M. Engelhard, J. Liu, Y. Wang, Y. Lin, *Electrochim. Acta* 54 (2009) 3109.

[29] S.D. Knights, K.M. Colbow, J. St-Pierre, D.P. Wilkinson, *J. Power Sources* 127 (2004) 127.

[30] Z. Siroma, M. Tanaka, K. Yasuda, K. Tanimoto, M. Inaba, A. Tasaka, *Electrochemistry* 75 (2007) 258.

[31] Y. Shao, J. Sui, G. Yin, Y. Gao, *Applied Catalysis B: Environmental* 79 (2008) 89.

[32] T. Maiyalagan, B. Viswanathan, U.V. Varadaraju, *Electrochemistry Comm.* 7 (2005) 905.

[33] C-L. Sun, L-C. Chen, M-C. Su, L-S. Hong, O. Chzan, C-Y. Hsu, K-H. Chen, T-F. Chang, L. Chang, *Chem. Mater.* 17 (2005) 3749.

[34] S. van Dommele, K.P. de Jong, J.H. Bitter, *Chem. Commun.* (2006) 4859.

[35] E. Broitman, N. Hellgren, K. Jarrendahl, M.P. Johansson, S. Olafsson, G. Radnoczi, J-E. Sundgren, L. Hultman, *J. Appl. Phys.* 89 (2001) 1184.

[36] A.Z. Sadek, M. Kracica, A. Moafi, D.W.M. Lau, J.G. Partridge, D.G. McCulloch, *Diamond Relat. Mater.* 45 (2014) 58.

[37] R. Czerw, M. Terrones, J-C. Charlier, X. Blasé, B. Foley, R. Kamalakaran, N. Grobert, H. Terrones, D. Tekleab, P.M. Ajayan, W. Blau, M. Ruhle, D.L. Carroll, *Nano Lett.* 1 (2001) 457.

[38] V.V. Strelko, V.S.Kuts, P.A.Thrower, *Carbon* 38 (2000) 1499.

[39] N. Mubumbila, B. Bouchet-Fabre, C. Godon, C. Marhic, B. Angleraud, P-Y. Tessier, T. Minea, *Diamond Relat. Mater.* 13 (2004) 1433.

[40] N. Axen, G.A. Botton, R.E. Somekh, I.M. Hutchings, *Diamond Relat. Mater.* 5 (1996) 163.

[41] G. Bae, D. H. Youn, S. Han, J.S. Lee, *Carbon* 51 (2013) 274.

[42] C-Y. Cao, Z-M. Cui, C-Q. Chen, W-G. Song, W. Cai, *J. Phys. Chem.* 114 (2010) 9865.

[43] J.A. Farmer, C.T. Campbell, *Science* 329 (2010) 933.

[44] H. Chen, J. Duan X. Zhang, Y. Zhang, C. Guo, L. Nie, X. Liu, *Mater. Lett.* 126 (2014) 9.

[45] N.V. Skorodumova, S.I. Simak, B.I. Lundqvist, I.A. Abrikosov, B. Johansson, *Phys. Rev. Lett.* 89 (2002) 166601.

[46] J. Kaspar, P. Fornasiero, M. Graziani, *Catal. Today* 50 (1999) 285.

[47] A. Trovarelli, Catalysis by Cerium Oxide and Related Materials, *Imperial College Press*, London, UK, (2002), ISBN 1-86094-299-7.

[48] I.D. Gonzalez, R.M. Navarro, W. Wen, N. Marinkovic, J.A. Rodriguez, F. Rosa, J.L.G. Fierro, *Catal. Today* 149 (2010) 372.

[49] W. Xu, R. Si, S.D. Senanayake, J. Llorca, H. Idriss, D. Stacchiola, J.C. Hanson, J.A. Rodriguez, *J. Catal.* 291 (2012) 117.

[50] Software Diamond-Crystal and Molecular Structure Visualization, Version 3.2h, 1997-2012, Crystal Impact GbR, Bonn, Germany.

[51] W. Liu, M. Flytzani-Stephanopoulos, *J. Catal.* 153 (1995) 317.

[52] I. Manuel, C. Thomas, H. Colas, N. Matthess, G. Diega-Mariadassou, *Top. Catal.* 311 (2004) 30.

[53] D. Pierre, W. Deng, M. Flytzani-Stephanopoulos, *Top. Catal.* 46 (2007) 363.

[54] X. Tang, B. Zhang, Y. Li, Y. Xu, Q. Xin, W. Shen, *J. Mol. Catal. A: Chem.* 235 (2005) 122.

[55] S. Imamura, T. Higashihara, Y. Saito, H. Aritani, H. Kanai, Y. Matsumura, N. Tsuda, *Catal. Today* 50 (1999) 369.

[56] G.N. Vayssilov, Y. Lykhach, A. Migani, T. Staudt, G.P. Petrova, N. Tsud, T. Skala, A. Bruix, F. Illas, K.C. Prince, V. Matoliin, K.M. Neyman, J. Libuda, *Nat. Mater*. 10 (2011) 310.

[57] V. Matolin, I. Matolinova, M. Vaclavu, I. Khalakhan, M. Vorokhta, R. Fiala, I. Pis, Z. Sofer, J. Poltierova/Vejpravva, T. Mori, V. Potin, H. Yoshikawa, S. Ueda, K. Kobayashi, *Langmuir* 26 (15) (2010) 12824.

[58] M. Vorokhta, I. Khalakhan, I. Matolinova, M. Kobata, H. Yoshikawa, K. Kobayashi, V. Matolin, *Appl. Surf. Sci.* 267 (2013) 119.

[59] I. Khalkhan, M. Dubau, S. Haviar, J. Lavkova, I. Matolinova, V. Potin, M. Vorokhta, V. Matolin, *Ceram. Int.* 39 (2013) 3765.

[60] S. Haviar, M. Dubau, J. Lavkova, I. Khalakhan, V. Potin, V. Matolin, I. Matolinova, *Sci. Adv. Mater.* 6 (2013) 1278.

[61] M. Dubau, J. Lavkova, I. Khalakhan, S. Haviar, V. Potin, I. Matolinova, V. Matolin, *ACS Appl. Mater. Interfaces* 6 (2014) 1213.

[62] J. Lavkova, I. Khalakhan, M. Chundak, M. Vorokhta, V. Potin, V. Matolin, I. Matolinova, *Nanoscale* 7 (2015) 4048.

[63] R. Fiala, I. Khalakhan, I. Matolinova, M. Vaclavu, M. Vorokhta, Y. Sofer, S. Huber, V. Potin, V. Matolin, *J. Nanosci. Nanotechnol.* 11 (2011) 5062.

2 Experimental Techniques and Equipment

In the following chapter, a brief introduction to used methods and the main principle for each technique will be given. In addition, the description of our equipment will be presented in detail including specific conditions and parameters used for sample preparation and characterization.

2.1 Thin Films Deposition

There are dozens of deposition technologies for material formation. Concerning thin film preparation, two main groups can be distinguished according to the physical or chemical nature of the main principle involved during the sample preparation. However, some methods are either purely physical or purely chemical, though a considerable number of processes that are based on glow discharge and reactive sputtering combine both physical and chemical reactions. The detailed classification can be found elsewhere [1, 2]. Herein, we will focus our attention to the *magnetron sputtering* technique.

Sputtering, in general, is a basic and well-known process of thin film preparation widely used in industrial and laboratory applications. It is based on the ejection of atoms from an electrode surface by momentum transfer from bombarding ions to the surface atoms [1]. The primary ions are generated in glow discharge plasma within a working gas (usually inert gas) and accelerated by negative voltage applied to the target, i.e. to the cathode. The primary ions collision with the target surface leads to the sputtering of the target material and the ejected species (atoms, molecular fragments, ions) condense on a substrate as a thin film.

Nevertheless, the conventional sputtering process gives a very low efficiency of working gas ionization and thus, a low deposition rate. Moreover, high cathode voltage and working gas pressure are needed to sustain plasma in the chamber. Therefore, the modification by using magnetic field from permanent magnets situated near the target helps to overcome these problems. The arrangements of electric and magnetic fields with configuration displayed in Fig. 2.1 force electrons

to circulate along the magnet field lines [3]. These circulations increase the traveling way of electrons that leads to a substantial increase of working gas ionization and thus, to increase of sputtering yield.

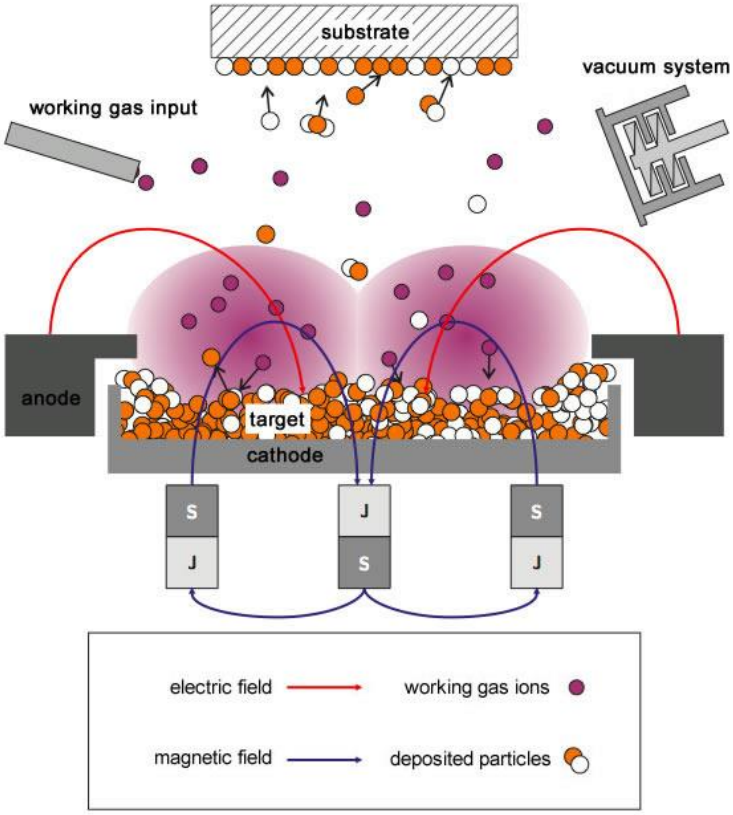

Fig. 2.1 Schematic illustration of arrangement during the magnetron sputtering process; taken from [4].

Depending on the sputtered material, there are two types of magnetron sputtering modes differing by used voltage applied on the target playing a role of cathode – direct current (DC) power and radiofrequency (RF) one. Generally, the DC power sources are used for conductive materials, while RF power supply is used in case of dielectrics. In addition, combination of more magnetrons in one chamber makes possible co-sputtering of different materials leading to the formation of thin films with variable concentration of elements. As an example, we can mention the deposition of oxide layers doped by metal (Pt-CeO_x, Pd-CeO_x, Pt-SnO_x) via RF power source applied on a dielectric target and DC voltage on a metal one [5, 6].

Instead of inert gas used as a working gas (usually argon), i.e. non-reactive magnetron sputtering, we can use gas, which reacts in the discharge with deposited

material (e.g. oxygen, nitrogen) [1]. Thus, using reactive magnetron sputtering, the composition of a deposited film can be changed by modification of working atmosphere, e.g. by sputtering of metal in the oxygen plasma, metal oxide can be deposited on a substrate [7].

2.1.1 Carbon Films Preparation

Amorphous carbon (a-C) and carbon nitride (CNx) films were prepared by DC magnetron sputtering from a 2-inch diameter graphite target (Goodfellow, purity 99.997%) using a commercial Modular High Vacuum Coating system MED020 (BALTEC). Pieces of a (100)-oriented p-doped silicon wafer of 500 μm thickness have been used as substrates. The target-to-substrate distance was 50 mm. Sputter depositions were carried out at constant current of 20 mA using nitrogen/argon gas mixtures as process gases. Argon and nitrogen gas flows were controlled with mass flow controllers. In order to achieve various nitrogen doping of the carbon films, the nitrogen/argon gas flow ratio was varied keeping the total gas flow constant at 23 sccm, which results in a total gas pressure of approximately 0.8 Pa.

The notation of the prepared carbon layers is in accordance with the amount of nitrogen in working gas during the magnetron sputtering process, i.e. pure argon atmosphere corresponds to a-C layer, 5% of nitrogen corresponds to CN_x5%, 25% of nitrogen corresponds to CN_x25%, etc. However, in order to obtain the CN_x100% film, pressure of pure nitrogen 4 Pa can be also used. Therefore, unless otherwise noted, the notification of CN_x100%, will correspond to the layer prepared with the gas pressure of 4 Pa [8, 9].

The MED020 system was used, as well, for an oxygen plasma treatment via an etching device consisting of a ring-shaped driven Al electrode placed 2 cm above a grounded substrate holder. Accordingly, the DC discharge was ignited between the electrode and the substrate holder. The process gas was pure oxygen at a total pressure of 20 Pa. The discharge current was set equal to 1.7 mA and the discharge voltage automatically adjusted by the MED020 system was close to 430 V [8].

2.1.2 Catalyst Layers Preparation

Deposition of cerium oxide (CeO_x) thin films has been carried out using the RF magnetron sputtering in a homemade magnetron sputtering system. A 2-inch CeO_2 target (Lesker, purity 99.99%) was placed at a distance of 90 mm from substrates. Deposition was carried out at room temperature in the system with a residual pressure less than 4.10^{-4} Pa.

The process gas was pure argon or an oxygen/argon mixture at a total pressure of 4.10^{-1} Pa. The oxygen partial pressure was adjusted with a needle valve and measured with a vacuum gauge. The concentration of oxygen in the working gas was varied in order to obtain modification in porosity of deposited cerium oxide layers. Accordingly, the applied discharged power was also changed. Both parameters have an influence on the total deposition rate of CeO_x layers, which is determined from cerium oxide deposition time and a thickness of the deposited layer sputtered on a silicon substrate. We use silicon as a reference substrate because during the same deposition process the cerium oxide layers are growing compact on silicon [10]. In the following chapter, the parameters for the preparation of each CeO_x layer will be specified by the partial pressure of oxygen and the deposition rate. If the partial pressure is not mentioned, thus, no additional oxygen was added to the working gas and the oxygen pressure is considered as a pressure of residual atmosphere of 4.10^{-4} Pa.

In order to obtain platinum doped CeO_x layers, platinum wires (diameter d = 0.404 mm) have been placed on top of the CeO_2 target. The variation in Pt dopant concentration was modified by varying the number of used Pt wires from one to three. The final concentration was set by quantification of Pt 4f spectra obtained by XPS measurement. Other deposition conditions remain the same as in case of non-doped CeO_x layers.

2.2 Electron Microscopy

Nowadays, the electron microscopy is an indispensable method for research in the field of materials science. Microscopy techniques offer direct observation of

morphology, structure and composition of prepared samples, which allows us to better understand their properties at atomic scale.

2.2.1 Scanning Electron Microscopy

The main principle of Scanning Electron Microscopy (SEM) is based on an interaction with a high-energy electron beam by scanning it on the studied sample surface. When accelerated electrons enter a solid, they are scattered elastically, by an electrostatic interaction with atomic nuclei and inelastically, by an interaction with atomic electrons. Whereas most of the interactions leads to inelastically forward scattered electrons with deflection angle less than 90°, only a small fraction of primary electrons are elastically backscattered (BSE). The volume of the sample containing scattered electrons is called the interaction volume and its size depends on penetrated material and energy of primary electrons. Therefore, the detected backscattered electrons display chemical contrast of the sample composition. This information comes from depth about tens to hundreds nanometers (Fig. 2.2), as the electrons have almost no energy losses. However, due to small number of BSE, detected signal has low intensity with high proportion of noise.

The inelastic collision is typical by energy transfer; the energy loss of entering electrons will appear as a gain in energy of outer-shell electrons. A small part of acquired energy will be used up to release electrons from particular atoms and the rest to kinetic energy of escaping electrons from solid as secondary electrons (SE). As the SE traveling through the solid interact with other atomic electrons, gradually losing their kinetic energy, the escaping electrons are generated only within very small escape depth (< 2 nm, Fig. 2.2). Therefore, the image created by SE displays surface structure, i.e. topographical contrast.

When a primary electron enters a specimen and interacts inelastically with an inner-shell electron, causing the transition to a higher-energy orbit, it will leave the atom with an electron vacancy in its inner shell. The scattering atom remains in this excited state only a brief period of time, as one of the other atomic electrons fills the vacancy by making the downward transition. During this de-excitation process, the energy can be released in form of X-ray photon or transferred to another electron escaping from the surface as an Auger electron. Both, the X-ray photons and Auger electrons can be detected in order to obtain information about chemical composition

of the sample, in general, noticed as Analytical Electron Microscopy (AEM). Nevertheless, the information depth and the yield differ significantly. While for Auger electrons, the information originates from few Angstroms under the sample surface, the X-ray photons are able to escape from hundreds of nm depth (Fig. 2.2). In addition, the yield is increased with increasing atomic number in case of X-ray, whereas the Auger yield has opposite tendency. The detection of Auger electrons is a rare method in electron microscopy. On the other hand, the X-ray signal detection is a base of Energy Dispersive X-ray Spectroscopy (EDX), which main principles will be mentioned in Section 2.3.1 Energy Dispersive X-ray Spectroscopy [11].

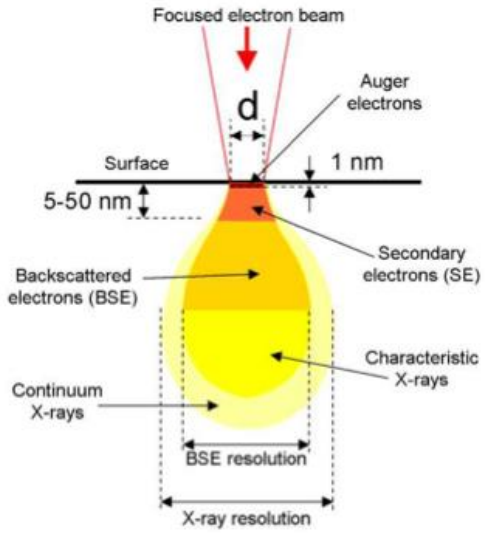

Fig. 2.2 Schematic illustration of the excitation volume for an interaction of a primary electron beam with solid and information depth for each type of signal; taken from [12].

The typical construction of the SEM is displayed in Fig. 2.3. The main component of an electron gun is a cathode, which is of source of electrons. Depending on the character of electron emission, the request for working conditions and performance differs. The electrons can be produced by thermal emission or field emission, whilst their combination is known as the Schottky cathode. The microscopes with this kind of the cathode are usually marked as FEG (field emission gun), however, we have to note that it is not of the cold-field emission type. The cathode can be in form of a filament made from tungsten or LaB_6 (thermionic emission), tungsten tip (field emission) or moreover, coated by ZrO (Schottky emission). Another important component of the electron gun is the Wehnelt cylinder,

a metal electrode, which surrounds the cathode completely except for the small hole in the middle through which the electron beam emerges. Its function is to control the emission current of the electron beam and to serve as a convergent electrostatic lens. In order to control electron beam voltage, the extractor with positive potential is placed afterwards. The potential applied between the cathode and the extractor – the anode will accelerate the electrons. The energy of the incidence electron beam can be varied from 100 eV to 30 keV. The electron beam is focused into a narrow beam by series of electromagnetic lenses placed in the SEM column. The final diameter of the electron beam can be as small as 1 nm. Such a probe is scanning on the sample surface in a raster pattern by deflective lenses. The interaction of the electron beam with the solid will lead to signals emission, which can be collected by a detector mostly in form of CCD camera (Charge-Coupled Device).

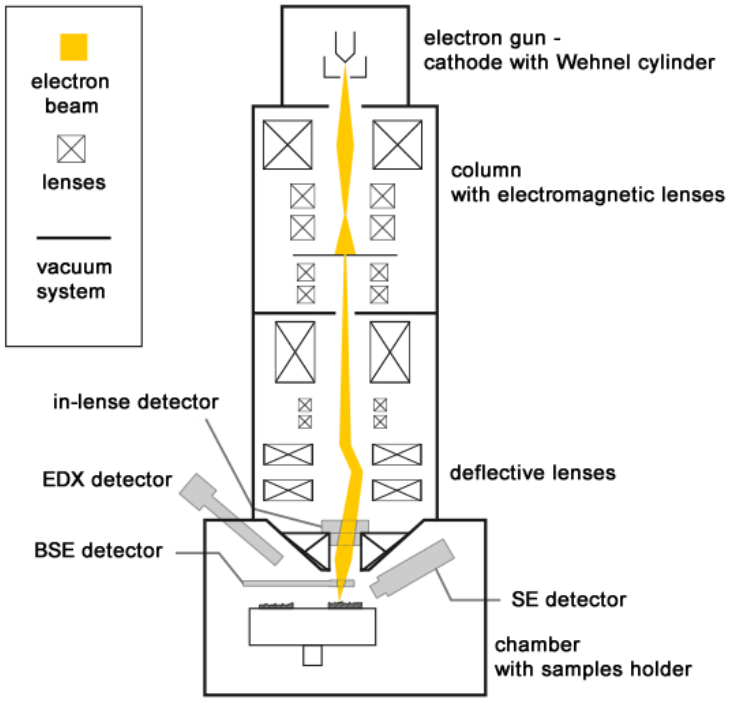

Fig. 2.3 Cross-sectional diagram of SEM equipment; taken from [4].

The morphology of prepared samples was examined by SEM using a MIRA III and/or LYRA Tescan microscope with an energy of the electron beam of 30 keV at working pressure of 1.10^{-2} Pa. Most images were acquired in SE mode.

2.2.2 Focused Ion Beam and Gas Injection System

Nowadays, the Focused Ion Beam (FIB) technique has become very useful for device modification and sample preparation. Through new techniques and applications this instrument has taken its place in analytical laboratories, universities, geological, medical and biological research institutions. Although the utility of the FIB is not limited to the preparation of specimens for subsequent analysis by other analytical techniques, it has revolutionized the area of Transmission Electron Microscopy (TEM) specimen preparation. The main advantage over traditional methods is the relative simplicity, high success and ability to produce specific samples in a short time.

The liquid-metal ion source (LMIS) constructed by Krohn *et al.* in 1961 [13], used mostly as a source of ions is displayed in Fig. 2.4. The heavy-metal atoms (typically gallium) in a reservoir are heated up to near evaporation and flow down through a sharp tungsten needle. Due to the positive potential applied on the tungsten tip, the point source of particles, called the Taylor cone with a diameter in range 2-5 nm, is formed. In front of the tungsten tip, an extractor, in shape of an annular electrode with negative potential, is placed. The strong electric field between the tungsten tip and the extractor leads to the ejection of metal particles from the Taylor cylinder. They are ionized and accelerated through the column. The energy of ions can be varied from 5 keV to 30 keV. The extraction current, current emitted from the tip, is regulated by the extractor and in addition, by the suppressor, an electrode with positive potential placed between the extractor and the tungsten tip. Adjusting suppressor voltage may change the extraction current without changes on the extractor, thus, it will avoid the spatial displacement of the Taylor cone and apparent beam drift caused by changing the extractor voltage. For subsequent beam adjustment, a spot size diameter and a value of probe current, the sequence of apertures and electromagnetic lenses is used. The probe current can be varied in range of few pA to tens of nA depending on the application [14].

Usage of gallium as a heavy-metal in the LMIS reservoir has many advantages. First, because of its low melting point, gallium requires limited heating and can conveniently be in liquid phase during operation. The lower heating temperature minimizes interdiffusion with the tungsten needle and yields a long

source life. Second, its mass is heavy enough to allow rough milling of heavier elements; however, it is not so heavy to destroy the sample immediately. Finally, gallium can be easily distinguished from other elements, as it will not interfere with the analysis of the sample.

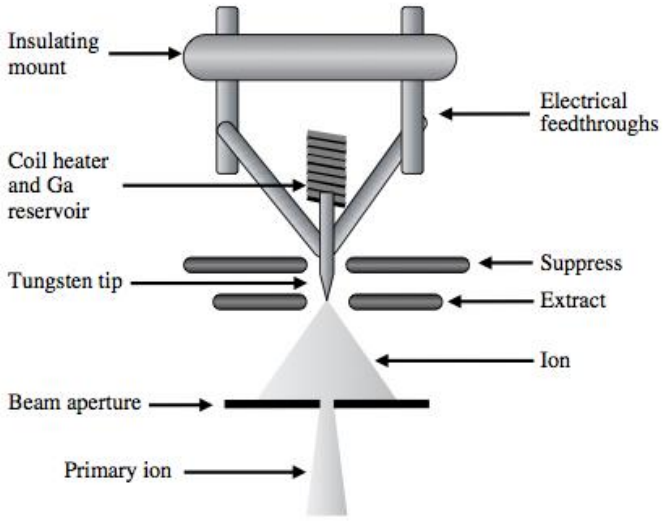

Fig. 2.4 Cross-sectional diagram of LMIS used in FIB; taken from [14].

By an interaction of the Focused Ion Beam with the solid, the secondary electrons (SE), backscattered electrons (BSE) and secondary ions (SI) are emitted. Generally, SE are 10-1000 times higher than the amount of SI, therefore, SE are used for imaging of the sample surface. The detectors are analogous to the ones used in SEM; however, the resolution is not better than 10 nm. Images offer topographical contrast and partially chemical contrast, as well. Nevertheless, chemical contrast is better displayed by SI. Since the detector for SI is the same as in case of SE, the negative potential is applied on the grid of detector, in order to deflect electrons and collect positive ions [14].

Apart from the particles sputtering, an interaction of the high energetic ions with the solid may lead to the incorporation of entering ions in the matrix of penetrated material. The penetration depth (R_p) depends on the energy of ions, their atomic number, as well as on the atomic number of penetrated solid and the incidence angle [13]. The complicated relation is simulated by Monte Carlo and/or molecular dynamics methods. As an example of freeware software can be mentioned SRIM (Stopping and Range of Ions in Matter) software developed by Ziegler *et al*.

[15]. While in most cases the ion implantation is considered as an undesirable effect [16], which leads to the layer amorphisation, it can be also used as aimed doping of material [17].

The main application of FIB is the sample modification including milling, thinning and deposition processes. Rough removing of material and slight elimination of the thickness is occurred by simply interaction of the incident ions with sample due to the voltage and current control. However, for material deposition, additional equipment is needed. It is a Gas Injection System (GIS), which is implemented in the system in order to create the cloud of atoms above the sample. In a reservoir of GIS, the precursor of material is heated and delivered by nozzles in the chamber. Precursor is composed by main component atoms (tungsten, platinum, etc.) attached with organic molecules ($W(CO)_6$, $(CH_3)_3(CH_3C_5H_4)Pt$) because of sufficient sticking probability on the sample surface and rapid decomposition properties. Ion beam scanning in the area, where the cloud of precursor is injected, leads to the ion beam-induced deposition (IBID). The process includes decomposition of precursor to the volatile organic molecules, which are pumped away by a vacuum system and adsorption of purified main component on the sample surface. The whole process is sketched by schematic diagram in Fig. 2.5. Besides the ion beam, the electron beam can be used for the beam-induced deposition (EBID), as well. Nevertheless, the deposition rate is much lower and the decomposition of the precursor is not sufficient. The organic elements are not removed completely, thus, they are contained in the deposited layer. On the other side, due to the low mass of electrons, the deposition is gentler to the sample surface, the layers at a very surface are not damaged or destroyed by high energetic beam.

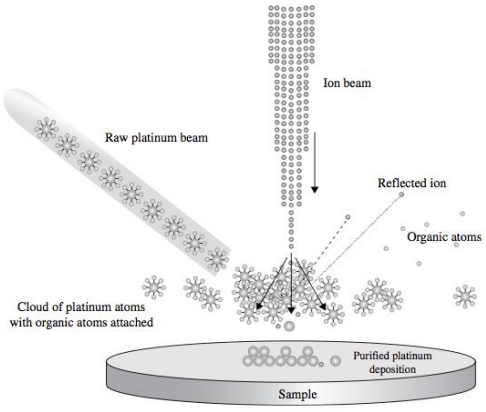

Fig. 2.5 Schematic diagram of IBID; taken from [14].

In the last tens years, the FIB has brought the revolution to the sample preparation for TEM. The "lift-out" *in situ* technique has spread to laboratories due to the many advantages. First, the area of interest can be selected precisely, as FIB is usually inserted in SEM device. Therefore, it is able to prepare a TEM sample, in form of thin lamella, directly from the bulk sample observed before in SEM. Second, the method is non-destructive, as the lamella is prepared from the area of few squared microns. The rest of the sample remains untouched. Compared with the traditional techniques, mechanical stress occurring due to the mechanical polishing is limited. Moreover, the sample is thinned homogenously down to less than 50 nm in a large area. Finally, the method is not time consuming. The preparation of thin lamella by "lift-out" *in situ* technique takes around one hour instead of one or two days necessary for sample preparation by traditional techniques. In addition, due to a special sample holder, we are able to insert 8 samples into the TEM chamber at the same time. The main steps of "lift-out" *in situ* technique for TEM samples preparation can be found elsewhere [18-20]. Herein, we present our device and parameters used during the process of lamella preparation.

A dual beam microscope LYRA Tescan was used for cross-sectional samples preparation. The microscope is equipped with electron and ion beams, a GIS device and a single manipulator able to move in three directions. A cross-sectional diagram of chamber arrangement and photography of the real system are shown in Fig. 2.6.

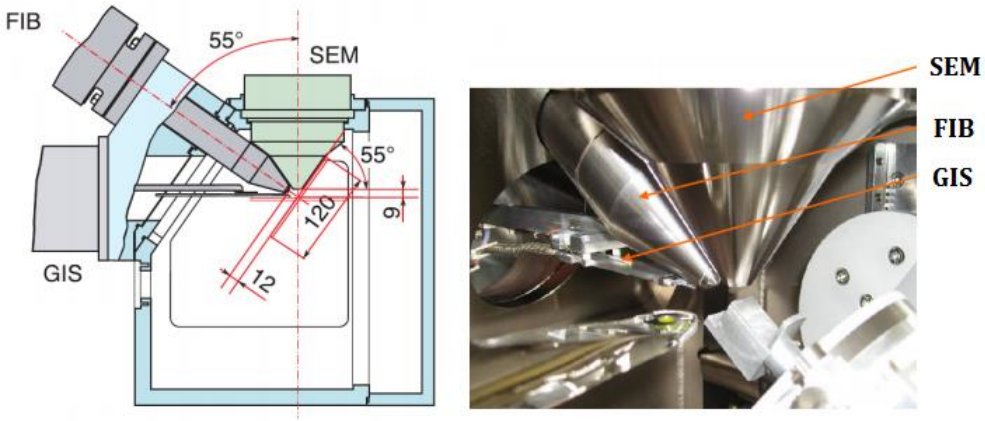

Fig. 2.6 Cross-sectional diagram of chamber arrangement and photography of the real system; taken from [21].

For imaging of sample surface, the SE signal generated by primary electrons at an energy of 30 keV was used. First of all, on the sample surface an area of 1 x 10 μm^2 was selected to be covered by a protective layer in order to minimize sample destruction by a high-energy beam. We used silicon or platinum as a material suitable for protective layer deposition. Protective material was chosen such a way to be able obtain the best possible image contrast during TEM observation of studied sample. The protective layer was deposited first, by EBID at an energy of 5 keV and a beam current of 600 pA, and subsequently, by IBID at an energy of 30 keV and a beam current of 250 pA (Fig. 2.7 a). Rough milling was performed by the ion beam at a beam current of 10 nA (Fig. 2.7 b) followed by slight thinning and cutting through the structure at a beam current of 800 pA (Fig. 2.7 c). Then the lamella was fixed on a tungsten tip (radius<0.5mm, taper angle 10-13°, Omniprobe) (Fig. 2.7 d) and a sample holder (4-post Cu lift out grid, Omniprobe) by IBID using platinum (Fig. 2.7 e). Final thinning was performed in two steps, at a beam current of 250 pA, with tilting the sample ±2° and subsequently, with lower beam energy of 5 keV at a beam current of 200 pA, with tilting the sample ±7°. The final thickness of the lamella prepared such a way is typically below 50 nm (Fig. 2.7 f and g).

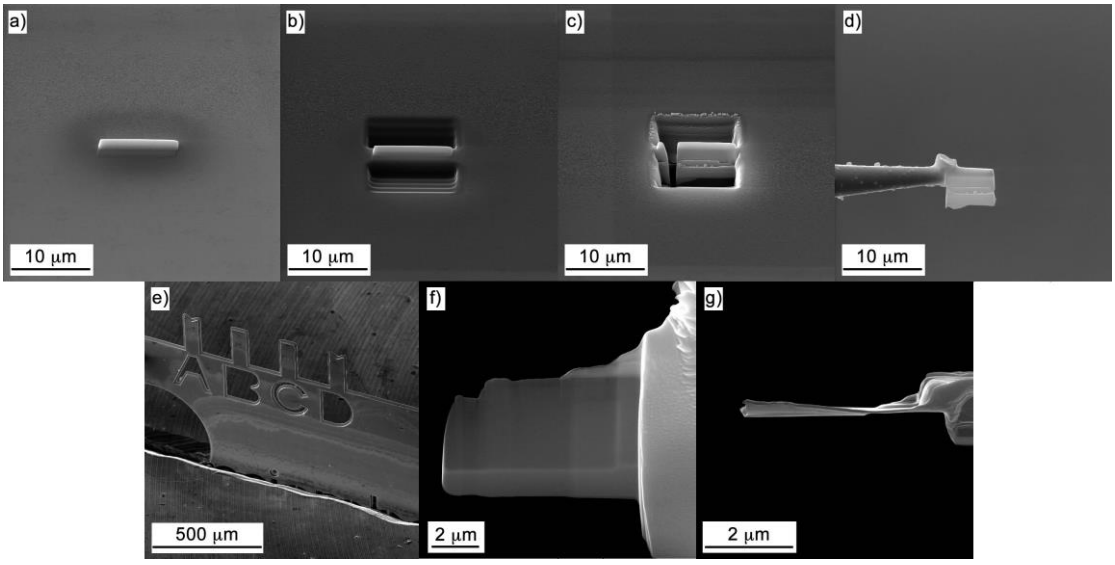

Fig. 2.7 Individual steps of "lift-out" *in situ* technique resulted in a lamella suitable for TEM observation. Protective layer deposition a), rough milling b), cutting through the structure c), fixation on tungsten tip d) and sample holder e). Final shape of the lamella from the side-view f) and the top-view g).

2.2.3 Transmission Electron Microscopy

At a very rough approaching, the Transmission Electron Microscope (TEM) can be compared with optical microscope. Instead of light, TEM uses high-energy electrons as primary agent for sample imaging. The primary electrons are crossing through the sample and their mutual interactions result in a magnified image of the sample formed on the screen. TEMs are capable of imaging at significantly higher resolution than light microscopes, owning to the small de Broglie wavelength of electrons. This enables to examine fine details of sample. In addition, a TEM can be operated in several different modes as a High Resolution Transmission Electron Microscopy (HRTEM), a Scanning Transmission Electron Microscopy (STEM) and Analytical Electron Microscopy (AEM). Such a broad range of techniques used in this tool offers a complete characterization of materials at nanoscale, and we will introduce them individually in the following chapter.

The main principle of TEM lies in the interaction of the electron beam with the matter, similar as for SEM. The high-energy electron beam is entering the sample in form of thin lamella and crossing through it, which leads to the generation of different kinds of signals, as it is displayed in Fig. 2.8. Depending on the signal origin, detection devices are suitably adjusted, in order to obtain complex information about the observed sample. In the same way as for SEM, the primary electron beam generates SE, BSE, Auger electrons and X-rays, however, generally, only X-rays signal is detected in TEM. The attention is focused on electrons transmitted and scattered through the thin sample and thus, direct beam and elastically/inelastically scattered electrons.

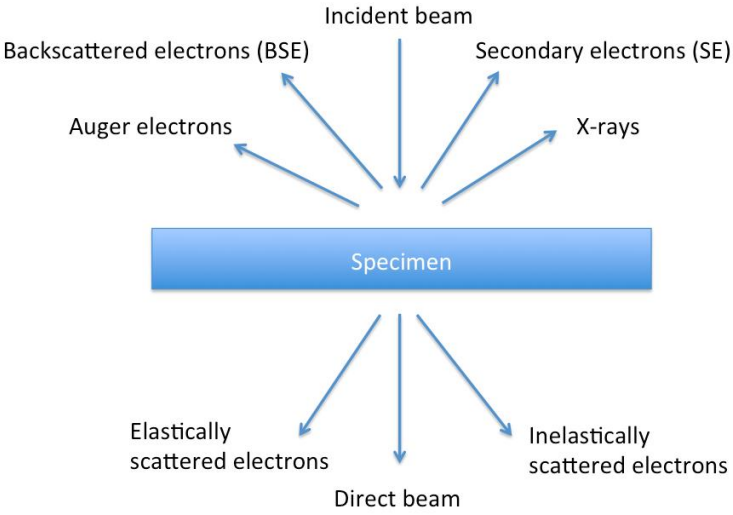

Fig. 2.8 Signals generated by an interaction of the beam of high-energy electrons with a thin specimen.

Although the electron gun is of similar composition as SEM one (thermionic, Schottky field emission and autoemission – cold field emission), it operates at higher energies (hundreds of keV) so that electrons are able to pass through the specimen. Moreover, the illumination system is more complicated, as it is shown in Fig. 2.9. The emitted electrons are focused to a gun crossover by applying potential on a Wehnelt cylinder. The accelerated electron beam is passing through two condenser lenses, where the first one (C1) forms an image of the gun crossover. If the second lens (C2) is focused to produce the image of the C1 crossover at the front-focal plane (FFP) of the upper-objective polepieces, then a parallel beam of electrons formed by the lens enters the sample. The described mode is so-called parallel-beam operation in TEM. Subsequently, the direct and diffracted beams are focused by a sequence of lenses – lower-objective polepieces, intermediate lenses and projector lenses to final image on fluorescence screen [11, 22].

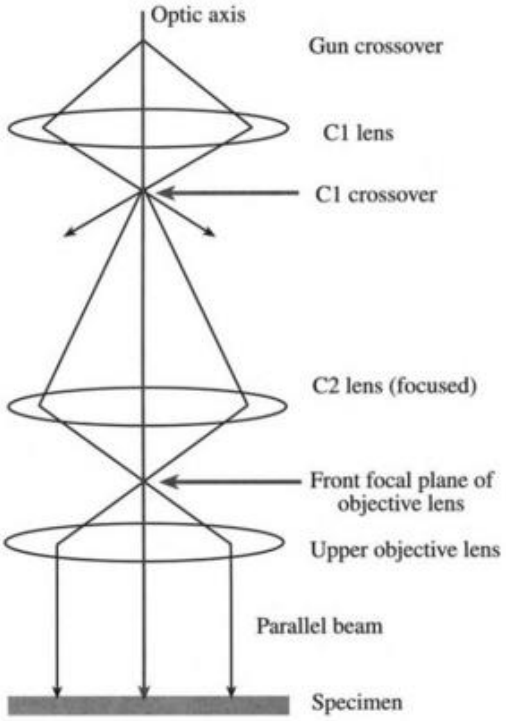

Fig. 2.9 Parallel-beam operation mode in TEM; taken from [22].

When the high-energy electron beam with wavelength of a few thousands of nanometer is passing through crystalline specimen, the atoms in solid matrix can act as a diffraction grating to the electrons. Thus, fraction of them will be scattered to particular angles, determined by the crystal structure of the specimen, while others continue to pass through the sample without deflection. Depending of the beam character, we call it diffracted or direct beam, respectively. After electrons have left the specimen, they pass through the electromagnetic objective lens, which collects all electrons scattered from one point of the sample in one point on the fluorescence screen, causing an image of the sample to be formed. Instead of image formation on the fluorescence screen, the diffraction pattern can be displayed by projection of the back focal plane onto the screen.

Depending on the nature of beams selected for the image formation, we can distinguish between bright field (BF), dark field (DF) and central dark field (CDF) imaging. By the objective aperture insertion under the lower-objective polepieces in the back focal plane of the objective, we are able to select or block the direct or diffracted electrons. In the BF mode (Fig 2.10 a), the aperture allows only the direct

beam to pass. In this case, the image results from a weakening of the direct beam by its interaction with the sample. Therefore, mass-thickness and diffraction contrast contribute to image formation: thick areas, areas in which heavy atoms are enriched, and crystalline areas appear with dark contrast. On the other side, regions with no sample in the beam path appear bright, hence the term “bright field”. In the DF images (Fig 2.10 b), the direct beam is blocked by the aperture, while one or more diffracted beams are allowed to pass the objective aperture. Since diffracted beams have strongly interacted with the specimen, very useful information is present in DF images, e.g., about planar defects, stacking faults or particle size [23]. As it is shown in Fig 2.10 b, the electrons that are selected by the aperture travel off the optic axis, since the aperture is displaced to select the scattered beam. The more off-axis the electrons are the greater aberrations and astigmatism they suffer [22]. Therefore, such a displacement is usually replaced by tilting the incident beam via potentiometers above the objective lens so that the chosen scattered-electron beam moves toward the central, on-axis position.

To obtain the lattice images, a large objective aperture has to be selected that allows many beams including the direct beam to pass (Fig. 2.10 c). The image is formed by the interference of the diffracted beams with the direct beam (phase contrast). If the point resolution of the microscope is sufficiently high and a suitable crystalline sample oriented along a zone axis, then High Resolution TEM (HRTEM) images are obtained. In many cases, the atomic structure of a specimen can directly be investigated by HRTEM. However, the interpretation of HRTEM images has to be confirmed by image simulation [23] (e.g., JEMS program [24]).

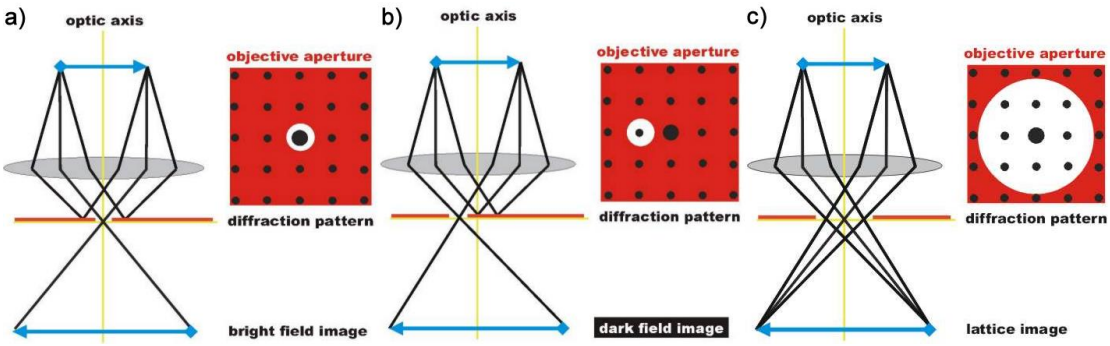

Fig. 2.10 Diagrams showing the selection of electron beams in BF a), DF b) and HRTEM c) mode of TEM; taken from [23].

In STEM mode, a condensed beam is used to probe the sample point by point. We work in so-called convergent-beam operation in TEM, as the beam is condensed in order to achieve the smallest probe. The practical situation of an illumination system in the most TEMs is displayed in Fig. 2.11. The condenser lens (C1) forms an image of the gun-crossover, as in the parallel-beam mode. However, contrary, the condenser lens C2 is switched off, while the C2 aperture still controls the convergence angle of the beam on the specimen. If the objective lens is split into two polepieces with separate coils, the upper polepiece can play a role of a condenser lens (C3) and focus the beam on the specimen [22]. Moreover, the double deflection lenses are used to deflect the beam during scanning over a defined area of the sample. At each spot, the generated signal is simultaneously recorded by selected detectors, building up an image. Furthermore, such a convergent beam is used to gain a highly localized signal from the specimen in analytical TEM (e.g. EDX, EELS). Indeed, it is possible to obtain EDX and/or EELS linescans and maps simultaneously with the STEM images, allowing direct correlation of images and quantitative data.

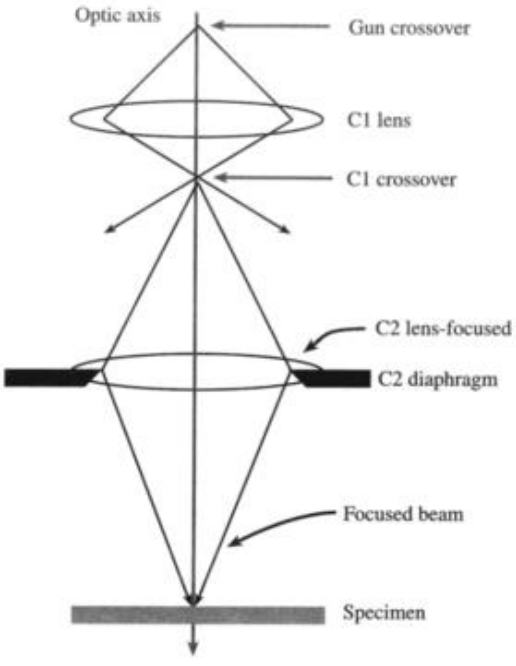

Fig. 2.11 Convergent-beam operation mode in TEM; taken from [22].

The analogy to the BF and DF TEM is drawn in the STEM by selecting the direct or scattered beams in an equivalent way but use detectors rather than apertures. In order to obtaine the BF or DF STEM image, a BF on-axis detector or an annular DF (ADF) detector, which surrounds the BF detector, is inserted in a plain that is conjugated with the back focal plane. It is possible to control which electrons fall on which detector and thus contribute to the image and its contrast [22].

TEM characterisation was performed inside the technical platform called ARCEN (Applications, Recherche, Caractérisation à l'Echelle Nanométrique) of the University of Burgundy. TEM observations were carried out using a JEOL 2100 FEG UHR microscope with 200 kV accelerating voltage. The images obtained in conventional parallel-beam mode and in HRTEM mode were acquired by a GATAN CCD Ultrascan camera. The point resolution in HRTEM mode is down to 0.19 nm (lattice resolution of 0.10 nm) and 0.20 nm in STEM mode. All STEM images presented in here were acquired by ADF detector. The image post-processing, as distances and angles measurement, was done by Digital Micrograph Software 2 (GMS2).

2.3 Spectroscopic methods

Electron microscopy, TEM as well as SEM, provides information about the morphology and structure of a specimen down to atomic scale. While due to the material contrast, we have some knowledge about the composition of elements, such information is in many cases insufficient. Therefore, methods that are sensitive to exact atomic number of atoms are needed.

Analytical Electron Microscopy (AEM) includes techniques, which are able to detect the local chemical composition. By interaction of an electron beam with the matter, complex signals are produced. In both TEM and SEM, X-rays and Auger electrons are formed. Whereas Auger electrons have very weak signal and their yield is decreasing with an increasing atomic number, X-rays have opposite properties and they can be detected in order to obtain information about the specimen atomic composition. On the other side, for light elements, the Electron Energy Loss Spectroscopy (EELS) technique is used preferentially.

Besides the spectroscopies implemented in electron microscope devices giving local information, supplementary integral spectroscopic technique, X-ray Photoelectron Spectroscopy (XPS), is used to complete knowledge about the chemical structure and composition of the sample. All used spectroscopic methods will be briefly described in the following sections.

2.3.1 Energy Dispersive X-ray Spectroscopy

When a primary electron enters a specimen, it can be scattered inelastically by an inner-shell electron of the matter. It leads to transition of electron to the higher-energy orbit leaving a hole in the inner-shell. This excited state is not stable, and an electron from a higher-energy level makes a downward process, which fills the hole in the inner-shell. The de-excitation can be released in form of characteristic X-ray photon whose energy depends on the atomic number Z of the involved atom and on the quantum numbers (n_i) of energy levels involved in the electron transition. The energy levels are historically marked as K for (n_1), L for (n_2), M for (n_3), etc.

The detection of X-rays by Energy Dispersive X-ray Spectroscopy (EDX) results in a spectrum of characteristic peaks of transfers between individual shells. An example of an EDX spectrum is shown in Fig. 2.12. Each element contained in the sample gives rise to at least one characteristic peak. Heavy (high-Z) elements show several peaks (K, L, M, etc.), which can be overlapped with others. Therefore, the quantification may be complicated. Moreover, characteristic peaks in the EDX spectrum are superimposed on a continuous background that arises from the Bremsstrahlung process [11].

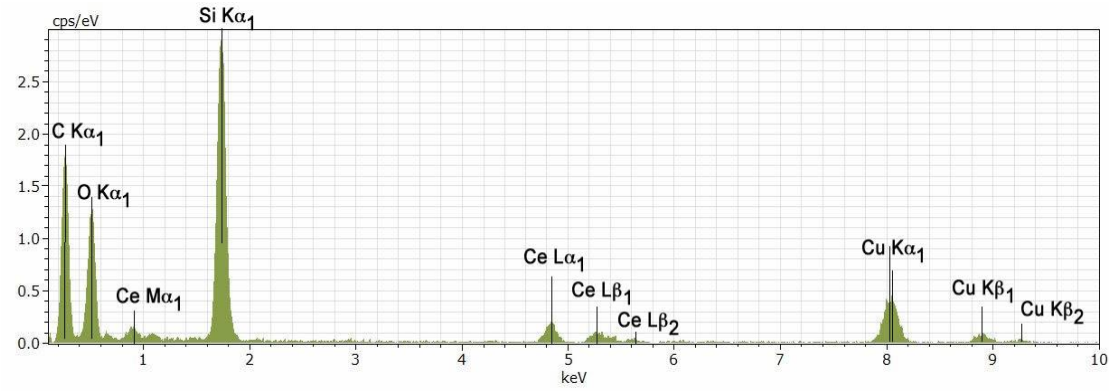

Fig. 2.12 Example of an EDX spectrum of CeO_2.

As it was sketched in Fig. 2.2, the emission depth of X-rays is several micrometers for electron energy about 30 kV in case of SEM. It means that the method in not solely a surface technique. As regards the thin layer specimen (less than 100 nm) the signal originates from the support as well [11]. The X-ray intensity for very thin specimen observed in TEM is several times lower as for SEM; thus, a compromise between the sufficient sample thickness for TEM observation, the acquisition time and X-ray signal intensity enough to detection must be done.

For EDX analysis a BRUKER Quantax XFlash® 5030T SDD detector implemented in the TEM JEOL 2100 FEG was used. The acceptance angle is 0.13 sr and the probe diameter in STEM mode can vary in range 0.5 – 2.5 nm.

2.3.2 Electron Energy Loss Spectroscopy

The approach to microanalysis can also be performed by Electron Energy Loss Spectroscopy (EELS) through the installation of a GATAN Imaging filter (GIF) below the TEM column (Fig. 2.13). The main principle of the method lies in the detection of energetic losses of the electron beam passed through a thin specimen. Because these electrons are responsible for inelastic interactions, which lead to X-rays and Auger electrons formation, they carry atomic-number information in form of energy losses. In addition, amount of electrons with loss is equal to sum of X-ray photons and Auger electrons; therefore, the signal is intense enough to detect the light as well as heavy elements.

In order to detect the small differences in kinetic energy of electrons, a magnetic prism with highly uniform magnetic field between two parallel faces of an electromagnet is used. The electrons with the same energy are focused at the exit of the spectrometer to form an electron energy loss spectrum of the specimen. This spectrum is usually recorded by a CCD camera (see Fig. 2.13).

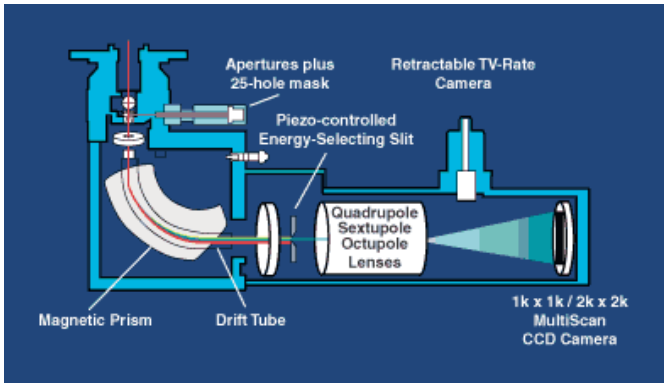

Fig. 2.13 Scheme of the GIF system, provided by GATAN; taken from [25].

An example of an EELS spectrum is shown in Fig. 2.14, where three typical regions are marked. The most intense signal is the zero-loss peak, representing electrons that were scattered elastically or remained unscattered while passing through the specimen. The area of energy losses below 50 eV known as plasmon excitations occurs. It represents the inelastic scattering by outer-shell electrons in form of collective oscillation. The inelastic excitation of inner-shell electrons causes an increase in energy losses at ionization edge; this ionization energy is characteristic for each particular element and the electron shell [11]. For example, the energy loss close to 530 eV corresponds to the *K* edge of oxygen whereas the losses at 884 eV and 901.6 eV correspond to the M_5 and M_4 edges of cerium, respectively [26]. Moreover, from the shape of the ionization edge it is possible to set the chemical surrounding of detected element, e.g. carbon in diamond-like structure has different features than graphite-like one [27]. The typical energies of core-loss and plasmons excitations as well as the shape of a spectrum for each element can be found in the EELS atlas [25].

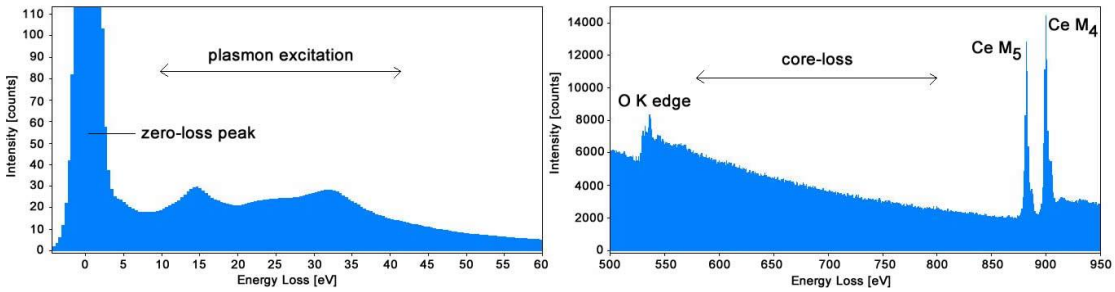

Fig. 2.14 Example of an EELS spectrum of CeO_2 with low and core losses.

A Gatan Imaging Filter (GIF) aperture of 2 mm with energy dispersion of 0.3 eV per channel was used to acquire EELS spectra. A probe of 1 nm or 1.5 nm was scanned through a specimen with short acquisition time (about 1 s) in order to minimize the electron-beam damage of sample. The energy resolution is down to 0.8 eV. The specific conditions will be mentioned for each spectrum afterwards.

Spectra post-processing was done by Digital Micrograph (DM) software [28]. For the cerium oxidation state calculation, the following evaluation method was used. The background intensity at the Ce $M_{4,5}$ edges was subtracted by fitting an inverse power-law for a range of 40 eV before the M_5 edge (820-860 eV) and extrapolating this function to higher energies. Among several proposed methods [29-32], we have chosen the second derivative method for EELS linescan and map evaluations. It was calculated numerically using DM software [28]. The second derivative method is particularly useful when dealing with sharp 'white lines' as the choice of the window over which integrating the peak area is essentially automatic; we have taken the positive area. Then, using our own DM script, the ratio between the M_5 and M_4 peak areas of the second derivative was calculated.

2.3.3 X-ray Photoelectron Spectroscopy

Principle of X-ray Photoelectron Spectroscopy (XPS) is based on photoelectric effect. Electrons, herein called the photoelectrons, are emitted from matter as a result of electromagnetic radiation absorption. The X-rays with particular energy ($h\nu$) irradiates the sample surface and excites an electron of the sample atoms from its initial state (E_b). The excited electron is traveling through the sample to the surface and by overcoming the energy barrier, a material work function (Φ) for electron emission, is reaching vacuum. The kinetic energy of emitted photoelectrons

(E_k) is detected by energy analyser. For conductive samples in electrical contact with spectrometer, the work function of spectrometer (Φ_s) can be used instead of the work function of material. This work function is usually determined from calibration measurement using gold reference. The energy balance can be expressed by diagram displayed in Fig. 2.15 or by equation as follows:

$$E_b = h\nu - (E_k + \Phi_S) \tag{2.1}$$

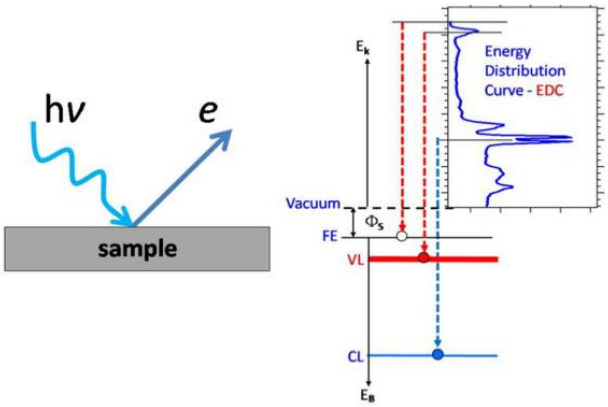

Fig. 2.15 Basic principles of XPS; taken from [12].

As a result, the spectrum (Fig. 2.16) composed of peaks as a function of binding energies can be acquired. The binding energy of excited electron is characteristic for each element and each core atomic orbital, thus it reflects the electronic structure of a specimen. Moreover, the intensity of peaks is related to the concentration of element in irradiated region. In addition, the photoionisation process leads to not only the emission of core-level electrons, Auger electrons are also acquired.

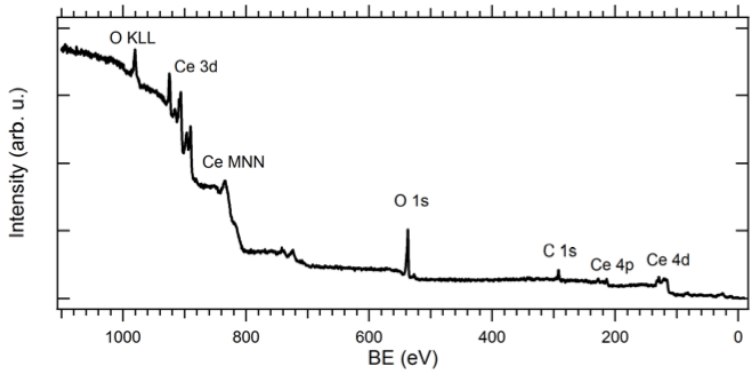

Fig. 2.16 Example of XPS wide spectrum of CeO_2; taken from [3].

XPS is of the most widely used surface spectroscopic technique for elemental composition, chemical and electronic state determination. The method is very surface sensitive, the photoelectrons excited and emitted to vacuum originate from within the 1-5 nm topmost region of of the sample. The information depth is generally depending on photon energy and sample material. In case of a nanoporous catalyst, acquired signals contain substantial contribution of surface based information. More detailed description of XPS technique can be found elsewhere [33, 34].

A laboratory XPS system working in UHV conditions at a base pressure of 2.10^{-8} Pa equipped with a SPECS Phoibos MCD 9 hemispherical electron analyser and a dual Mg/Al K_α X-ray source was used. XPS spectra at normal photoelectron emission geometry using a photon excitation energy of $h\nu$ = 1486.6 eV (Al K_α) with a total energy resolution of ΔE = 1 eV were acquired.

Analysis of XPS spectra needs background subtraction at first, followed by the spectra decomposition. The Shirley background subtraction was used in most of cases; however 45 eV breadth of the Ce 3d spectra causes that high binding energy side of the spectra is influenced by an inelastic background which is not taken into account. For this reason to analyze the Ce 4f electronic states, deconvolution of the Ce 3d spectra was carried out using the procedure employed by Skala *et al.* [35].

Bibliography of Chapter 2.

[1] K. Seshan, Handbook of Thin-film deposition Processes and Techniques, *William Andrew Publishing*, New York, USA, (2002), ISBN 0-8155-1442-5.

[2] P.M. Martin, Handbook of Deposition Technologies for Films and Coatings: Science, Applications and Technology, *William Andrew Publishing*, New York, USA, (2009), ISBN 978-0-8155-2031-3.

[3] M. Vorokhta, Doctoral thesis - Investigation of Magnetron Sputtered Pt-CeO_2 Thin Film Catalyst for Fuel Cell Applications, *Charles University in Prague*, Czech Republic (2013).

[4] S. Haviar, Doctoral thesis - Příprava a charakterizace nanostruktur pro katalýzu a detekci plynů, *Charles University in Prague*, Czech Republic (2014).

[5] R. Fiala, M. Vaclavu, M. Vorokhta, I. Khalakhan, J. Lavkova, V. Potin, I. Matolinova, V. Matolin, *J. Power Sources* 273 (2015) 105.

[6] E.P. Domashevskaya, O.A. Chuvenkova, S.V. Ryabtsev, Yu.A. Yurakov, V.M. Kashkarov, A.V. Shchukarev, S.Yu. Turishchev, *Thin Solid Films* 537 (2013) 137.

[7] A. Martel, F. Caballero-Briones, P. Quintana, P. Bartolo-Peerez, J.L. Pena, *Surf. Coat. Technol*. 201 (2007) 4659.

[8] M. Dubau, J. Lavkova, I. Khalakhan, S. Haviar, V. Potin, I. Matolinova, V. Matolin, *ACS Appl. Mater. Interfaces* 6 (2014) 1213.

[9] M. Dubau, J. Lavkova, V. Potin, I. Matolinova, V. Matolin, *Manuscript*.

[10] M. Vorokhta, I. Khalakhan, I. Matolinova, M. Kobata, H. Yoshikawa, K. Kobayashi, V. Matolin, *Appl. Surf. Sci.* 267 (2013) 119.

[11] R.F. Egerton, Physical Principles of Electron Microscopy, *Springer*, New York, USA, (2007), ISBN 978-0387-25800-0.

[12] I. Khalakhan, Doctoral thesis - Preparation and Characterization of Novel Oxide Catalysts for Fuel Cell Applications, *Charles University in Prague*, Czech Republic (2013).

[13] L.A. Giannuzzi, F.A. Stevie, Introduction to Focused Ion Beams, *Springer*, Boston, USA, (2005), ISBN 0-387-23116-1.

[14] N. Yao, Focused Ion Beam Systems, *Cambridge University Press*, Cambridge, United Kingdom, (2007), ISBN 978-0-521-83199-4.

[15] Software SRIM and TRIM, J. Ziegler, available online: www.srim.org

[16] S. Rubanov, P.R. Munroe, *J. Microsc.* 214 (2004) 213.

[17] N. Chekurov, K. Grigoras, A. Peltonen, S. Franssila, I. Tittonen, *Nanotechnology* 20 (2009) 065307.

[18] R.M. Langford, C. Clinton, *Micron* 35 (2004) 607.

[19] L.A. Giannuzzi, F.A. Stevie, *Micron* 30 (1999) 197.

[20] J. Li, T. Malis, S. Dionne, *Mater. Charact.* 57 (2006) 64.

[21] M. Krajnak, Bachelor thesis - Příprava lamel pro transmisní elektronový mikroskop (TEM) pomocí fokusovaného iontového svazku (FIB), *Charles University in Prague*, Czech Republic (2011).

[22] D.B. Williams, C. B. Carter, Transmission Electron Microscopy, *Springer*, New York, USA, (2009), ISBN 978-0-387-77502-0.

[23] ETH Zurich, http://www.microscopy.ethz.ch/elmi-home.htm

[24] P.A. Stadelmann, *Ultramicroscopy* 21 (1987) 131.

[25] C.C. Ahn, O.L. Krivanek, EELS Atlas: A Reference Collection of Electron Energy Loss Spectra Covering All Stable Elements, *Gatan*, Warrendale, USA, (1983), available through Gatan DMS software.

[26] L.A.J. Garvie, P.R. Buseck, *J. Phys. Chem. Solids* 60 (1999) 1943.

[27] J. Roberston, *Mater. Sci. Eng., R* 37 (2002) 129.

[28] Gatan Inc., Digital Micrograph, www.gatan.com

[29] R.F. Egerton, Electron Energy-Loss Spectroscopy in the Electron Microscope, *Plenum Press*, New York, (1996), ISBN 978-1-4419-9582-7.

[30] C.C. Calvert, A. Brown and R. Brydson, *J. Electron. Spectrosc. Relat. Phenom.* 143 (2005) 173.

[31] T. Riedl, T. Gemming and K. Wutzig, *Ultramicroscopy* 106 (2006) 284.

[32] R. Arenal, F.de la Penna, O. Steephan, M. Walls, M. Tencee, A. Loiseau and C. Colliex, *Ultramicroscopy* 109 (2008) 32.

[33] J.F. Watts, J. Wolstenholme, An Introduction to Surface Analysis by XPS and AES, *Wiley*, London, UK, (2003), ISBN 0-470-84712-3.

[34] S.K. Sharama, X-Ray Spectroscopy, *InTech*, Rijeka, Croatia, (2012), ISBN 978-953-307-967-7.

[35] T. Skala, F. Stutara, K.C. Prince, V. Matolin, *J. Electron Spectrosc. Relat. Phenom.* 169 (2009) 20.

3 Results and Discussion

This chapter summarizes the results of an investigation of the catalytic thin film layers based on platinum doped cerium oxide prepared by magnetron sputtering, which were obtained through a fundamental approach and a fuel cells applied research. In order to reach a higher efficiency for the catalyst material, the production of structures with high specific surface area was highly favourable.

First, in Section 3.1 Catalyst Support Chacterization, the attention is given on catalyst substrate material and its characterization. The carbon materials with different composition are used as the support. Then, we have shown that the cerium oxide layers deposited by magnetron sputtering on the carbon substrates exhibit a complex porous columnar structure contrary to the relatively flat layers deposited on silicon substrates. To obtain porous structures, the CeO_x thin layers were deposited via magnetron sputtering in oxygen/argon atmosphere on different types of carbon substrates. The structure and composition of these porous nanostructured cerium oxide layers on the carbon films are studied in detail in Section 3.2 Cerium Oxide Layers. By adding well dispersed platinum (Section 3.3 Platinum Doped Cerium Oxide Layers), we have created the complex system, which can be applied in PEMFC as the real catalyst for the anode side (Section 3.4 Catalyst layer application in PEMFC).

3.1 Catalyst Support Characterization

In Section 1.3 Support of Catalyst, the great importance of catalyst support was demonstrated. Herein, we present four systems used as a substrate for the preparation of ceria-based catalytic layers as thin films:

- *Silicon wafer (Si)*
- *Graphite foil (C-foil)*
- *Amorphous carbon (a-C)*
- *Nitrogenated carbon (CN_x)*

3.1.1 Morphology and Structure of Catalyst Support

3.1.1.1 As-Prepared Layers

- *Silicon wafer* (*Si*)

Pieces of (100)-oriented p-doped silicon wafers (thickness 0.5 mm) covered with a native oxide layer (amorphous SiO_2) were used as a catalyst support. The thickness of silicon oxide was ranged between 2-5 nm with completely flat surface.

In our previous research [1-7], we have shown that the Pt-CeO_x layer prepared via magnetron sputtering on Si grows compact and nonporous. Accordingly, by using a varnish method [5] and Atomic Force Microscopy (AFM) technique, we are able to set the thickness of a catalytic layer deposited on the top of silicon. Thus, the Si wafer with a ceria-based catalytic layer on the surface plays a role of reference system to study and compare the effects played by carbon substrates.

In addition, the Si substrate was also used as a support for sputter deposition of planar carbon films (see below).

- *Graphite foil (C-foil)*

A commercial graphite foil (Alfa Aesar, purity 99.8%, thickness 0.254 mm) was the second system used as a catalyst substrate. Fig. 3.1 presents an AFM image of the pure C-foil composed of atomically smooth graphite sheets with clearly visible hexagonal structure.

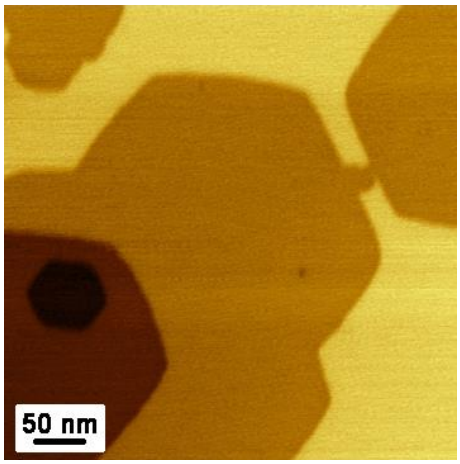

Fig. 3.1 High resolution AFM image of the pure C-foil.

- *Amorphous carbon (a-C)*

The sputtering method described in Section 2.1.1 Carbon Films Preparation was used for deposition of amorphous carbon films supported by the silicon substrate. The average thickness of all deposited layers was estimated to be close to 200 nm based on the deposition conditions; however, the real thickness might vary. A cross-section TEM image of as-prepared amorphous carbon layer is displayed in Fig. 3.2. The a-C film is continuous, nonporous, with rather flat surface, and the measured thickness was 170 ± 5 nm.

In order to study the a-C film structure, the cross-section samples were prepared by means of FIB from the 200 nm thick a-C films for TEM characterization. TEM images with different defoci were acquired (Fig. 3.3 a-e). Czigány *et al.* [8] have illustrated that the contrast variation is changed with focus, while the main features remain static. However, herein presented micrographs taken at high magnification do not present any visible structure. In addition, the patterns obtained by Fast Fourier Transformation (FFT) at Gaussian focus (Fig. 3.3 c) inset, almost no contrast) present typical features of an amorphous phase [9]. The concentric rings displayed for FFT of the defocused images (Figs. 3.3 a) and e),

insets) originate from nature of focusing and do not belong to the film structure. Therefore, we conclude that the carbon films are fully amorphous.

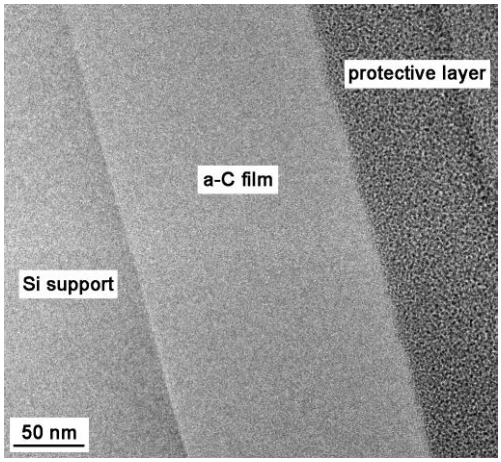

Fig. 3.2 TEM cross-section image of the a-C layer of 170 nm thickness.

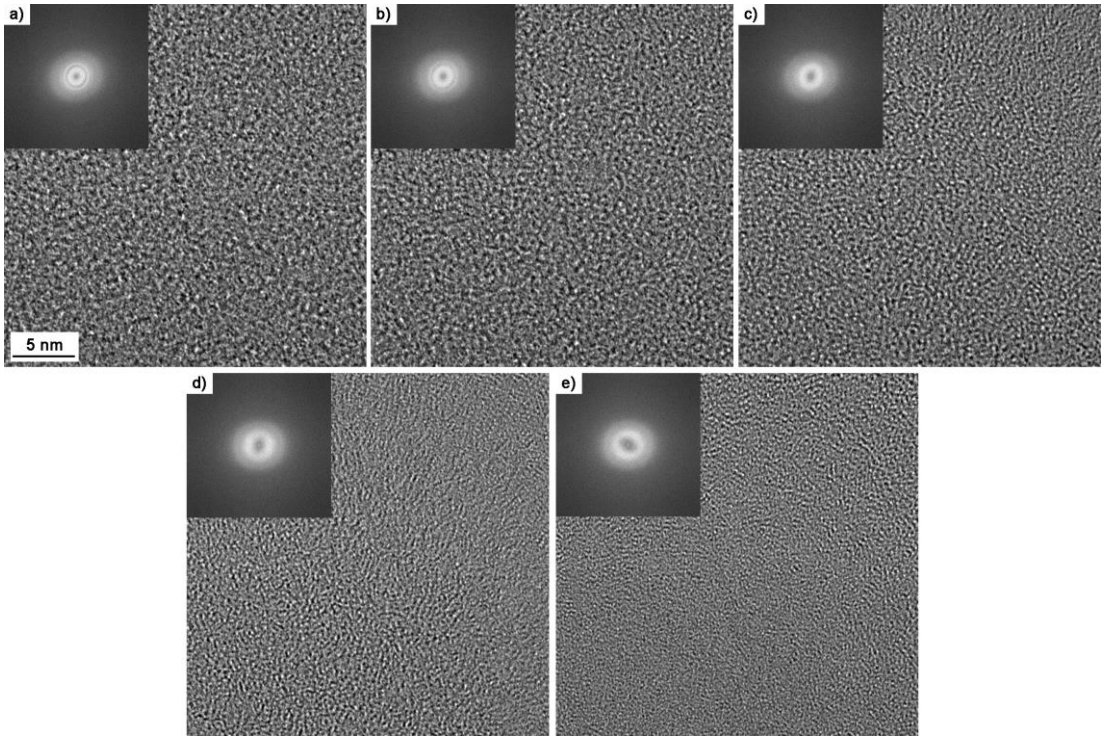

Fig. 3.3 HRTEM focus series of the a-C film saved at defocus of -100 nm a), -50 nm b), 0 nm (Gaussian focus) c), +50 nm d) and +100 nm e). Corresponding FFTs are inserted.

- *Nitrogenated carbon (CN_x)*

Likewise, the nitrogenated carbon films were prepared via magnetron sputtering. The deposition system allows to change the composition of working atmosphere, as it was mentioned in Section 2.1.1 Carbon Films Preparation. Nitrogen of various concentrations (5, 25, 50, 75 and 100%) in the carrier argon flow was injected into the chamber during the sputter deposition process in order to obtain nitrogenated carbon films with different compositions. The total gas pressure of nitrogen/argon mixture during the magnetron sputtering was 0.8 Pa for all nitrogen concentrations. In case of 100% nitrogen concentration in the working atmosphere the CN_x layers were mainly deposited at higher pressure of 4 Pa. Unless otherwise note, we consider under the CN_x 100% labelling pressure of 4Pa. Samples designation we used corresponds to the nitrogen concentration into the working gas (e.g. CN_x 100% means a nitrogenated carbon film prepared in pure nitrogen atmosphere). Fig. 3.4 displays a cross-section TEM image through the 190 nm thick CN_x100% film on silicon wafer. In comparison with the a-C layer, the CN_x100% thin film surface is rougher, as confirmed in our recent study [10] by means of the AFM roughness measurement.

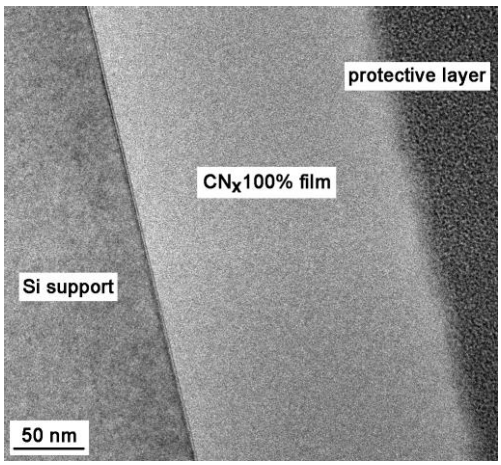

Fig. 3.4 TEM cross-section image of the CN_x100% layer of 200 nm thickness.

In order to investigate the influence of nitrogen concentration, varied from 5% up to 100% in working gas during the reactive magnetron sputtering, on the nitrogenated carbon films structure, the cross-section samples prepared by means of FIB from the 200 nm thick CN_x films were observed in TEM. The HRTEM images saved close to the Gaussian focus are presented in Fig. 3.5. For each sample was

used the same image processing as in case of the a-C film study; the Gaussian focus was found, then the images with several positive and negative defoci were taken, and the FFT processing was applied. All layers were found to be fully amorphous and did not display any special features.

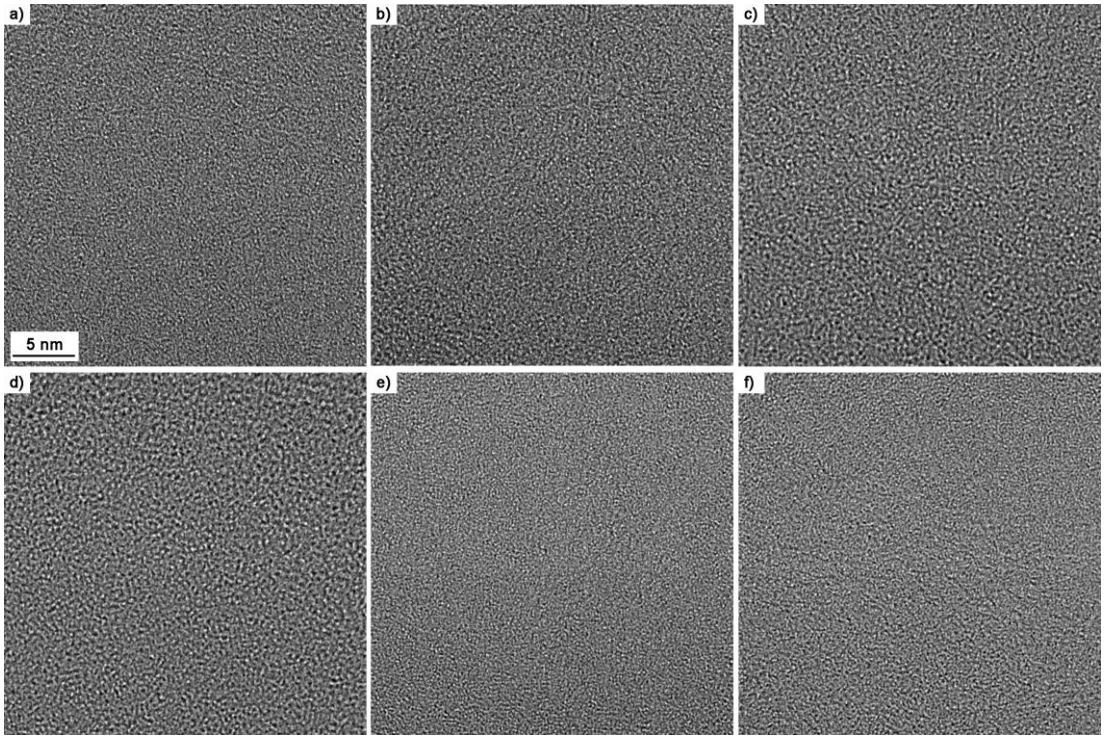

Fig. 3.5 HRTEM cross-section images, saved close to the Gaussian focus, of the CN_x thin films with various concentrations of nitrogen in the process gas during the magnetron sputtering: 5% a), 25% b), 50% c) 75% d), 100% (low pressure 0.8 Pa) e) and 100% (high pressure 4 Pa) f).

According to the literature [11, 12], the nitrogenated carbon films prepared by means of the reactive magnetron sputtering at the room temperature have been reported to exhibit solely an amorphous microstructure, see the diagram displayed in Fig. 3.6. This diagram points to facts that different preparation parameters and conditions as the substrate temperature and/or the nitrogen concentration are needed to obtain the structural changes of the CN_x films. Thus, we can conclude that the amorphous structure of the CN_x films prepared in the conditions mentioned in Section 2.1.1 Carbon Films Preparation is in a good agreement with previous observations [11].

To date a lot of researchers have paid attention to the fullerene-like structure observation due to their great hardness and elasticity [8, 9, 11-14]. In our work we

did not obtain any indication of the changes in the microstructure by using HRTEM imaging (Fig. 3.5). Moreover, the publications referring to the fullerene-like structure present results about carbon deposition at higher temperatures [8, 11, 12] or for deposition techniques different from the magnetron sputtering [9, 13, 14]. The main reason for the formation of the fullerene-like structure at the higher temperature is the structure evolution mechanism occurring in the chamber during the magnetron sputtering proposed by several groups [12, 13]. The N_2-containing atmosphere and the deposition flux from the carbon target lead to a large extent of multiatomic species formation. The studies have shown that plasma contains mainly N_2^+, N^+, CN^+, $(CN)_2^+$ and C^+ ions, whereas the CN species are created on the graphite target and sputtered off [13, 15, 16]. The CN molecules are adsorbed and stabilized on the top of the substrate surface due to the multiple bonds between C and N. Furthermore, the N_2 and C_2N_2 volatile gases formation is also active on the surface during the selective etching by the reaction of misaligned CN molecules and oncoming nitrogen species; i.e. the incorporated nitrogen seems to originate from the already formed CN molecules adsorbing on the substrate, while the nitrogen ions contained in the plasma approaching the substrate have caused chemical etching. Due to the desorption process, the amount of nitrogen in the CN_x film does not exceed 25%. If the temperature is decreasing, the mobility of carbon and nitrogen molecules is reduced, and an increasing number of nonaligned molecules are adsorbed. Moreover, the efficiency of the desorption process due to the chemical etching is lower. This results in the amorphization of carbon film [12]. Therefore, we suggest that the CN_x thin films prepared in our system at room temperature are fully amorphous, even though the concentration of nitrogen in the working gas has varied. Nevertheless, we cannot exclude structural ordering at low distances, discontinuities in the microstructure, presence of more or less ordered phases or any others changes in the film composition. Some compositional changes will be furthermore proven by spectroscopy techniques in the subsequent chapters.

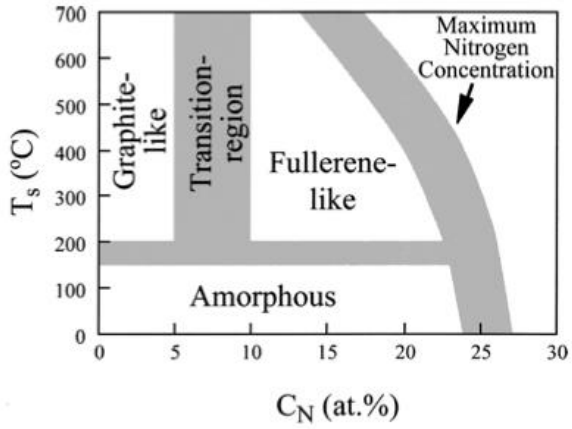

Fig. 3.6 Diagram displaying the structures observed in sputtered CN_x films for different substrate temperature and nitrogen concentrations. Taken from [11].

3.1.1.2 Carbonaceous Substrates after Oxygen Plasma Etching

For the purpose of examining oxygen plasma influence on carbon films, the samples of approximately 200 nm thick as-prepared a-C and CN_x100% layers supported by the silicon substrates have been simultaneously exposed to the oxygen plasma for different periods of time (10, 20, 30 and 40 min). The process gas consisted of pure oxygen at a total pressure of 20 Pa (for more details see Section 2.1.1 Carbon Films Preparation). In Fig. 3.7, the cross-section TEM micrographs of the a-C and CN_x100% films after the plasma treatment are shown. Significant changes in the thickness and roughness are observed for both carbonaceous films due to the material erosion caused by the oxygen plasma. After 10 minutes of plasma exposure, slight roughening of a-C surface is visible. As the treatment continues, the oxygen etching becomes destructive to a considerable extent for the a-C surface. As it can be seen, after 40 minutes of plasma treatment, the wavy structure of the a-C surface is eroded and the deep hollows structure is formed. In contrast to the a-C film, the surface roughening of the CN_x100% film can be undistinguished after 20 and 30 minutes of oxygen plasma exposure; the fine grainy surface is formed. However, although the effect of plasma on the CN_x100% surface roughening is slight, the main variations were observed for the film thickness. Twenty minutes of plasma treatment leads to the fading away of 100 nm CN_x100% film, and moreover, 40 minutes of etching was sufficient to remove off nearly the

whole 200 nm thick CN_x100% layer. Oppositely to the CN_x100% film, thinning of the a-C film is much slower.

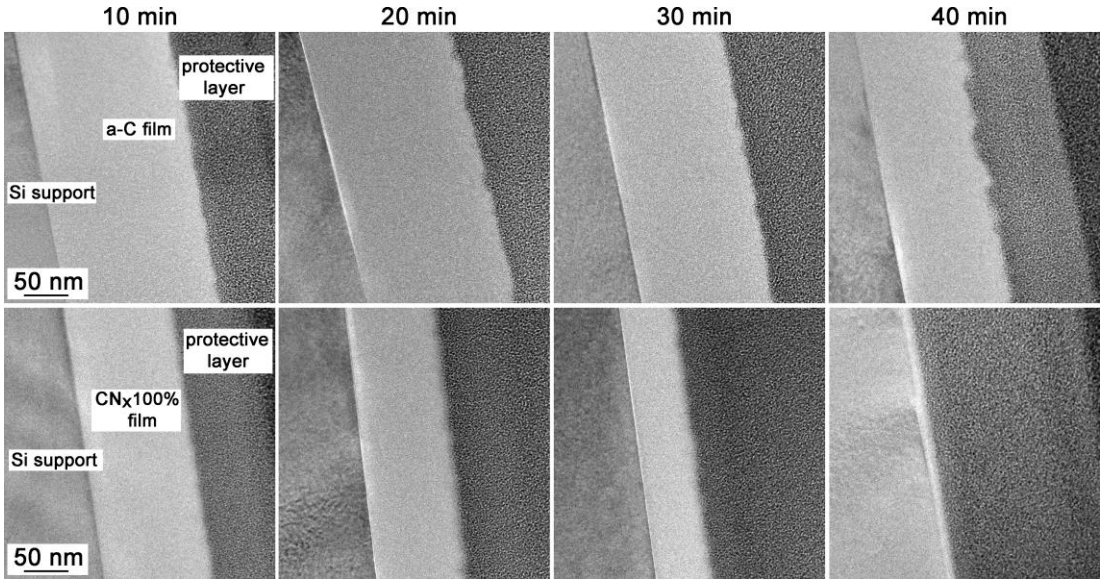

Fig. 3.7 TEM cross-section images of the a-C and CN_x100% films after 10, 20, 30 and 40 minutes of oxygen plasma treatment.

The results of the film thickness measurement from TEM cross-section images before and after oxygen plasma exposure as a function of different time are summarized in Table 3.1 and displayed in Fig. 3.8 for both the a-C and CN_x100% films, respectively. To conclude, the CN_x100% film is less resistant to the oxygen plasma treatment than the a-C film, although the surface roughening has shown major effect in case of the a-C layer.

Oxygen plasma etching time [min]	0	10	20	30	40
a-C film thickness [nm]	170	175	165	145	115
CN_x100% film thickness [nm]	190	125	100	60	10

Table 3.1 Thicknesses of the a-C and CN_x100% films as-prepared and after 10, 20, 30 and 40 minutes of oxygen plasma treatment.

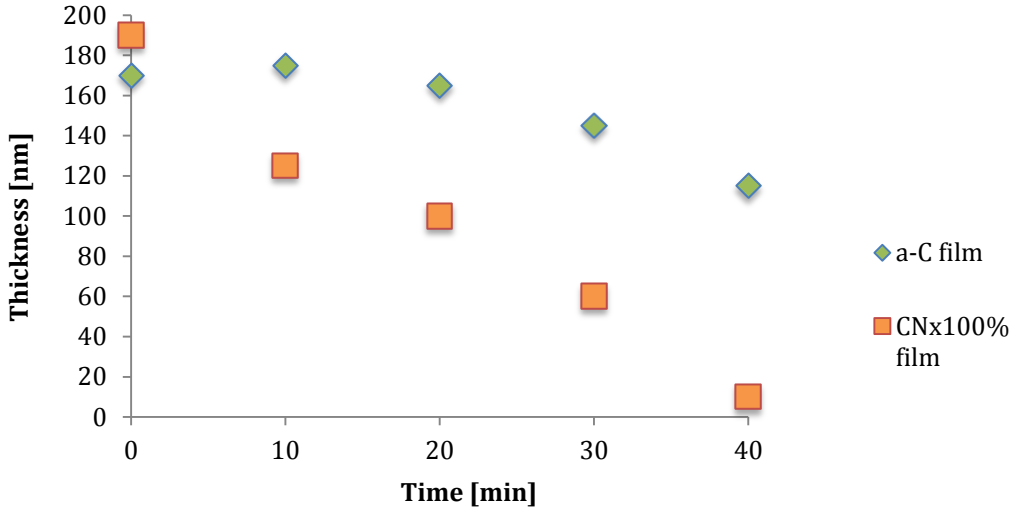

Fig. 3.8 Thicknesses of the a-C and CN_x100% films before and after oxygen plasma treatment.

The amorphous carbon film fading and observed surface erosion caused by the oxygen plasma treatment are presented in our studies [6, 10, 17]. The universally agreed etching mechanism resides in the reaction of carbon surface atoms with active oxygen species present in the oxygen plasma [18-20]. The chemical reaction occurring between oxygen plasma and carbon film leads to the formation of volatile carbon oxides (CO and CO_2). The gaseous species desorbed from the substrate remove carbon atoms causing material erosion and subsequently surface roughening [21, 22]. CO and CO_2 gases are piped away by the pumping system, as confirmed by using the mass spectroscopy technique during the reactive plasma etching of carbon substrates [18-20, 23]. Moreover, it was shown that a selective oxygen plasma etching occurs on the carbon substrates [22, 24]. The oxidation reaction in the oxygen plasma takes place first at the structural defects and edges of the carbon substrate [24]. In addition, in case of the a-C thin films, the carbon structure is not completely in the amorphous sp^2 phase; a fraction of sp^3 phase can be also contained. It was observed that the etching rate of sp^3 hybridized carbon is lower than for the sp^2 hybridized one [22, 25, 26]. Therefore, the selective etching of a-C film during the oxygen plasma treatment can result in the observed nonhomogeneous a-C film thinning, accompanied by higher surface roughening.

In case of the nitrogenated carbon films, the composition is even more complex. As it was mentioned above, CN species are adsorbed and stabilized on the

surface and thus, CN_x films consist of carbon and nitrogen with several different bonds between them [12]. More detailed description of bonding will be presented in the subsequent chapters. In general, by adding more nitrogen into the carbon film, the fraction of the sp^2 bonding states is increasing [9]. Due to the lower resistance of the sp^2 carbon phases against the oxygen etching, the CN_x layer is fading faster then the a-C film, which can be unambiguously seen in Fig. 3.8.

3.1.1.3 Carbonaceous Substrates after Cerium Oxide Layer Deposition

The effect of carbon surface erosion and its etching off caused by the oxygen plasma treatment take place also in case of magnetron sputter deposition of cerium oxide layers. Here, we show that the cerium oxide layers deposited by magnetron sputtering on the carbon substrates mentioned above (for preparation technique see Section 2.1.2. Catalyst Layers Preparation) have exhibited a complex porous columnar structure contrary to the relatively flat and compact layers on the silicon substrates [1-7]. An influence of different preparation parameters and conditions are discussed.

The CeO_x layers deposited on silicon play a role of reference samples as the cerium oxide layers grow continuous and nonporous way on that type of substrate. The formation of a compact cerium oxide layer makes possible to measure its thickness by means of the AFM measurement using the varnish method on silicon [5]. The method consists in masking part of the silicon substrate with tip prior to the cerium oxide deposition. After the deposition the mask is removed off, and the resulting step height corresponds to the thickness of deposited cerium oxide on the silicon substrate. Herein, the thickness is marked as a nominal thickness and it is use for sample designation. However, the real thickness of cerium oxide sputtered on the carbon substrates may differ.

An influence of several deposition parameters during cerium oxide sputtering on the catalyst structure modification was investigated. First, the attention was focused on deposition time. During the deposition the thickness of CeO_x layers is increasing with time leading to the morphology modification. Afterwards, the importance of the catalyst substrate is shown. Finally, variations in the deposition

rate and an influence of residual oxygen pressure in the chamber during the sputtering are studied.

3.1.1.3.1 Influence of Cerium Oxide Deposition Time

To investigate the structure evolution, the cerium oxide layers were deposited on a graphite foil for different periods of time. The deposition rate of cerium oxide was set as 1 nm.min^{-1}. The CeO_x was sputtered in pure argon atmosphere at a total pressure of 4.10^{-1} Pa. In this way, the series of the samples with various thicknesses were prepared. The morphology evolution is clearly seen in Fig. 3.9, where the SEM top-view micrographs are presented. At the beginning of the deposition (the nominal thickness of cerium oxide 0.5 – 1 nm), nuclei are formed, and only individual grains are visible. During the early stage of growth (1.5 – 5 nm), the grains start to increase, merge, and a fractal-like structure arises. With the further deposition (12 - 20 nm), the texture is thickened, and the SEM images show a columnar structure. In case of the 30 nm thick CeO_x layer, the structure of the deposited on the C-foil becomes more compact. The same character of growth was also observed in our previous studies for others carbonaceous materials like carbon nanotubes [1] or glassy carbon [6].

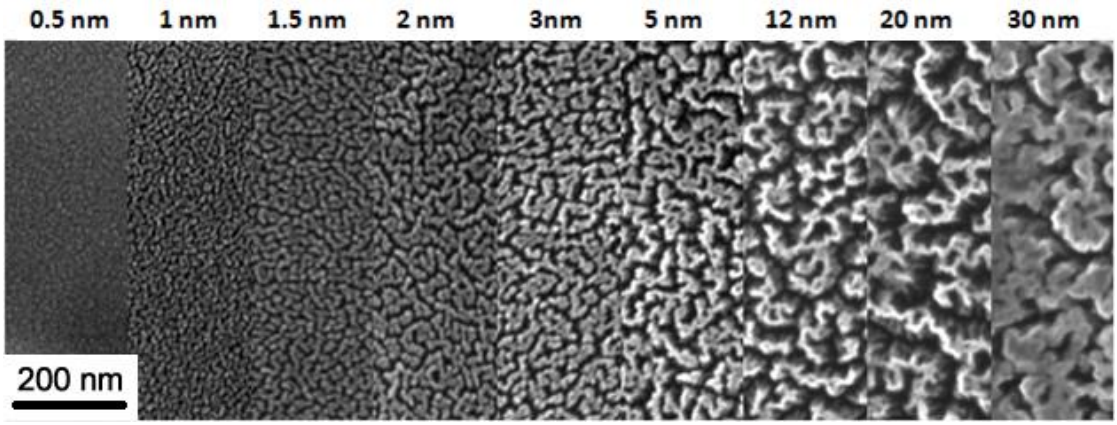

Fig. 3.9 SEM top-view micrographs of the morphology evolution for CeO_x layers deposited on the C-foil as a function of nominal thickness. Deposition rate of cerium oxide 1 nm.min^{-1}, residual oxygen pressure 4.10^{-4} Pa in Ar working atmosphere, total pressure kept at 4.10^{-1} Pa.

In order to perform TEM observation, three samples with nominal thicknesses of the CeO_x layers equal to 1, 5 and 20 nm (marked as CeO_x (1 nm)/C-foil, CeO_x (5 nm)/C-foil and CeO_x (20 nm)/C-foil) were chosen to prepare thin lamellas by means of FIB with the electron- and ion-beam assisted deposition of platinum or silicon as a protective layer. The TEM micrographs taken in ADF STEM mode are presented in Fig. 3.10. As one can see, the cross-section images confirm the morphology evolution described above and shown in Fig. 3.9. For CeO_x (1 nm)/C-foil (Fig. 3.10 a), the cerium oxide layer is non-continuous (bright line) with the separate grains in range about 3-4 nm in diameter. The C-foil surface below the catalyst layer is relatively flat, without any modification. Concerning the sample with the 5 nm thick deposited CeO_x layer, the hilly-like structure is visible at the first sight in Fig. 3.10 b). The surface roughness is high and the considerable transformation of C-foil has occurred. In addition, it is seen from material contrast that the hilly-like structure is formed by the carbon substrate and cerium oxide just copies created shapes. The total thickness of the formed porous structure was measured as 30 nm. For the sample marked as CeO_x (20 nm)/C-foil (Fig. 3.10 c), several columns composed of modified carbon decorated by cerium oxide were observed. The structure thickness on the C-foil, estimated as 100-120 nm, is more than 5 times higher as in case of the silicon substrate, where the CeO_x layer grows compact and nonporous [1].

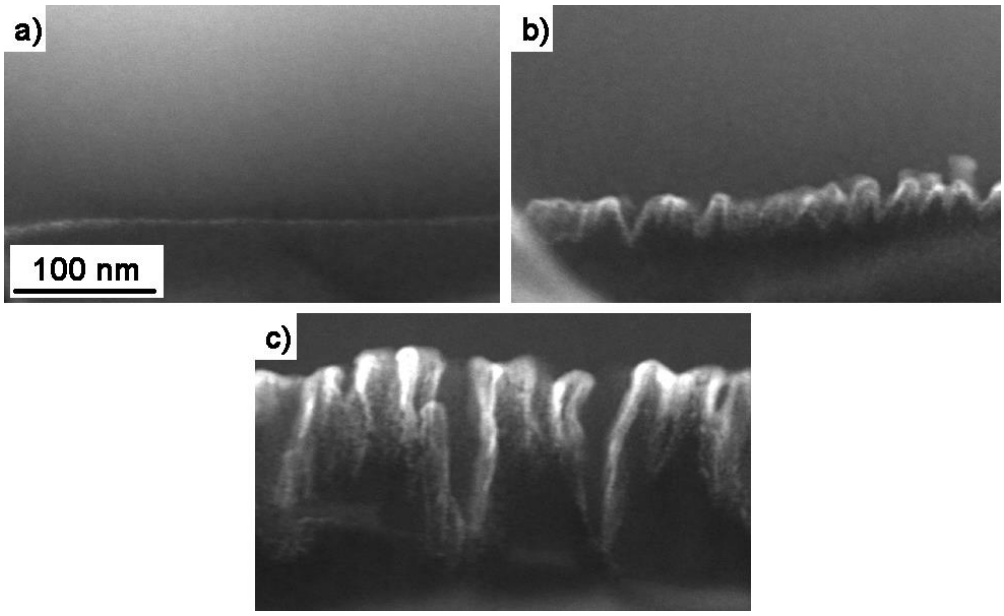

Fig. 3.10 Dark-field STEM cross-section images of the CeO_x layer on the C-foil substrate with the nominal thickness of 1 nm a), 5 nm b) and 20 nm c).

To verify the composition of the hilly-like structure formed during the cerium oxide magnetron sputtering process, the catalyst layer of the sample CeO_x (5 nm)/C-foil was washed out by using H_2SO_4 acid. Fig. 3.11 represents the micrographs before and after the CeO_x removal obtained by SEM and TEM, respectively. As one can see, the porous structure did not disappear, and the surface morphology seems to be changed very little. The pointed features (Figs. 3.11 a) and b) are rounded a bit as the CeO_x has been flushed out (Figs. 3.11 c) and d), although, the main structure remains static. Furthermore, in Fig. 3.11 d) showing the TEM image with higher magnification after the CeO_x removal, the carbon planes of the C-foil substrate are clearly visible. Any others crystals were not observed. It confirms that the hilly-like structure is created by carbon, and cerium oxide is present atop the carbon surface.

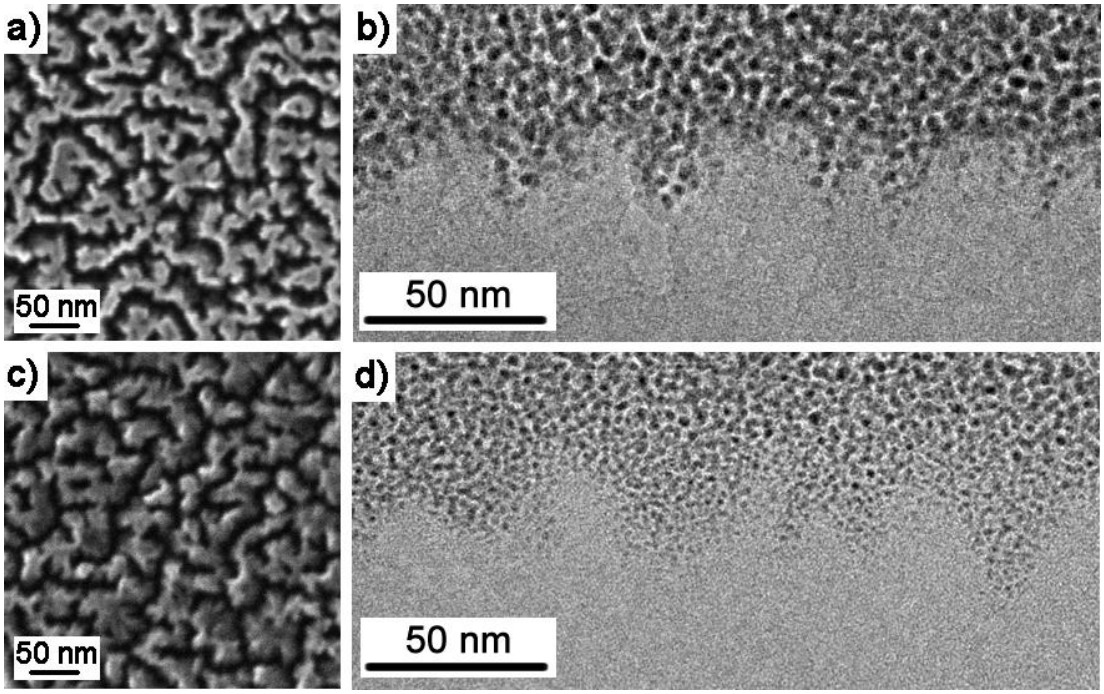

Fig. 3.11 SEM and TEM micrographs of the CeO_x (5 nm)/C-foil before a) and b) and after catalyst layer removal c) and d).

The above-presented results suggest that the carbon plays an active role in the catalyst porosity creation. Moreover, a phenomenon related to the sputtering deposition process of cerium oxide on the C-foil is crucial for an enlargement of the high specific surface area gaining. The main mechanism responsible for the porous structure formation leans on the equilibrium between the carbon substrate etching and the cerium oxide deposition. As shown in our studies [10, 17, 27], during the

magnetron sputtering of cerium oxide the oxygen plasma is formed as a result of oxygen added to working gas and/or the residual atmosphere inside the chamber in case of deposition in pure argon. The oxygen species present in the plasma interact with the carbon substrate that leads to the volatile carbon oxides formation [18-20, 23] and consequently, to the erosion of the surface. The process is similar to the oxygen plasma exposure solely (see Section 3.1.1.2 Carbonaceous Substrates after Oxygen Plasma Etching). Because of the simultaneous CeO_x deposition, the mechanism can be described as follows; at the early stage of growth, the small amount of cerium oxide is sputtered on the carbonaceous substrate (nominal thickness 0.5-1 nm). Individual nuclei are formed and it results in fine grainy and non-continuous layer, as it is visible in Fig. 3.9. As these grains are resistant to the oxygen plasma etching, they play a role of shielding mask for underlying C-foil. With the further magnetron sputtering process, the unprotected parts of C-foil are exposed to the oxygen plasma treatment, and the etching of carbon substrate occurs. As a consequence, carbon fades, and deep hollows are created. Moreover, the subsequent deposition of cerium oxide causes the grains merging, the caps atop increasing and therefore, the hilly-like structure formation (Figs. 3.9, 3-5 nm and 3.10 b). Since the deposited layer of cerium oxide is thicker, the structure becomes more compact (Fig. 3.9, 30 nm) and the further etching of carbon substrate cannot occur. In addition, we have shown that the modified carbon surface is stable and keeps the porous structure after the CeO_x removal (Figs. 3.11 c) and d). Thus, we can conclude that the carbon surface roughening and the porous structure formation are the result of the complex processes occurring during the CeO_x magnetron sputtering including the cerium oxide deposition and oxygen plasma etching. The above described growth model is summarized in Fig. 3.12.

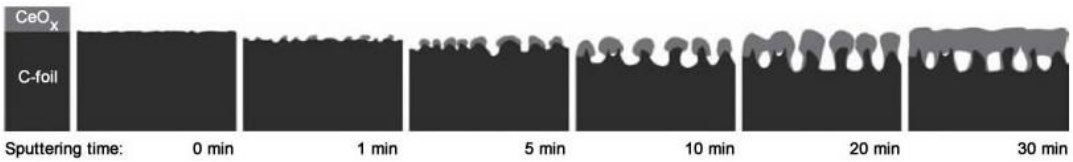

Fig. 3.12 Proposed model of the growth process of CeO_x/C-foil as a function of cerium oxide deposition time, taken from [17].

3.1.1.3.2 Influence of Different Carbonaceous Catalyst Support

- *Amorphous carbon (a-C) vs. nitrogenated carbon (CN_x100%) films*

In order to confirm the idea of carbon fading during the magnetron sputtering of cerium oxide due to the oxygen plasma etching, thin films of amorphous carbon and nitrogenated carbon were deposited on the silicon support. The as-prepared carbonaceous layers thicknesses were measured from the TEM images as 170 nm for a-C and 190 nm for the CN_x100% film, respectively. Subsequently, CeO_x layers with the nominal thicknesses of 5, 20 and 30 nm were sputtered onto. The deposition rate of cerium oxide was estimated to be close to 0.4 $nm.min^{-1}$. For a better control of the oxygen plasma influence, cerium oxide was sputtered in oxygen/argon atmosphere with a partial pressure of oxygen 0.4 mPa at a total pressure of 4.10^{-1} Pa.

The SEM top-view images of the catalyst layers are shown in Fig. 3.13 [10]. Concerning the a-C substrate, the CeO_x layer exhibits the fine grainy surface structure for all investigated thicknesses. As the amount of deposited cerium oxide is increasing, the grains reach bigger size, as well; however, the main features remain unchanged. In contrast, as one can see in Fig. 3.13, the surface morphology and the structure of the CN_x100% substrate vary significantly. The 5 nm thick catalyst layer shows the fractal-like character of growth and with the further deposition of CeO_x, the columnar structure appears and subsequently, the 30 nm thick cerium oxide grains merge, the caps atop increase and the formed surface reminds a cauliflower structure.

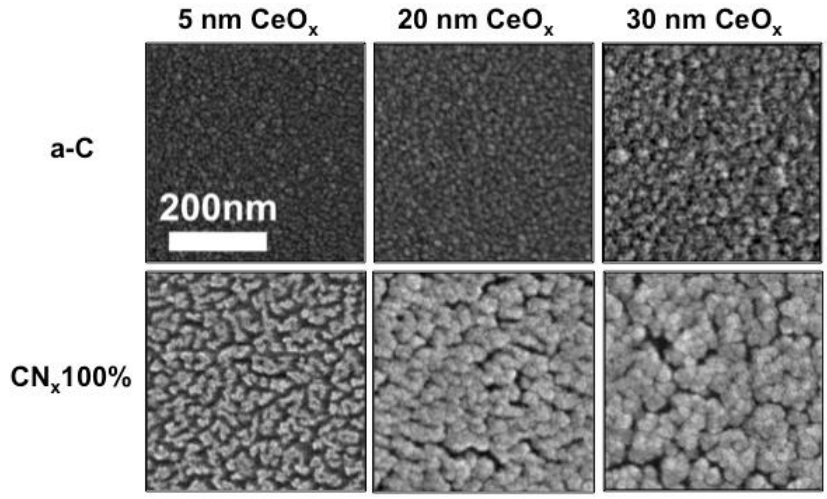

Fig. 3.13 SEM top-view micrographs of the morphology evolution for CeO_x layers deposited on the a-C and CN_x100% thin films supported by silicon as a function of nominal CeO_x thickness, taken from [10].
Deposition rate of cerium oxide 0.4 $nm.min^{-1}$, oxygen partial pressure 0.4 mPa in Ar working atmosphere, total pressure kept at 4.10^{-1} Pa.

The corresponding TEM cross-section micrographs presented in Fig 3.14 display the side view of the porous catalytic layers. In accordance with the SEM images, the surface of the CeO_x/a-C samples exhibits minor changes. The catalyst layer is continuous and slightly rough regardless of the cerium oxide thicknesses. The surface roughness follows the morphology of a-C interlayer finely modified by oxygen plasma etching. Although the transformation of the amorphous carbon surface is negligible, changes in the thickness of non-etched carbon layer are measurable and the values are recorded in Table 3.2. For instance, the thickness of the a-C film decreases after the magnetron sputtering process of 5 nm thick CeO_x layer from initial 170 nm (the thickness of the as-prepared a-C film) to 154 nm. Moreover, the porous structure (composed of the CeO_x layer with modified part of the carbon substrate) is 13 nm high in comparison with the 5 nm nominal thickness of deposited CeO_x. It suggests similar carbon film removal and modification during the magnetron sputtering of catalytic layer as in case of the C-foil substrate. The further deposition process has no influence on the a-C layer anymore (the thickness of the non-etched a-C film is 164 and 162 nm for CeO_x (20 nm)/a-C and CeO_x (30 nm)/a-C, respectively). It is in accordance with the presented model in Fig. 3.12 (see also [17]), where at an early stage of growth, the carbon substrate is not protected by cerium oxide particles against the oxygen plasma treatment and therefore, the a-C film disappears relatively fast. Thereafter, with outgoing

deposition of cerium oxide, the CeO_x particles play a role of shielding mask and the nonhomogeneous etching of carbon occurs. Afterwards, the CeO_x layer becomes more compact and the a-C film is sufficiently covered against further transformations.

On the other side, the samples prepared by using the CN_x100% film exhibit increasing porosity with increasing amount of deposited CeO_x layer. Fig. 3.14 presents the hilly-like structure created by sputtering of 5 nm thick CeO_x layer on the CN_x100% film supported by silicon. The thickness of non-etched carbon film was measured as 137 nm with corresponding 45 nm thick porous structure composed by cerium oxide and modified nitrogenated carbon. Whilst in case of the a-C film, the catalyst layer is continuous, and therefore the further etching of carbon is impossible, the hilly-like structure offers uncovered places for oxygen plasma treatment. The deeper holes formation due to the subsequent carbon fading results in a columnar structure displayed in Fig. 3.14 for the CeO_x (20 nm)/CN_x100% sample with a total thickness of 130 nm (Table 3.2). As a consequence of the additional magnetron sputtering process and thus, the additional plasma treatment, the CN_x100% film is etched to the silicon support (CeO_x (30 nm)/CN_x100%). With increasing amount of cerium oxide, caps on top the carbon surface raise and the mushroom-like structure is formed. The faster disappearing of the CN_x100% film exposed to the oxygen plasma etching during the CeO_x magnetron sputtering is in accordance with the above presented results (Section 3.1.1.2 Carbonaceous Substrates after Oxygen Plasma Etching), wherein the pure a-C and CN_x100% films were treated solely in oxygen plasma. Furthermore, it is consistent with our previous work [10], as well as with the others published elsewhere [28, 29].

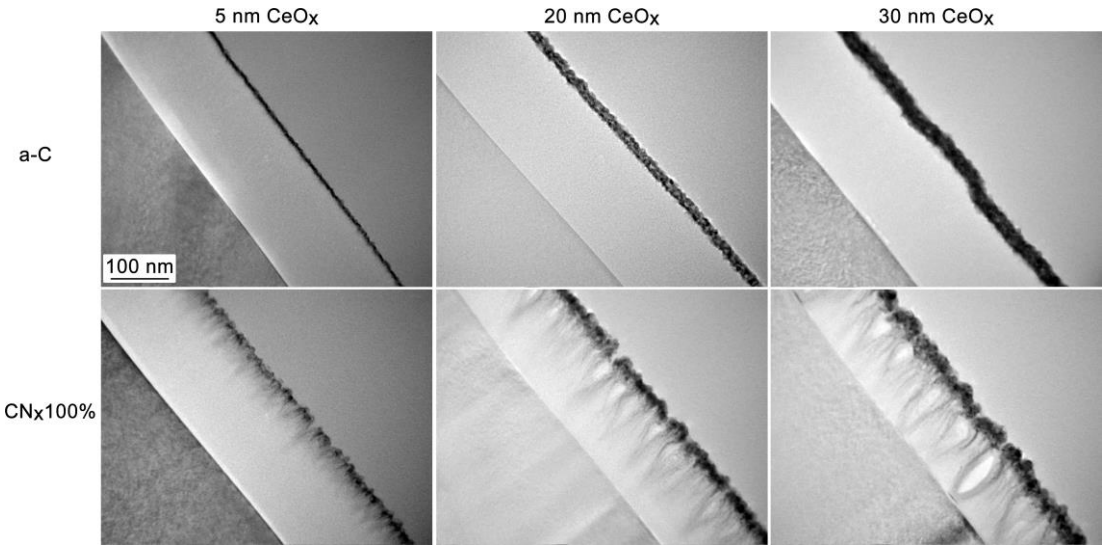

Fig. 3.14 TEM cross-section micrographs of the CeO_x layers on the a-C and CN_x100% thin films supported by silicon (left bottom corner).
Deposition rate of cerium oxide 0.4 nm.min^{-1}, oxygen partial pressure 0.4 mPa in Ar working atmosphere, total pressure kept at 4.10-^{1} Pa.

Nominal thickness of CeO_x layer [nm]		0	5	20	30
a-C film	Thickness of non-etched carbon [nm]	170	154	164	162
	Thickness of porous structure [nm]	0	13	26	39
CN_x100% film	Thickness of non-etched carbon [nm]	190	137	35	0
	Thickness of porous structure [nm]	0	45	130	151

Table 3.2 Thicknesses of the non-etched a-C and CN_x100% film and the porous structure before and after the magnetron sputtering of 5, 20 and 30 nm thick CeO_x layer.
Thickness measurement done on the base of the TEM side-views presented in Fig. 3.2, 3.4 and 3.14.

- *Films with different nitrogen content*

With purpose to investigate the etching rate variation with different nitrogen content in the CN_x layers, a series of nitrogenated carbon films was prepared via magnetron sputtering process on the silicon support in working atmosphere composed of argon and nitrogen. The gas flow composition contained 5, 25, 50, 75 and 100% of nitrogen in N_2/Ar mixture at a total gas pressure of 0.8 Pa. In order to keep this study consistent with previously presented work [10], we try to prepare 200 nm thick nitrogenated carbon layers with different nitrogen content. Unfortunately, in case of CN_x substrates with low content of nitrogen, delamination of the layers has occurred. As a consequence of this bad adhesion with the silicon support, the CN_x/a-C bilayers growth was chosen. In this case 100 nm thick a-C layer was deposited directly on silicon and afterwards, the 100 nm thick CN_x films was sputtered onto. In addition, two CN_x100% films were prepared with total thicknesses of 200 nm: one as a bilayer and second as a single layer, while the higher pressure was used (4 Pa) during the sputtering. In this case the 200 nm thick a-C film with was considered as a reference sample. Subsequently, the 5 nm of CeO_x was deposited simultaneously on all the CN_x/a-C, CN_x and a-C substrates by magnetron sputtering in oxygen/argon atmosphere (estimated deposition rate 0.2 $nm.min^{-1}$, oxygen partial pressure 1 mPa, total pressure 4.10^{-1} Pa). The TEM observation was carried out on lamellas prepared by FIB.

Fig. 3.15 illustrates the changes of morphology after the catalyst deposition due to the different content of nitrogen into the working gas during the magnetron sputtering of CN_x layers. The formed structure of the a-C and CN_x5% films shows similar features of individual pillars even though distinction in the non-etched carbon thickness is appreciable. Whereas, the a-C film without any modification is 104 nm thick, the rest of CN_x5% has only 77 nm (Table 3.3). It would imply that the nitrogen doping of the carbonaceous layer results to the faster carbon fading due to the higher etching effect caused by the oxygen plasma. By adding more nitrogen in gas flow during the CN_x film deposition (25% and more), nitrogenated carbon is less resistant against the plasma treatment and the structure in form of individual noodles is created. The features are similar, only variations in the thicknesses of non-etched carbon part and the porous structure are present, as one can see from Table 3.3. With increasing amount of nitrogen in working atmosphere during the CN_x layer

preparation (giving an increase of nitrogen content in the CN_x layers as will be presented later), the thickness of non-etched carbon films is decreasing accompanied by formation of higher porous structures. Unfortunately, some break during the CeO_x magnetron sputtering on CN_x75%/a-C film has occurred, and herein displayed structure is not in accordance with our expectation. Moreover, it is remarkable to compare the samples containing CN_x100%, prepared as the CN_x100%/a-C bilayer at pressure 0.8 Pa, the bilayer at 4 Pa and as the CN_x100% single layer at 4 Pa, respectively. Concerning the bilayers, the CN_x100% film is etched to the a-C film; however, the thickness of the porous structure is significantly lower for the sample prepared at higher nitrogen pressure (cf. 102 nm for CeO_x (5 nm)/CN_x100% (0.8 Pa)/a-C and 69 nm for CeO_x (5 nm)/CN_x100% (4 Pa)/a-C). In addition, the 200 nm thick CN_x100% (4 Pa) single layer is etched to the silicon support.

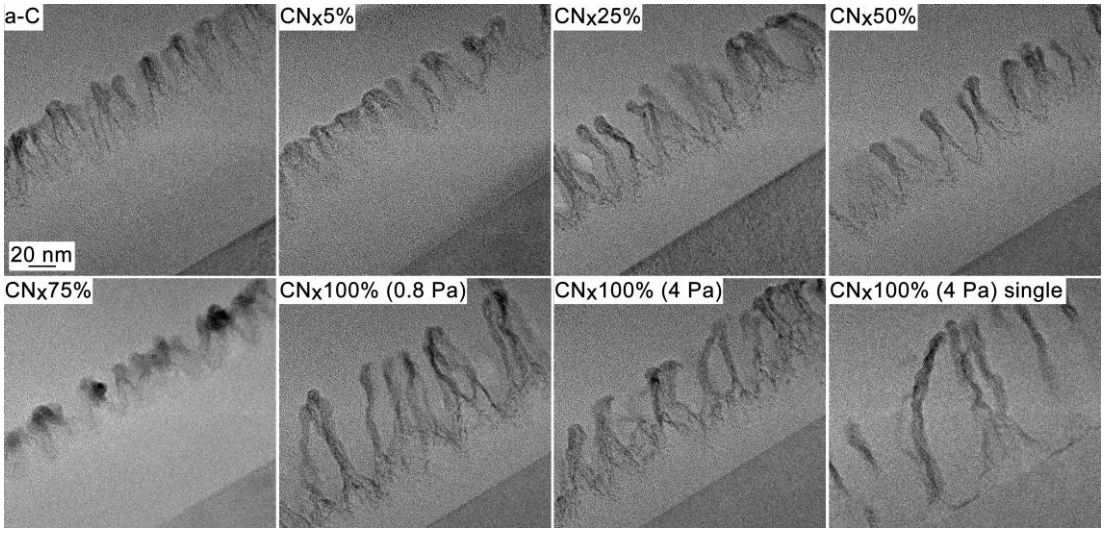

Fig. 3.15 TEM cross-section micrographs of the 5 nm thick CeO_x layers on the 200 nm thick intermediate carbonaceous films: a-C single layer, bilayer CN_x/a-C with N concentration of 5, 25, 50, 75, 100% (0.8 Pa) and 100% (4 Pa) and CN_x100% (4 Pa) single layer.

All films are supported by silicon (right bottom corner).
Deposition rate of cerium oxide 0.2 nm.min^{-1}, oxygen partial pressure 1 mPa in Ar working atmosphere, total pressure kept at 4.10^{-1} Pa.

Concentration of N_2 in gas flow [%]	0 (single, 0.8 Pa)	5	25	50	75	100 (0.8 Pa)	100 (4 Pa)	100 (single, 4 Pa)
Thickness of non-etched carbon [nm]	**104**	**77**	**44**	**60**	**82**	**40**	**38**	**0**
Thickness of porous structure [nm]	**60**	**56**	**71**	**67**	**47**	**102**	**69**	**132**

Table 3.3 Thickness of non-etched carbon and the created porous structure for different carbonaceous films after the 5 nm thick CeO_x layer deposition.
The initial thicknesses of all the as-prepared carbonaceous (bi)layers were close to 200 nm.

The above-presented results suggest that by increasing content of nitrogen in the gas flow mixture of N_2 and Ar, the resistance of CN_x films against the oxygen plasma treatment is decreasing. The higher the pressure of nitrogen during the CN_x layers sputtering is, the faster the carbon fading etching occurs due to the oxygen plasma. It results in a strong etching effect of carbonaceous layers and therefore, in considerable modifications of the created structures. Thus, it indicates that nitrogen content and its partial pressure in the deposition chamber during CN_x layer preparation by magnetron sputtering is of the major factor affecting the etching of carbon surfaces.

According to the literature, higher amount of N_2 in working gas and/or higher pressure results to a higher content of nitrogen in CN_x films [9, 11, 13, 30]. Furthermore, the subsequent deposition of CeO_x layer accompanied by oxygen plasma etching causes the carbon substrate transformation. It was mentioned that the active oxygen species interact with the CN_x surface, while the gaseous molecules of CO, CO_2 and CN or others volatile species as NO and/or NO_2 are formed and pump away [12, 18-20, 23, 28, 29, 31]. These questions, as well as composition of the magnetron sputtered CN_x films and changes by oxygen plasma and/or deposition of catalytic layers on cerium oxide base will be discussed later (Section 3.1.2 Composition of Catalyst Support).

3.1.1.3.3 Influence of Cerium Oxide Deposition Rate and Composition of Working Atmosphere

As noted in the previous section, not only the type and/or composition of carbonaceous substrates have an impact on the final morphology of catalytic structures forming during magnetron sputter deposition of cerium oxide. The created porous structures may be affected by amount of deposited cerium oxide, as mentioned above, as well as by others preparation conditions, e.g. the deposition rate of CeO_x and the partial pressure of oxygen play an important role during the cerium oxide magnetron sputtering.

The comparison of Figs. 3.14 and 3.15 taken for single layers of CN_x100% after the 5 nm thick catalyst deposition, indicates that the structure has been considerably modified. Fig. 3.14 (the bottom left image) displays the hilly-like character of growth by using a deposition rate of 0.4 $nm.min^{-1}$ and an oxygen partial pressure of 0.4 mPa, whilst Fig. 3.15 (the bottom right image) presents the individual noodles created after the cerium oxide deposition with a rate of 0.2 $nm.min^{-1}$ and a partial pressure of 1 mPa. Therefore, the further investigation was carried out on the samples with the 20 nm thick CeO_x layer on the CN_x100% film supported by silicon with variation in the deposition rate and partial pressure of oxygen.

- *Cerium oxide deposition rate*

In order to study the impact on the morphology and structure due to the variation of cerium oxide deposition rate, the CeO_x layer was sputtered on the 200 nm thick CN_x100% film with different deposition rates of 0.2, 0.4 and 0.8 $nm.min^{-1}$. The partial pressure of oxygen was kept at the same value of 0.4 mPa for the all samples. The results obtained by means of TEM on lamellas prepared by FIB are presented in Fig. 3.16. In case of low deposition rate (0.2 $nm.min^{-1}$), the etching process of carbon prevails over the surface covering by cerium oxide particles. The individual noodles with the average thickness of 20 nm and a large gap between them were observed. As one can see, the continuous CeO_x layer coats this areas on the silicon support surface (dark line). With deposition rate of 0.4 $nm.min^{-1}$, the system is in an equilibrium state between the carbon removal and the cerium oxide adsorption, since the columnar structure is formed. Further increase of the

deposition rate results in the predominant effect of the surface covering and suppressing the carbon etching process consequently leading to the creation of less porous structures. The similar mechanism was observed for the a-C layers in our previous studies, as well [10, 17].

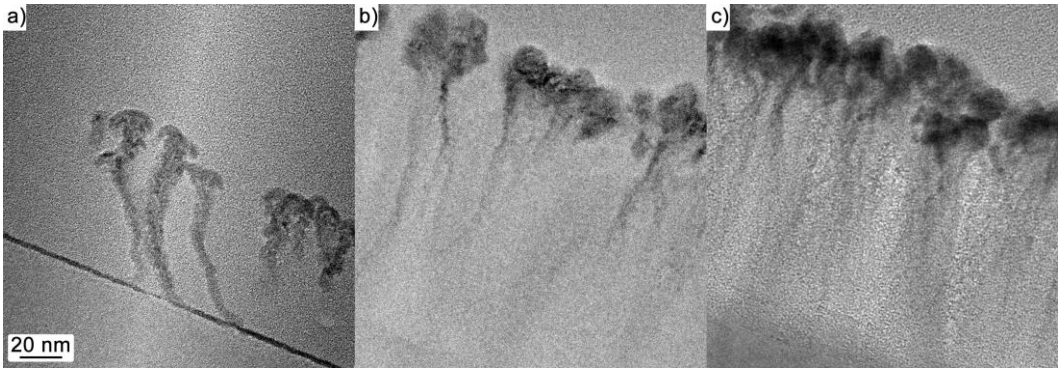

Fig. 3.16 TEM side-view images of the 20 nm thick CeO_x layer on the CN_x100% intermediate film prepared with the cerium oxide deposition rate of 0.2 a), 0.4 b) and 0.8 nm.min^{-1} c), respectively.
Oxygen partial pressure 0.4 mPa in Ar working atmosphere, total pressure kept at 4.10^{-1} Pa.

- *Composition of working atmosphere*

The analogous investigation was also carried out for the dependence on the oxygen partial pressure. A series of 20 nm thick CeO_x layers was sputtered on the CN_x100% film with the deposition rate of 0.2 nm.min^{-1} at the total pressure of working gas kept at 4.10^{-1} Pa, whilst the oxygen partial pressure differed. The changes in composition of working atmosphere lead to the catalyst structure modification, as it is displayed in Fig 3.17. The deposition of cerium oxide in the pure argon atmosphere results to the formation of a catalyst layer with the columnar structure. The porous layer morphology varies depending on the oxygen residual pressure in the deposition chamber, as a consequence the carbon etching caused by oxygen plasma.

At relatively small concentration of oxygen (0.4 mPa), carbon is extensively modified, and very thin noodle nanostructures are created. Moreover, in many places the carbonaceous layer was completely reacted off up to the silicon support that was consequently covered by cerium oxide during the deposition. It points out a very fast carbon vanishing. For higher oxygen pressure (1 mPa and 4 mPa) the

noodle structures of higher density are growing higher. In addition, further significant increase of oxygen pressure (10 mPa) does not cause more major carbon film transformation, but results to a relatively compact catalyst layer. Based on these results, we can assume that the porous structure formation mechanism leans towards the partial pressure of oxygen in the working gas. In the pure argon atmosphere, cerium oxide particles reach the carbon substrate and the surface is prevented from etching. The increasing amount of oxygen in the working gas causes faster carbon etching. However, for even higher partial oxygen pressure, etching effect is reduced. The same investigation for the a-C layers was carried out in our previous work, coming to a similar conclusion [17].

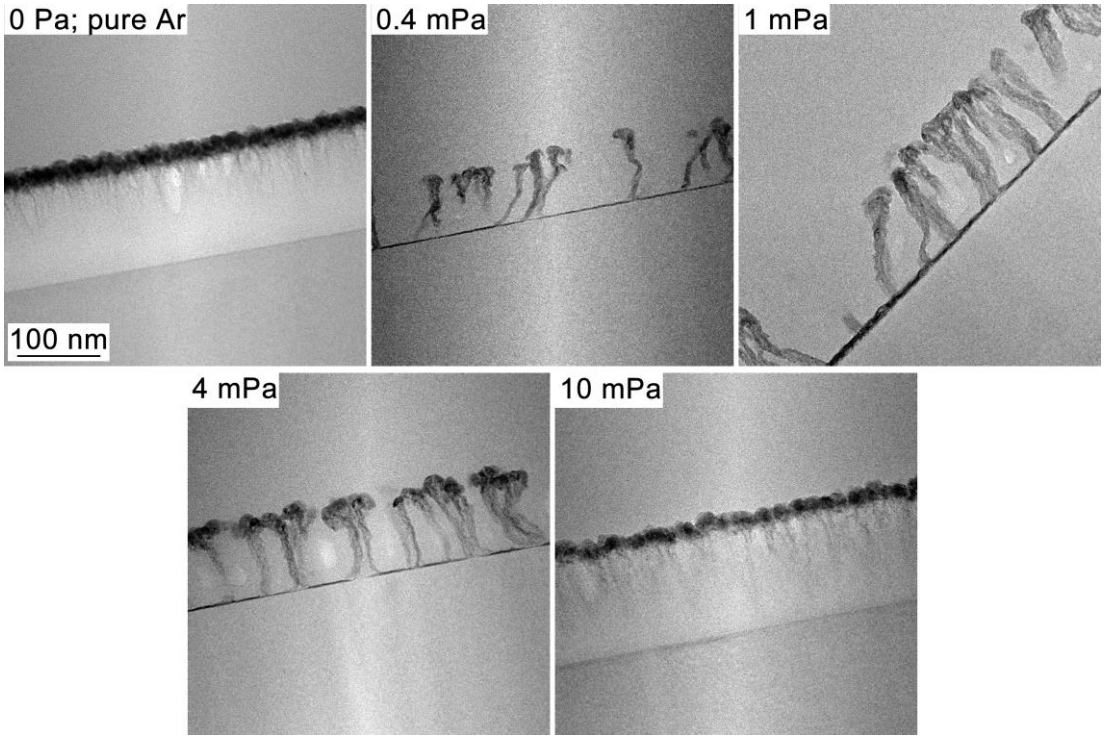

Fig. 3.17 TEM side-view images of the 20 nm thick CeO_x layer prepared on the intermediate CN_x100% film supported by silicon (right bottom corner) with variation in oxygen partial pressure.
Initial thickness of the as prepared CN_x100% film 200 nm, deposition rate of cerium oxide 0.2 nm.min^{-1} at the total pressure of working gas 4.10^{-1} Pa.

As it was previously mentioned several times, all herein presented results point out the simultaneous effects of carbon etching by oxygen plasma and the cerium oxide deposition during the magnetron sputtering on the carbonaceous substrates. Therefore, the analysis of the elaboration conditions influence on the

catalyst layer morphology indicates that important preparation parameters are the deposition rate of cerium oxide and the partial pressure of oxygen inside the preparation chamber. In general, we can conclude that the faster deposition rate leads to the less porous structure. On the other side, for the oxygen partial pressure the link is more complex, small amount of oxygen in the working gas results to a significant oxygen plasma etching of carbon, however, high partial oxygen pressure and pure argon atmosphere lead to the continuous layer formation. Moreover, the resistance of prepared carbonaceous films against plasma treatment decreases with increasing partial pressure of nitrogen during the CN_x film sputter deposition. This finding could help us to further anode catalyst improvement and fuel cell activity enhancement. Finally, we can conclude that the growth model described above (Fig. 3.12) is valid also in case of cerium oxide layer growth on nitrogenated carbon (CN_x) films as shown above.

3.1.2 Composition of Catalyst Support

Besides information about morphological changes of carbon substrates and a porous structure formation, an examination of the catalyst support composition widens our knowledge of the systems to a considerable extent. In order to study the element composition, absolute or relative concentrations and chemical states of individual elements, different spectroscopic techniques were used. Their combination allowed us to assemble the complex information about the catalyst. Energy Dispersive X-ray Spectroscopy (EDX) and Electron Energy Loss Spectroscopy (EELS), as techniques complementary to Transmission Electron Microscopy (TEM), were applied on the samples in form of thin lamellas prepared by FIB, while Photoelectron X-ray Photoelectron Spectroscopy (XPS) data were obtained on the samples as prepared, i.e. thin layers supported by silicon wafers of 10 x 10 mm^2 in size.

3.1.2.1 EDX Characterization

In order to verify the above-presented model describing the porous structure formation of CeO_x on carbonaceous substrates, EDX measurements were carried out.

To confirm our hypothesis that the catalyst hilly-like structure is formed by modified carbon substrate, and that these shapes are just copied by cerium oxide, EDX spectra were taken from the cross-sectional sample of CeO_x (20 nm)/C-foil. The observed area corresponds to the ADF STEM image shown in Fig. 3.10 c). The superposed maps of C, Ce and Pt elements displayed in Fig. 3.18 point at the presence of carbon (green) inside the created structure, whilst Ce (red) decorates the surface and occurs mostly in the caps atop. We have to note that platinum (blue) was used as a protective layer during the lamella preparation by FIB.

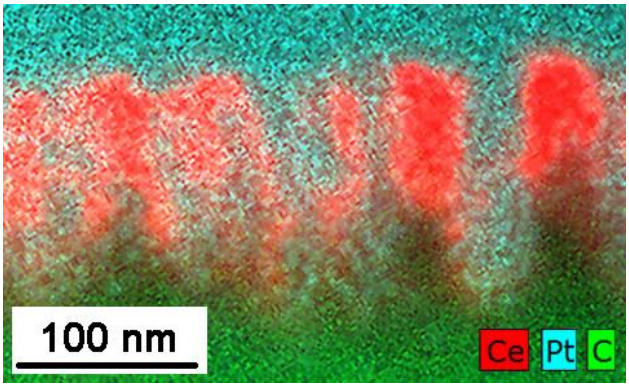

Fig. 3.18 EDX element map of the CeO_x (20 nm)/C-foil sample displaying carbon (green), cerium (red) and platinum (blue).

The composite element map obtained by means of EDX has proven our hypothesis about carbon modification during the CeO_x magnetron sputtering. It allows us to confirm the growth model proposed in Fig. 3.12 [17]. The main ideas were described in detail above, and thus, herein we present only the graphical sketch of the growth process (Fig. 3.19).

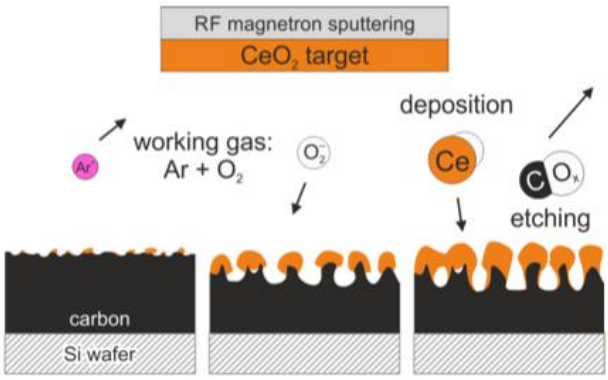

Fig. 3.19 Graphical sketch of the growth model for CeO_x deposition on an intermediate carbon substrate supported by the silicon wafer during magnetron sputtering process (taken from [17]).

3.1.2.2 EELS Characterization

To better understand faster removal of nitrogenated carbon by oxygen plasma treatment, further investigation of these substrates is needed. EELS is a suitable method for detection of elements with low atomic number, and thus, it fits very well for carbon and nitrogen. Moreover, cerium can be detected, as well.

In order to comprehend the role of nitrogen incorporated in the carbonaceous film, a study of the influence of the nitrogen concentration variation in working gas during CN_x film preparation on the carbonaceous films composition was performed by means of EELS. The samples were prepared in form of thin lamellas from the 200 nm thick a-C and CN_x layers supported by silicon wafer. The EELS spectra were acquired with a 1 nm probe, an energy dispersion of 0.2 eV per channel and a Gatan Imaging Filter aperture of 2 mm.

Fig. 3.20 presents EELS spectra taken from the samples with different N_2/Ar composition in gas flow during the carbonaceous films sputtering. The spectra were positioned at the zero-loss peak and/or the nitrogen peak at 400 eV for the a-C and CN_x layer, respectively. The K-edges of carbon (near edge fine structure) and nitrogen are displayed. At the first sight, it can be seen that the spectrum of the a-C film (green one) differs from the others, acquired on the layers containing nitrogen.

At the C K-edges, the usual two peaks corresponding to π and σ anti-bonding states are displayed [31]. The K-edge does not contain any sharp peak that is characteristic for amorphous nature of the films [30, 32]. In addition, the peaks are

relatively broad, which may indicate that not only sp^3 and sp^2 bonding states but also sp^1 ones are present. Thus, we are studying the relative π^*/σ^* ratio, since to set the absolute sp^2/sp^3 ratio is not possible [32, 33].

For the a-C film, a peak approximately at 285.0 eV was detected, whereas, a shift towards higher electron energy losses (about 2 eV) was observed for all the CN_x layers. Moreover, with increasing amount of nitrogen in working gas, an intensity of the π^* region is increasing against the intensity of the σ^* region, (see Table 3.4). However, the relative π^*/σ^* ratio does not change much for the layers CN_x75%, CN_x100% (0.8 Pa) and CN_x100% (4 Pa).

In the same way as for C K-edges, the displayed nitrogen peaks were marked as π^* and σ^* region. Their interpretation is rather complicated due to the multiple bonding possibilities of nitrogen [32].

Any nitrogen peak cannot be seen for the a-C film, in accordance with our expectation, as amorphous carbon films were prepared in pure argon. Otherwise, the N K-edges intensity rises as the nitrogen concentration reaches higher values.

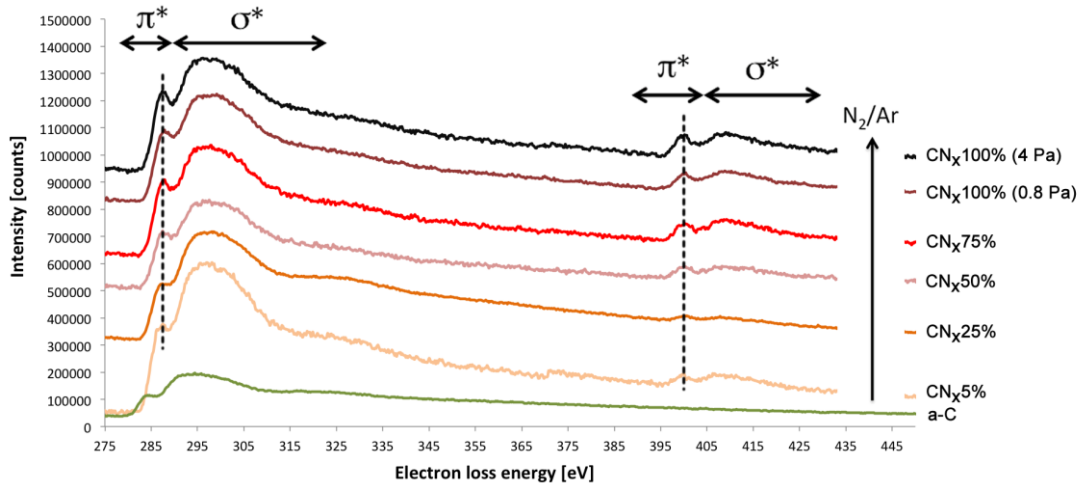

Fig. 3.20 EELS core-loss spectra of carbonaceous films with different N_2/Ar gas flow composition. The K-edges for carbon and nitrogen are displayed.

Based on the analysis of EELS spectra, we calculated the relative N/C composition of the CN_x films and the values are set in Table 3.4. The amount of nitrogen in the nitrogenated carbon films increases with the nitrogen concentration in the gas flow up to the saturation concentration around 33% is achieved

(N/Ar ≈ 75%). The further increase of nitrogen content in the working gas during the magnetron sputtering does not lead to the higher N concentration in the CN_x layer.

N/Ar	0% a-C	5% CN_x5%	25% CN_x25%	50% CN_x50%	75% CN_x75%	100% (0.8 Pa) CN_x100%	100% (4 Pa) CN_x100%
π*/σ* ratio	0.37	0.57	0.40	0.70	0.91	0.95	0.83
N/C ratio	0%	11%	13%	27%	33%	30%	33%

Table 3.4 Intensity ratio of π* to σ* region and relative nitrogen concentration in CN_x layers set from EELS spectra vs. nitrogen amount in N/Ar gas flow mixture.

The above presented results show that the nitrogen content in gas flow during the carbonaceous films sputtering results to the structural and chemical changes of CN_x layers. In comparison with the a-C film, where C K-edge at approximately 285.0 eV is close to the signature of graphite [30], the carbon peak for the CN_x layers is shifted above 2 eV towards the higher energy losses. This shift is generally attributed to the charge transfer from nitrogen to carbon due to the higher electronegativity of nitrogen [30, 33, 34]. The peak at 286.5 eV, assigned by Mubumbila *et al.* [30] as a feature of pyridine, is increasing with increasing amount of nitrogen in the layer, while the resonance at 288.0 eV has never been unambiguously puzzled out. In the σ* region, the peaks at 293.0 and 297.5 eV are close to the signature of aromatic structures of graphite and pyridine [30].

The increasing intensity of carbon π* peak vs. the nitrogen content suggests that the number of π bonds for C and N, related to the sp^2 and/or sp^1 orbitals, is increasing to the detriment of σ* bonds, related to the sp^3 orbital. However, the exact nature of the π* states cannot be determined; i.e. we cannot distinguish between CC sp^2 and CN sp^2. On the other side, we can assume that with decreasing of σ* region intensity, the CC sp^3 bonds are substituted by CN sp^2 and/or CN sp^1 ones. It is in agreement with several studies, which have proven that with increasing amount of nitrogen, the C=N bonds are increasing, as well [14, 30, 32-35].

The deconvolution of N K-edge is not unambiguous from EELS data due to the different bonding environment of the threefold coordinated nitrogen. Based on the theoretical work of Alvarez *et al.* [36], we proposed herein same contributions, which may be considered: a) at 398.4 eV, N sp^3 bonded to C sp^3 in "open" structure (due to the threefold coordinated N and fourfold coordinated C), b) at 399.0 eV N sp^3 bonded to C sp^3 in "closed" stressed structure (C-N-C), c) at 399.2 eV N sp^2 in pyridine d) at 399.4 eV N sp^1 in nitrile structures and e) at 401.5 eV substitution N sp^2 in graphite-like C sp^2 (aromatic) structures. However, further spectroscopic techniques are needed for precise analysis.

In accordance with the literature, the nitrogen concentration in the CN_x layers rises as a consequence of increasing N/Ar proportion in gas flow during the magnetron sputtering [30, 32, 33]. The saturation was achieved approximately at 33% for 75% of nitrogen in the working gas, and the further increasing in the N/Ar ratio causes no change. It results in the composition of $C_{0.66}N_{0.33}$.

In order to study structural and chemical changes after the cerium oxide layer sputtering on top of the CN_x100% film supported by silicon, EELS mapping was performed on the CeO_x (20 nm)/CN_x100% sample. The EELS spectra were acquired with a 1.5 nm step, a 1 nm probe, an energy dispersion of 0.3 eV per channel and a Gatan Imaging Filter aperture of 2 mm. We were interested in the relative composition of carbon, nitrogen and oxygen, thus the spectra windows were selected with regard to the C, N and O signal detection.

Fig. 3.21 presents the STEM image of the CeO_x (20 nm)/CN_x100% sample with marked area of interest, where the EELS spectra were acquired at each point. In addition, the relative composition of N, C, O and Ce is displayed in "temperature" colour scale, where the brighter tone means higher proportional representation of element. By comparison of the element maps, we can deduce that carbon is almost present everywhere except the upper part of the sample, where the cerium oxide caps were detected. It can be due to several factors: carbon is the main component of the CN_x layer, the protective layer can also contain carbon, either, or due to the carbon contamination. On the other hand, the nitrogen and oxygen spectra are complementary; the major nitrogen content is inside the unmodified CN_x layer, while almost no oxygen has been found there. However, in boundary areas of the CN_x layer, where carbon is modified due to the processes occurring during the

magnetron sputtering of CeO_x, the nitrogen concentration is decreasing. In contrast, in these areas, the deposited CeO_x layer leads to increasing occurrence of oxygen. The surface structure is fully occupied by oxygen originating from cerium oxide.

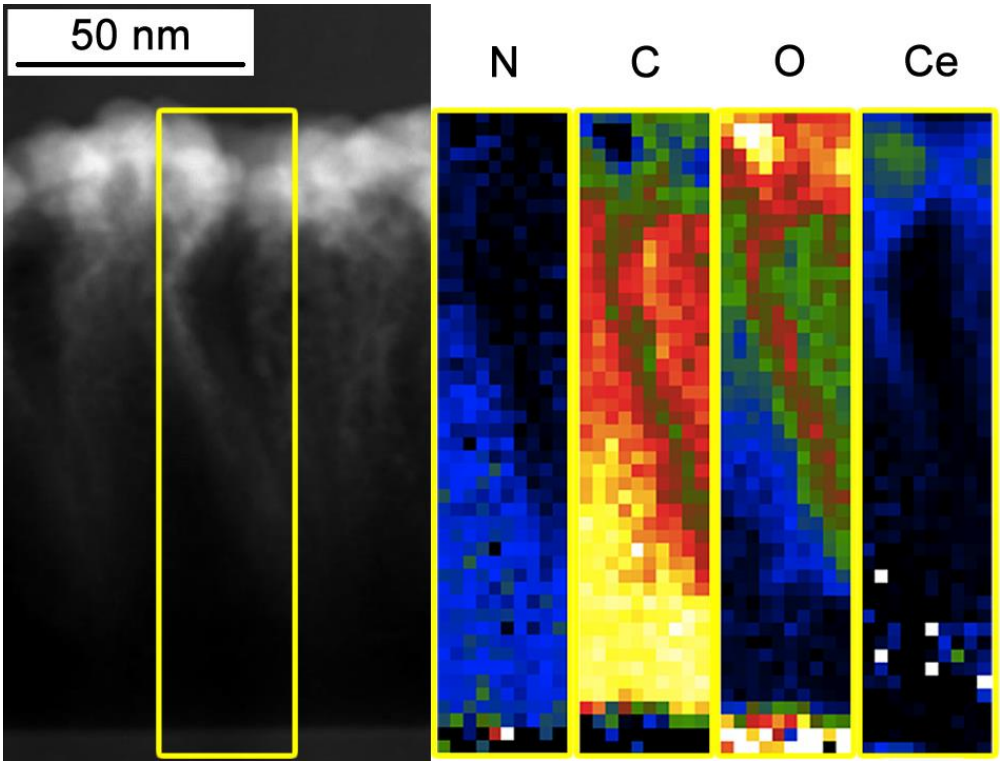

Fig. 3.21 STEM image with marked area of interest on the CeO_x (20 nm)/CN_x100% lamella and corresponding element maps of relative composition for nitrogen, carbon, oxygen and cerium.

With aim to confirm the idea of nitrogen content decreasing in the border areas of modified CN_x layer, the values of relative ratio for N, C, O and Ce are displayed in Table 3.5. The relative concentration of N is not exceeded 30% inside the non-modified carbonaceous layer. It is in good agreement with the above-presented results (Table 3.4), where the as-prepared CN_x100% layer was investigated. With increasing signal of Ce, the amount of nitrogen is decreasing significantly (from 33% to 0%), while the concentration of carbon evinces only slight changes (from 65% to 50%). It suggests a faster removal of nitrogen compared to carbon caused by the magnetron sputtering of catalyst layer. Oxygen and cerium amount has similar tendency due to the cerium oxide layer. In addition, the silicon oxide layer on the silicon support surface is well visible.

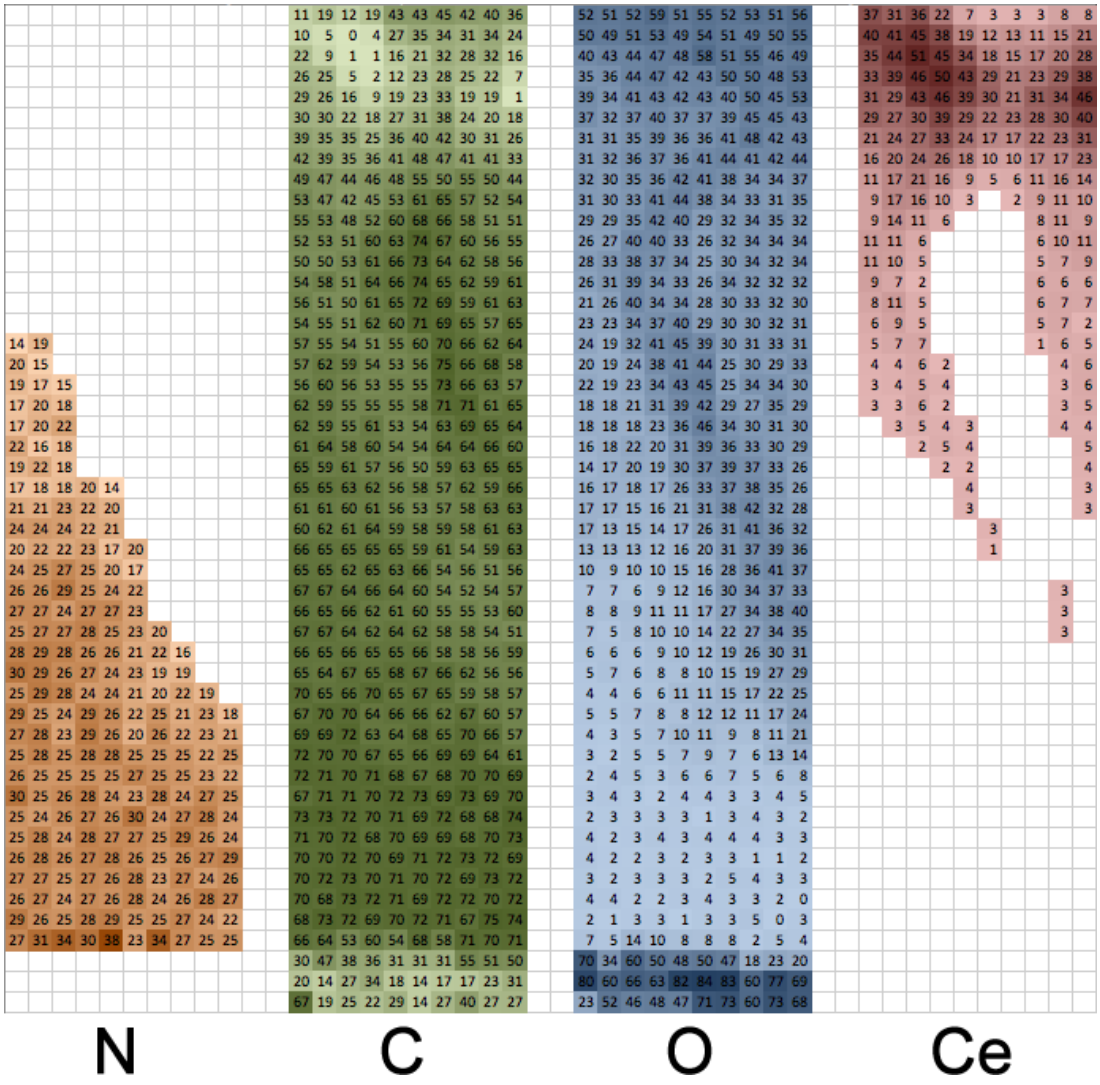

Table 3.5 Relative concentration of N, C, O and Ce for the 20 nm thick CeO_x layer on a-C substrate.

The magnetron sputtering of cerium oxide includes two main processes as was proposed above: the CeO_x layer deposition and the simultaneous oxygen plasma etching of the carbonaceous substrate. The second mentioned process leads to the volatile species formation, which causes the substrate modification, among others changes in the film composition, i.e. the changes in the relative concentration of carbon and nitrogen. In the literature, it was shown that the gaseous molecules contain carbon (CO, CO_2 [18-20, 23]) and/or nitrogen (NO, NO_2, C_2N_2 [12]). Moreover, the removal of nitrogen after oxygen plasma treatment was also confirmed by the decrease of N peak obtained by means of XPS as will be shown later [28].

Furthermore, the nitrogen amount has an influence on the bonding character in material; i.e. by adding more nitrogen in the layer the fraction of the sp^2 bonding states is increasing [9, 14, 30, 32, 33, 35]. Moreover, as indicated by the previous studies [22, 25, 26], the etching rate of sp^2 hybridized carbon is much higher than for the sp^3 carbon bonds. Thus, we suggest that the different character of bonds caused by added nitrogen may leads to the faster removal. Unfortunately, due to the broad peak of nitrogen in the EELS spectra, we cannot support this hypothesis. To confirm or exclude it, further spectroscopic analyses are needed.

3.1.2.3 XPS Characterization

In order to study the bonding character in the CN_x layer, the XPS measurement has been carried out. The investigation has been done on the as-prepared layers with the different amount of nitrogen in the processing gas and subsequently, after the oxygen plasma treatment and after the deposition of 5 and 20 nm thick CeO_x layer, as well.

The C 1s and N 1s XPS spectra were acquired for the a-C and CN_x layers with various concentrations of nitrogen (5, 25, 50, 75, and 100%) in working gas. Similarly to the EELS data analysis, relative nitrogen concentration in the CN_x layers was determined. Calculations of the concentration were done as a ratio of N 1s peak area to the sum of C 1s and N 1s peak areas taking into account atomic sensibility factors of 0.25 for carbon and of 0.42 for nitrogen, respectively. The calculated values are displayed by a chart in Fig. 3.22. As one can clearly see, almost no nitrogen was detected for the a-C layer. On the other side, even a very small amount of nitrogen in gas flow (5%) during the CN_x sputter deposition leads to relatively high concentration of nitrogen in the deposited layer (17%). Further increase of nitrogen amount in gas flow results in the increase of N concentration in prepared films. However, we have to note that changes are not as distinctive as in case of the step between a-C and CN_x5%. Nitrogen concentration is achieving saturation values close to 30%. It is in good accordance with the results obtained by EELS (see Table 3.4). For better illustration, the values of nitrogen concentration in the CN_x layers obtained by EELS data analysis are plotted in the same chart in Fig. 3.22.

Unfortunately, some break during the magnetron sputtering of CN_x75% film has occurred, and herein displayed results are not in accordance with our expectation.

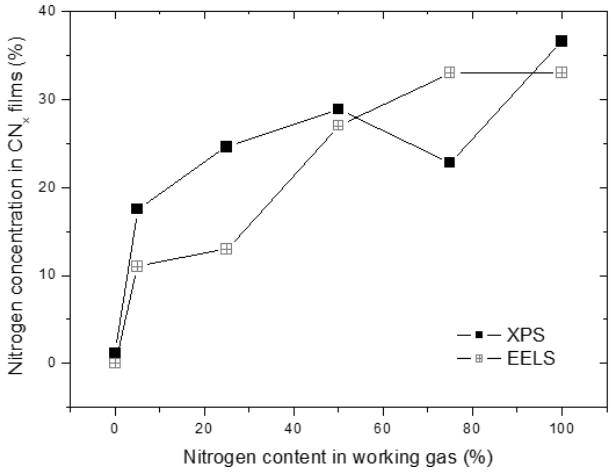

Fig. 3.22 Relative nitrogen concentration in the a-C and CN_x layers as a function of nitrogen content in working gas during magnetron sputtering based on XPS and EELS analyses.

The XPS C 1s and N 1s spectra for the a-C and CN_x layers with various concentrations of nitrogen (5, 25, 50, 75, and 100%) are shown in Fig. 3.23. The spectra were deconvoluted to several peaks.

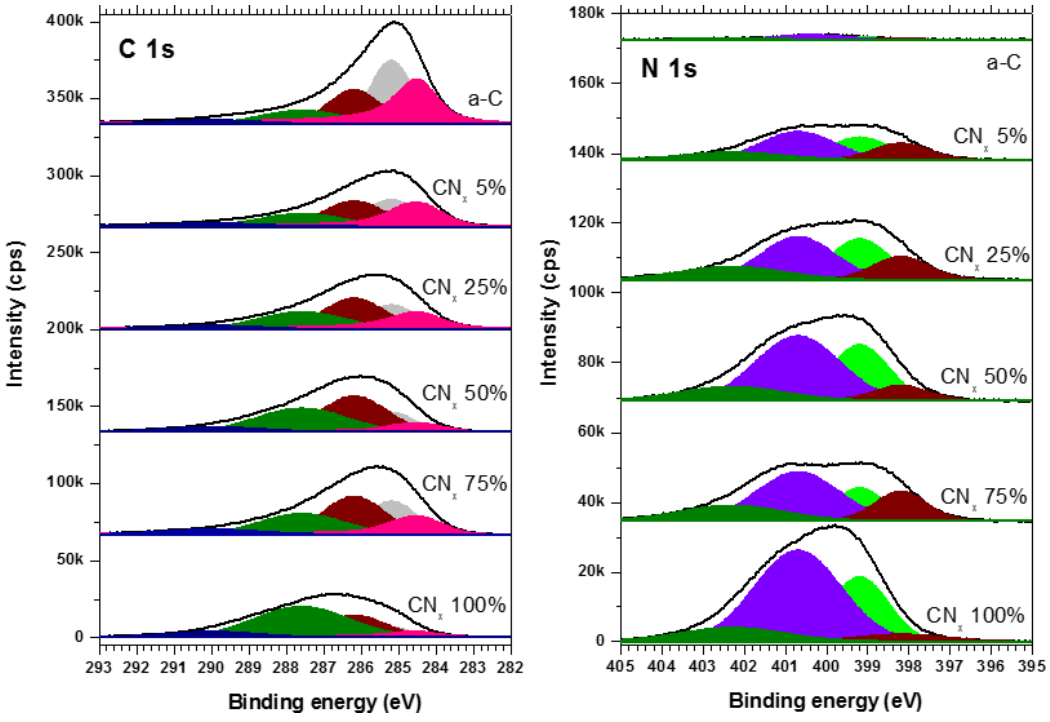

Fig. 3.23 XPS C 1s and N 1 spectra for the a-C and CN_x layers with various nitrogen concentrations.

The broad C 1s spectra were fitted by 5 individual peaks (denored as C1 - C5). Very similar decomposition can be found in paper published by Angleraud *et al.* [37], which was chosen as the main resource material for further interpretation. Some other authors have opted rather for 4 peaks convolution [28, 32, 38].

The C1 peak at 284.3 eV is generally attributed to the CC sp^2 coordinated bonds in graphite-like amorphous carbon [28, 37], however, Chowdhury *et al.* [38] have labelled the peak position as due to adventitious carbon originated from the atmospheric contamination. Rodil *et al.* [32] assigned the peak at 285.2 eV to the CC sp^3 states due to presence of low nitrogen concentration and/or hydrocarbon. We cannot exclude any hydrogen presence in the as-prepared a-C or CN_x layers; however, we attributed the peak at 285.2 eV solely to the CC sp^3 bonds in diamond-like amorphous carbon in accordance with results in [37]. The C3 and C4 peaks at the higher binding energies of 286.2 eV and 287.6 eV, respectively, are related to the nitrogen incorporation [28, 32, 37-40]. As suggested by several authors [28, 37-40], these C3 and C4 peaks are assigned to the CN sp^2 and CN sp^3 bonds, respectively. Nevertheless, their position in binding energy scale varies for different publications. In case of nitrogen atom bonded to three fold carbon the peak was observed at 285.9 eV [40], 286 eV [38] 286.1 eV [28] and 286.6 eV [37, 39]. For nitrogen atom bonded to therahedral carbon, the peak shifts from 287.3 eV [39] through 287.7 eV [28, 40] to 287.8 eV [37]. In addition, Rodil *et al.* [32] has included heteroaromatics (C3 peak) and aliphatic CN (C4 peak) to these positions. At least, the C5 peak lying at 288.9 eV can be assigned to C-O bonds [32].

Similar deconvolution has been done for N 1s peak, where the board spectrum is composed of four Gaussian peaks, labeled N1 - N4, while their interpretation is much more complicated. The N1 peak at 398.2 eV can be attributed to the CN sp^3 bonds [37, 40-42]. Despite of CN sp^3 contribution the peak at 398.2 eV is labeled as nitrile [43]. The N2 peak located at 399.2 eV can be associated with pyridine-like environment [44]. However, Chowdhury *et al.* [38] has proposed to assign the peak with CN sp bonds, Barber *et al*. [45] with nitrile. Analogically, the N3 peak at 400.6 eV fits with CN sp^2 in graphite-like environment [32, 37-42]. Nevertheless, same researchers propose the interpretation as pyrrole [32], imine [43] or as different bonds between nitrogen itself, e.g. NN sp^2 [38, 46]. The bonds with oxygen cause the appearance of the N4 peak, at 402.5 eV [32, 37, 40, 42]. However,

not even interpretation of this peak is unambiguous, because physisorption of N_2 molecules leads to the peak at similar position [32]. As one can expect, the proportion of individual peaks in C 1s and N 1s spectra is changing with the different composition of nitrogen in the layer. For the as-prepared a-C layer, we obtained relatively high proportion of carbon bonded as sp^2 and sp^3, as well as the peak, which we assigned with CN sp^2 fraction. On the other side, representation of C4 and C5 peaks, assigned to CN sp^3 bonds and bonds with oxygen, respectively, is lower. With increasing amount of nitrogen in the CN_x layer, the contribution of C-C bonds is decreasing, and contrarily, the contribution of C-N bonds is rising up. More accurate, the increase is significant for the peak attributed to the CN sp^2 bonds, wherein the C4 peak, interpreted as CN sp^3, is considerable for higher values of nitrogen in gas flow during the CN_x layers magnetron sputtering.

Complementary behavior should be found in the N 1s spectra. In case of the as-prepared a-C layer, the spectra intensity is very low due to the small amount of nitrogen in the layer. Fitting the very noisy spectrum, we can distinguish the N3 peak at 400.6 eV, mostly marked as a signature of CN sp^2 bonds, as well as the N2 peak at 399.2 eV is visible. Due to the bonds with oxygen or rather physisorbed N_2, we can also observed the peak N4 of very low intensity. We cannot obtained any N1 state assigned with CN sp^3 bonds. With increasing nitrogen amount, the increase of N3 and N2 peaks is detected, which points at higher number of CN sp^2 as well as pyridine bonds. In addition, the N1 peak has appeared even for low concentration of nitrogen in the chamber (5%), but its intensity has decreasing tendency with increasing amount of nitrogen in working atmosphere during the layer deposition. The N4 peak remains almost static for all CN_x layers.

To conclude, we confirmed the decrease of C1 and C2 contribution and increase of C3 and C4 peaks with increasing amount of nitrogen in the layer. It is in accordance with literature [37] and thus, we can infer that carbon in C-C bonds is substituted by nitrogen. With lower amount of nitrogen in the CN_x layer, the graphite-like bonds are primary replaced and therefore, we obtained significant higher percentage of C3 peak, labeled to CN sp^2 bonds. As the concentration of nitrogen is rising up, carbon in sp^3 configuration is replaced by nitrogen as well, which leads to the higher intensity of C4 peak. The complementary changes should be observed in the XPS N 1s spectra, however their interpretation is not unambiguous. We can confirm only increase in the N3 peak, which represents

CN sp^2 bonds in graphite-like environment, and in N2 peak assigned to pyridine-like environment. Also, the N1 peak was detected which can be assigned with CN sp^3 bond. Nevertheless, we cannot exclude for example the contribution of nitrile or pyridine-like bonds at the perimeter of vacancy defects [44] for interpretation of the N1 state, or pyrrole or others aromatic and/or aliphatic compounds in case of N3 peak [32].

In order to study the influence of oxygen plasma treatment on the carbonaceous layers, the 200 nm thick a-C and CN_x100% layers were exposed to the oxygen plasma, and the XPS spectra were acquired afterwards. Fig. 3.24 represents the C 1s spectra for the a-C and CN_x100% layers, before and after the oxygen plasma exposure.

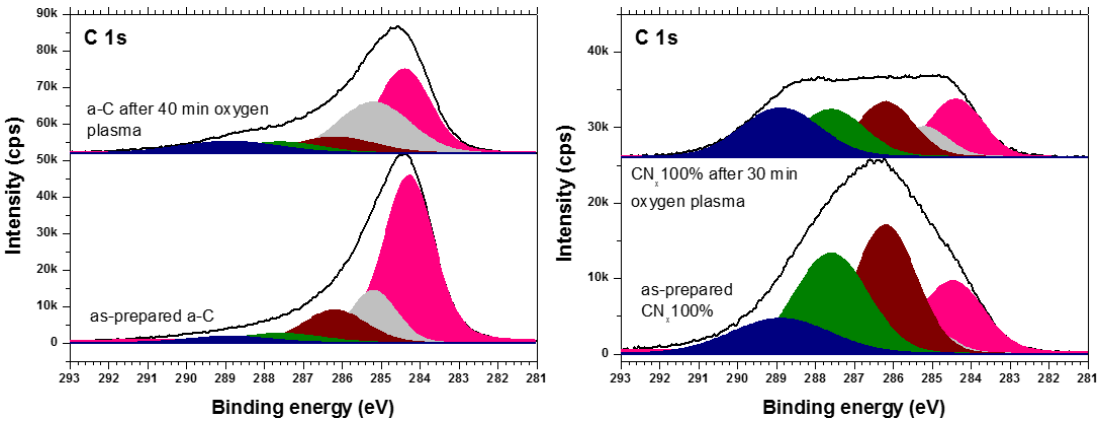

Fig. 3.24 XPS C 1s spectrum of a-C and CN_x100% layer, respectively, before and after oxygen plasma exposure.

As one can see, in case of a-C thin film, the decrease in the intensity of C1 peak, assigned to the CC sp^2 bonds, was observed. It confirms the previous published results [22, 25, 26], where it was shown that the etching rate of sp^2 hybridized carbon is higher than for the sp^3 hybridized carbon. The oxygen species contained in oxygen plasma react with carbon surface atoms resulted in volatile carbonaceous oxides [18-20, 23]. This reaction leads to the selective oxygen plasma etching occurred on the carbon substrate [20, 24]. In addition, the peak representing C-O bonds has risen slightly up after the oxygen plasma exposure.

In the same way, we can analyse the XPS C 1s spectra for the CN_x100% thin film after the O_2 plasma treatment. The most significant change is visible for the C3

peak. Detected decrease of the C3 peak is caused by the removal of CN sp^2 bonds due to the oxygen plasma influence. This suggests that oxygen plasma works effectively as an etchant of N bonded in graphite-like environment [28, 47]. The same behaviour is observed for the N4 peak assigned to nitrogen atom bonded to thetrahedral carbon and/or aliphatic CN bonds. The C1 peak, attributed to the CC sp^2 bonds, remains unchanged under oxygen plasma treatment. The behaviour of peaks C1 and C3 related to the CC sp^2 and CN sp^2 bonds, as well as observed decrease of the C4 peak intensity, can indicate that nitrogen is removed faster from the CN_x layer than carbon. Therefore, we assume that the preferential etching of nitrogen itself due to the impact of oxygen species causes the decomposition of CN bonding. Moreover, the considerably increase of C-O bonds was obtained due to surface oxidation.

In the context of the cerium oxide magnetron sputtering resemblance to the oxygen plasma treatment as regards the influence on carbonaceous substrate, XPS C 1s and N 1s spectra were acquired before and after the CeO_x layer deposition. Similarly, as for the oxygen plasma, the properties of the a-C and CN_x100% thin films were compared. The thicknesses of deposited CeO_x layers was estimated as 5 nm and 20 nm on flat silicon substrate.

Concerning the a-C film (see Fig. 3.25), the C 1s spectrum measured after the CeO_x layer deposition exhibits almost no shape changes, only overall intensity of the spectrum is decreased due to the attenuation of XPS signal caused by deposited cerium oxide on the carbon surface. Contrary to the a-C layer, the CN_x100% film has shown significant changes in the composition after the CeO_x layer deposition as one see in Fig. 3.26. The impact of cerium oxide deposition to the CN_x100% film is much stronger in comparison to the oxygen plasma influence (cf. Fig. 3.24). The peaks C3 and C4 are substantially suppressed which indicates disappearing of nitrogen incorporated in the CN_x films. It is in good agreement with the results obtained by means of EELS spectroscopy, where the concentration of nitrogen was found to be decreasing in the area of catalyst-substrate interface. This fact is possible to verify in the XPS N 1s spectra acquired on the CN_x100% film and presented in Fig. 3.26. Significant decrease in the N 1s intensity, which cannot be explain by the attenuation of XPS signal due to the deposition of cerium oxide, indicates that the sputter deposition process of cerium oxide primary decomposes C-N bonds. Herein, we can see the similarity between the oxygen plasma etching of carbonaceous

substrates and the magnetron sputtering of CeO_x layer. It confirms our previous hypothesis that during the deposition process, the oxygen plasma is formed in the chamber due to the residual oxygen in the working atmosphere [10, 17, 27] leading to the distinct morphological and compositional changes of the carbonaceous substrate. Presented results clearly show that easier breaking C-N bonds due to the influence of the oxygen plasma and/or the CeO_x deposition accompanied by faster removal of nitrogen incorporated in the CN_x films is of the reason of the higher etching rate of the nitrogenated carbon films than in case of the amorphous carbon films.

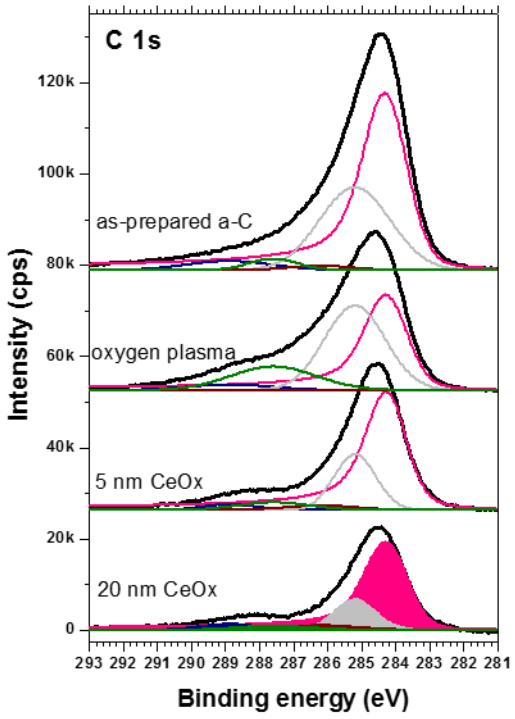

Fig. 3.25 XPS C 1s spectra of the a-C before and after the deposition of 5 nm and 20 nm thick CeO_x films. For comparison spectrum measured after oxygen plasma treatment is added.

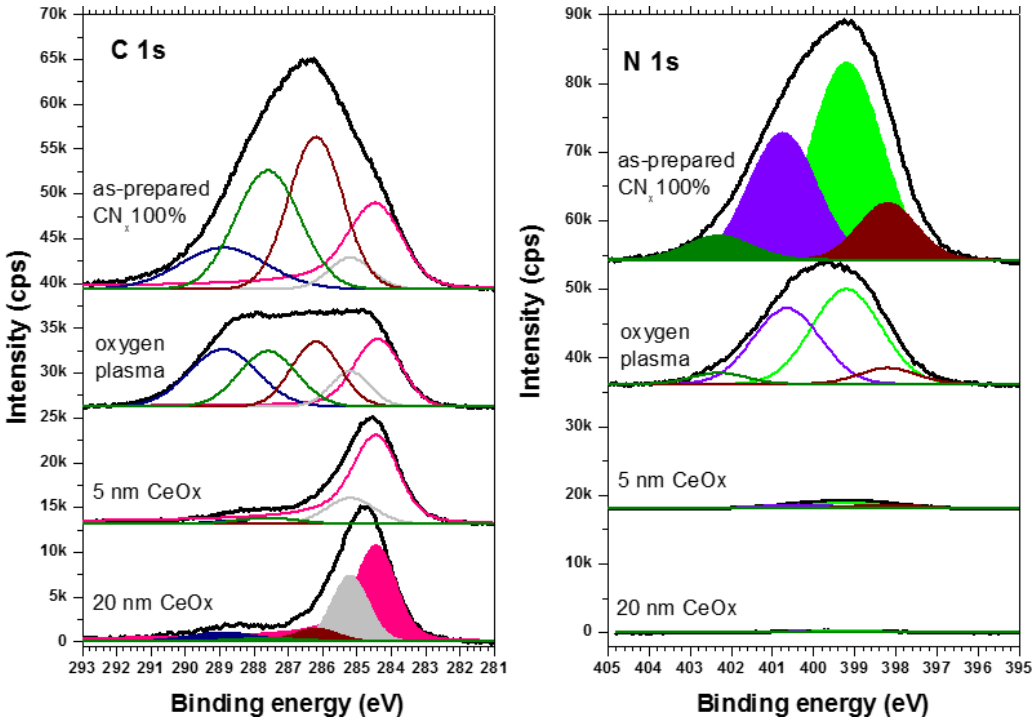

Fig. 3.26 XPS C 1s and N 1s spectra of the CN_x100% film before and after the deposition of 5 nm and 20 nm thick CeO_x films. For comparison spectra measured after oxygen plasma treatment are added.

From the above-presented results obtained by spectroscopic techniques, we can conclude that with increasing nitrogen concentration in working gas during deposition of carbonaceous films, the concentration of nitrogen incorporated in the CN_x layers is increasing, the sp^2 bonds are increasing as well. We suppose that the CC sp^3 bonds are replaced by nitrogen and it leads to the C-N bonding formation or to the CC sp^2 transformation. However, the C-N bonds seem to be less resistive to the oxygen plasma etching, as the bonds with nitrogen are decomposed first of all. Similar, but more pronounced effect was observed after the cerium oxide deposition process.

In addition, the spectroscopic data confirmed the growth model of cerium oxide on carbonaceous layer; i.e. the carbon film surface is significantly modified due to the oxygen plasma treatment and simultaneous cerium oxide deposition. It results in the porous structure of catalyst.

3.2 Cerium Oxide Layers

For improvement of the catalytic CeO_x/carbon-based system and its further applications, detailed knowledge and therefore a complete characterization of the catalyst is very important. As outlined previously (Section 3.1 Catalyst Support Characterization), the role of the catalyst substrate was demonstrated, and moreover, we pointed to the structural and compositional modification of the carbonaceous catalyst support after the cerium oxide deposition via magnetron sputtering. In following sections, our attention is focused on the cerium oxide layer itself, specifically on crystallography of cerium oxide layers regarding the thickness of the sputtered film, deposition conditions and the type of catalyst substrate. Furthermore, cerium oxidation states transformation related to the cerium oxide-carbon interface is studied.

3.2.1 Crystallography Study

In order to confirm our hypothesis based on the SEM and conventional TEM observations that sputter deposited cerium oxide layers are composed of small crystalline grains, the HRTEM studies were performed on several samples. As it was mentioned before, the growth of cerium oxide on different carbon substrates give rise to various surface morphologies, which can be linked to changes in crystallography of deposited layers. Thus, our attention is focused on the nanocrystallite type, its composition, shape and size with regard to the catalyst support and the deposition conditions.

According to the literature, in Section 1.4 Platinum Doped Cerium Oxide Catalyst Layers, we described stable and semi-stable crystallographic forms of cerium oxide, as CeO_2 and Ce_2O_3, which crystalize in a cubic (fluorite) and trigonal crystal structures [48-50]. In pursuit to these crystals observationy, HRTEM images were acquired, analysed and compared with data obtained from the crystallographic database [51]. The JEMS software was used for zone axis simulation and comparison with the experimental data [52].

The HRTEM images confirm our assumption and point to the nanocrystalline character of all the sputtered cerium oxide layers. The deposited cerium oxide films

are composed of crystallites with variable size up to several nanometers. Regardless the others factors as the substrate material, the amount of deposited cerium oxide and deposition conditions, the major part of recorded crystals corresponds with distances and angles to ceria, namely CeO_2 [101], CeO_2 [112] and CeO_2 [111]. Fig. 3.27 illustrates examples of cerium oxide crystals exhibiting the zone axis [101], [112] and [111], respectively.

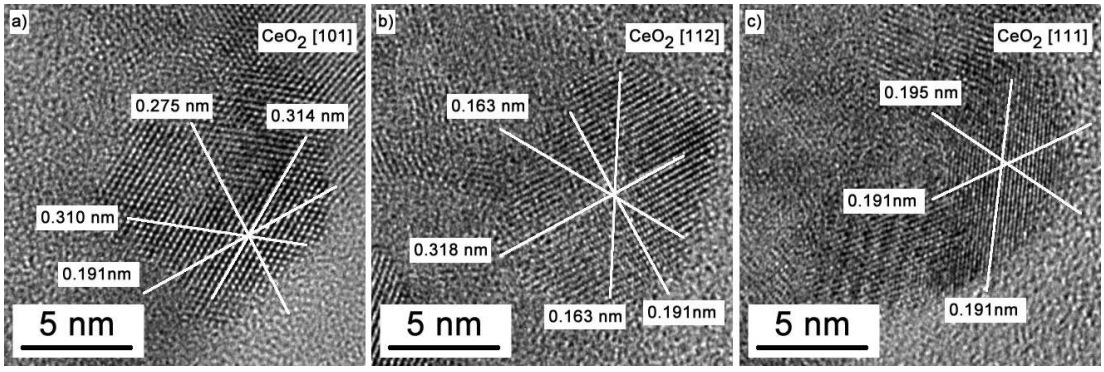

Fig. 3.27 HRTEM micrographs of nanocrystals observed in cerium oxide layers identified as CeO_2 [101] a), CeO_2 [112] b) and CeO_2 [111] c).

Mainly, in case of the cerium oxide layer supported by the silicon substrate, recorded zone axes of observed crystals did not correspond to cerium oxide in form of CeO_2 but rather to its reduced form Ce_7O_{12}, which crystalize in a rhombohedral crystal structure [50]. Fig. 3.28 presents the HRTEM micrograph of a crystal with distances and angles corresponding to the Ce_7O_{12} [203] zone axis.

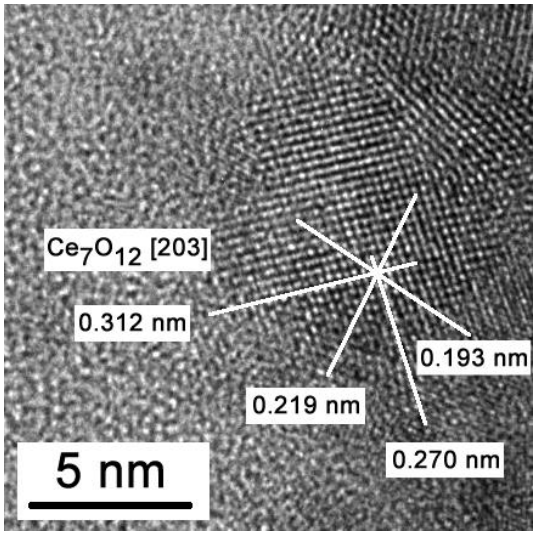

Fig. 3.28 HRTEM micrograph of a cerium oxide nanocrystal identified as Ce_7O_{12} [203].

Unfortunately, to distinguish between CeO_2 and Ce_7O_{12} crystals is not always unambiguous, since some zone axes of CeO_2 and Ce_7O_{12} exhibit similar values of distances and angles. As an example, we can mention here CeO_2 [101] ≈ Ce_7O_{12} [310], CeO_2 [112] ≈ Ce_7O_{12} [540] or CeO_2 [111] ≈ Ce_7O_{12} [001] zone axes. In case of ambiguity, we are inclined to favour CeO_2 crystal rather than Ce_7O_{12}.

Some researchers have shown that Ce_7O_{12} structures on Si can be achieved via CeO_2 layer annealing due to the periodic ordering of oxygen vacancies compared to the fluorite structure of CeO_2 [50, 53]. Accordingly, the oxygen vacancies can be formed as a result of oxygen discharge by ion bombardment during the magnetron sputtering of a cerium oxide layer. Therefore, such cerium oxide reduction can lead to the Ce_7O_{12} structures formation.

We note that we did not observe any Ce_2O_3 crystal, and thus, we suggest, if Ce_2O_3 is present it should be amorphous.

For catalyst layers grown on carbonaceous substrates, we identified several crystallites as CeO_2 or Ce_7O_{12}. However, in some cases recorded values of distances and angles were not in agreement with any zone axis of the cerium oxide structures. It suggests the formation of other compounds, such as cerium carbides. In accordance with this assumption, many crystals corresponding to the CeC_2 structure were identified. To our best knowledge, very few publications exist concerning cerium carbides, mainly outdated and dealing with metallurgy [54, 55]. They

describe magnetic properties of CeC_2 and its tetragonal crystal structure [54-56]. Nevertheless, any picture showing CeC_2 crystals in reciprocal or real space have not been displayed yet. Herein, we present several of them with the orientation along [100], [110], [001] and [102] zone axes (Fig. 3.29).

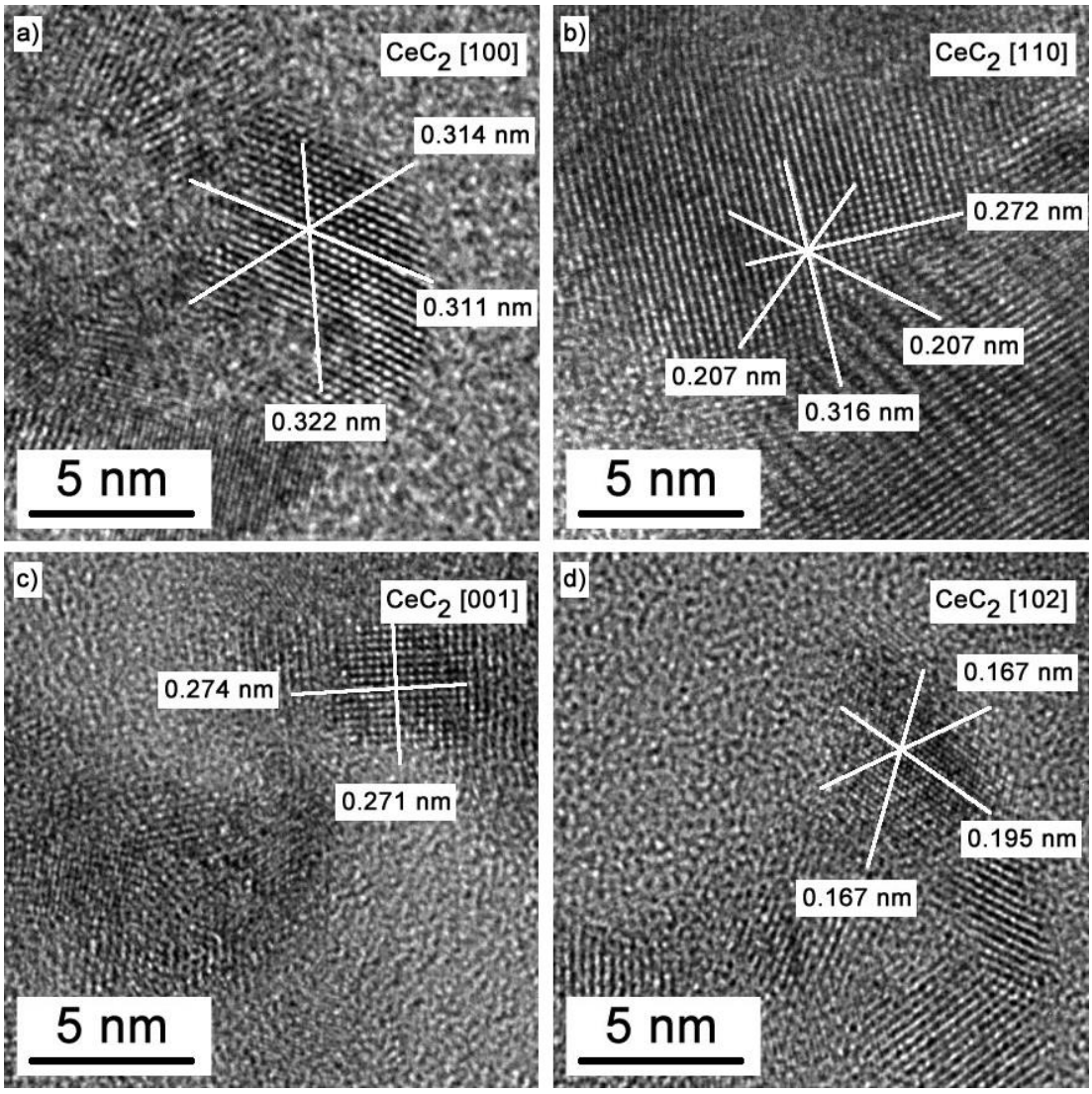

Fig. 3.29 HRTEM micrographs of cerium carbide nanocrystals observed in a cerium oxide layer deposited on a carbonaceous substrate identified as CeC_2 [100] a), CeC_2 [110] b) CeC_2 [001] and CeC_2 [102] d).

Similarly to CeO_2 and Ce_7O_{12} presenting similar distances and angles for several zone axes, the presence of CeC_2 is not always unambiguous. CeC_2 [111] can be interchangeable with CeO_2 [101] or Ce_7O_{12} [310]. In these cases, we marked the crystal as CeO_2.

For CeO_2 crystals with size below 5 nm the precise measurement of distances was difficult, not even due to the crystal size, but also due to the lattice anomaly. We have observed that the interplanar distances are bigger than for bulk cerium oxide and moreover, the distance is increasing with the decreasing size of the crystal. The anomaly lattice expansion could be explained by the higher amount of the oxygen vacancies due to the smaller size of the crystal. It is caused by the electrostatic repulsion of cerium cations, which are not shielded by oxygen anions [57-60].

3.2.1.1 Localization of Crystals

Concerning the catalyst layer morphology, the deposition of cerium oxide via magnetron sputtering results in various forms/structures dependent on the substrate material, the deposition conditions and the thickness of the deposited layer. Since the morphology is closely related with crystallography, the same factors have an influence on the localization of crystals, their sizes and shapes.

The most critical parameter for the crystals localization is the catalyst support. During the magnetron sputtering, the inert argon ions reach the ceria target and sputter cerium oxide molecules and/or decompose cerium oxide to the fragments - cerium and oxygen ions. Moreover, due to the residual pressure into the chamber and/or oxygen added to the working gas, the oxygen plasma is formed and the highly energetic oxygen ions can react with the substrate [10, 17, 27]. In case of carbonaceous and nitrated substrates, the volatile CO_x and NO_x species are removed [18-20]. Thus, the large amount of different particles coming to the reaction offers even larger quantity of products.

The CeO_2 crystals are observed for any type of catalyst support and they are well dispersed in the deposited layers. This is in contrast to the CeC_2 crystals, which are identified solely for samples prepared on carbonaceous substrates. Moreover, they are recorded only close to the catalyst-substrate interface. As an example of the crystals localization, in Fig. 3.30, we present the side-view micrograph of CeO_x (20 nm)/CN_x100% with marked positions and crystals identification. As one can see, the CeC_2 crystals occur very close to the carbonaceous substrate and their

size is much smaller than in case of the CeO_2 crystals. On the contrary, the CeO_2 crystallites have been found inside and atop of the deposited layer, as well.

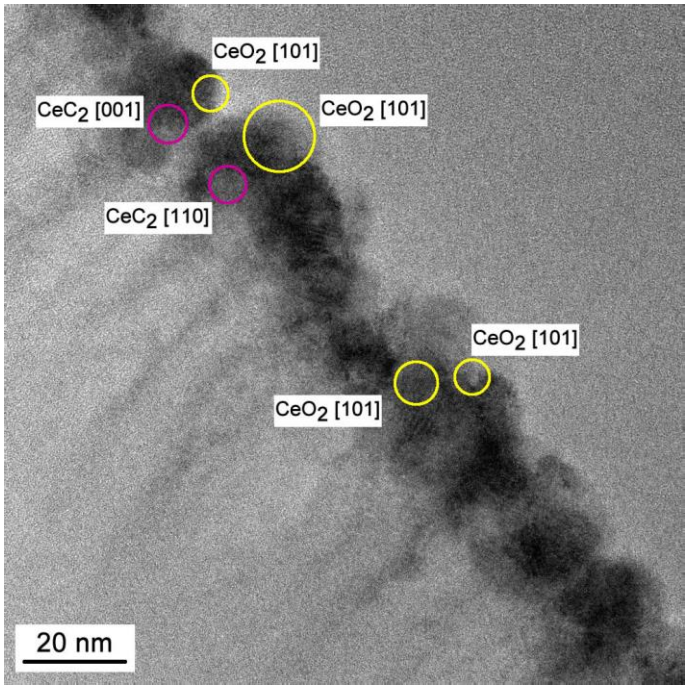

Fig. 3.30 TEM cross-sectional image of CeO_x (20 nm)/CN_x100% with marked position and identification of the crystals.

The reason for the CeC_2 crystals formation could be a replacement of oxygen atoms by carbon ones during the magnetron sputtering process. Vidhya *et al.* [61] have studied enthalpy and Gibbs energy of such a reaction leading to the cerium dicarbides. Mixture of solid CeO_2 (s) and graphite can be described per the following equation:

$$CeO_2(s) + 4C(s) = CeC_2(s) + 2CO, \quad (3.1)$$

with a final product of the solid CeC_2 compounds. The by-product is volatile CO, similarly as in case of carbon etching, detected by the mass spectroscopy [18-20].

In comparison, any cerium carbides have not been observed on the Si substrate. Nevertheless, in this case the reduced form of cerium oxide, Ce_7O_{12}, is not rare. As it was mentioned before, the oxygen vacancies ordering can be achieved by annealing of stoichiometric ceria in UHV conditions [62] or under high hydrogen pressure [63, 64] and/or, as in our case, we relate it to the ion bombardment during

the magnetron sputter process. By all treatments, oxygen can be removed from CeO_2 with following structure reordering. Besides, we did not note any preferential localization of Ce_7O_{12} crystals.

Additionally, cerium and/or cerium oxide reacts with the native silicon oxide layer on the top of silicon resulting in silicates and silicides formations [64, 65]. We did not acquire any of them in the crystalline form, and thus, we suppose they are amorphous. However, their existence was confirmed by EELS [64] and XPS analysis [65].

3.2.1.2 Size of Crystals

Although all acquired crystals present nanometric dimensions, specifically, not bigger than 20 nm, their size is not uniform. Similarly to the localization of crystals, the deposition conditions during the magnetron sputtering and the substrate selection have an influence on the crystals size. Two generally applicable rules can be formulated: *the thicker layer, the bigger crystals* and/or *the less porous layer, the bigger crystals*. The third important factor is the crystal localization: *the crystals closer to the substrate are smaller*. Let's see them in detail.

As it was shown in Section 3.1.1.3.1 Influence of Cerium Oxide Deposition Time, the morphological changes are occurring with increasing deposition time, i.e. with higher amount of deposited cerium oxide. Such morphological changes have an influence on crystals size, as well. The initial growth of the cerium oxide layer is connected with fine grainy structure, while individual nuclei of very small size are formed. Fig. 3.31 a) presents the HRTEM image of cross-sectional sample with 1 nm thick CeO_x layer on top of C-foil. It is well seen that the cerium oxide layer is non-continuous and it forms very small crystallites with size up to 3 nm. With further increase in the cerium oxide layer thickness, nanoparticles reach bigger size on top of caps as sufficient amount of cerium oxide was deposited. This effect is displayed in Fig. 3.31 b), where the 5 nm thick CeO_x layer on C-foil leans to the formation of crystals with size around 5-6 nm. The structure of the C-foil substrate is well visible in both images (left bottom corners). We have to note that platinum protective layer

was used in this case, therefore the cerium oxide layer – surface interface is overlapped with platinum grains (right top corner).

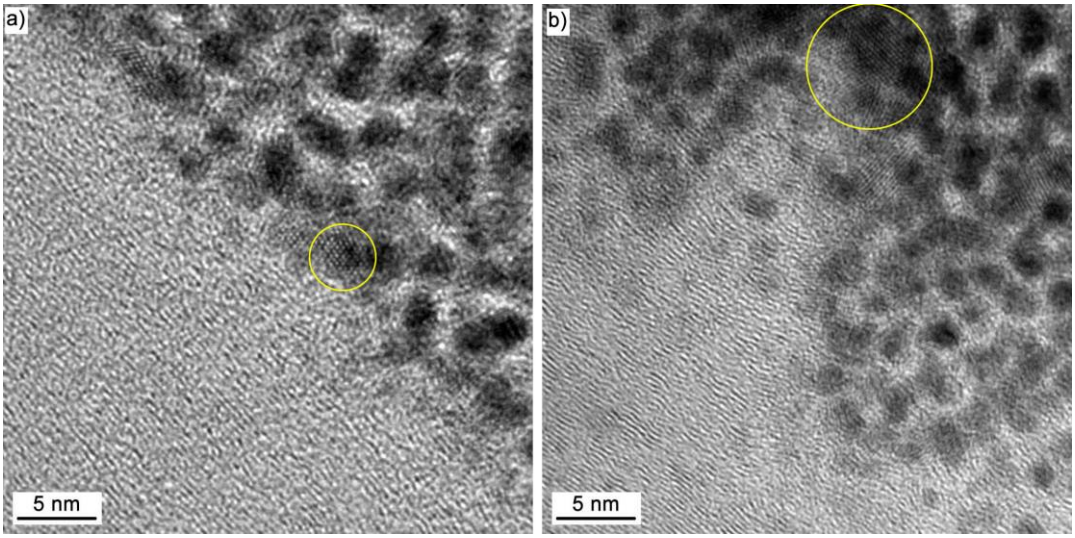

Fig. 3.31 HRTEM images of the CeO_x (1 nm)/C-foil a) and CeO_x (5 nm)/C-foil sample b). The thicker layer gives rise to the bigger size of crystals.

The further top cap growing is connected with even higher amount of deposited material. As one can see in Fig. 3.32, where the magnified images of Fig. 3.14 are displayed, the sputter deposition of more material leads to the bigger crystals formation. We compare here the CeO_x layers with nominal thicknesses of 20 nm and 30 nm deposited on the CN_x100% substrate; the size of cerium oxide crystals is rising up with the increasing thickness of the sputtered layer. This effect occurs due to the mechanism of grains sintering to the bigger crystallites, which are more energetic favourable.

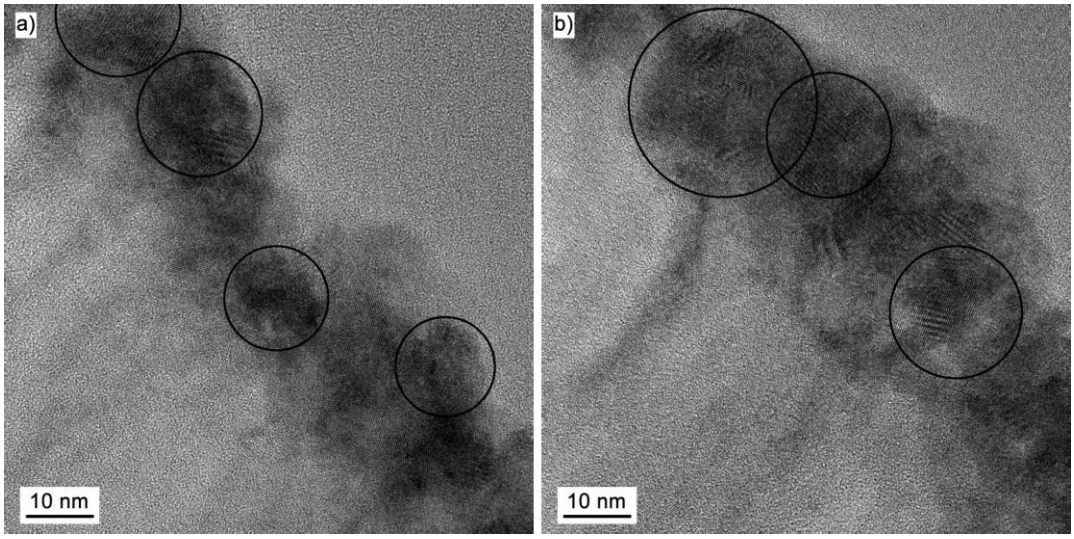

Fig. 3.32 Magnified images of the CeO_x (20 nm)/CN_x100% a) and CeO_x (30 nm)/CN_x100% sample b). The thicker layer gives rise to the bigger size of crystals on top of formatted structure.

As described above, the porosity of the catalyst layer can be achieved by the suitable choice of the substrate material and the deposition conditions of cerium oxide via magnetron sputtering. Similarly to the comparison carried out for morphology (Section 3.1.1.3.2 Influence of Different Carbonaceous Catalyst Support), we can compare the crystals size for different catalyst support. In Fig. 3.33 the magnified images of structures formed on the CeO_x (10 nm)/a-C and CeO_x (10 nm)/CN_x100% samples are displayed. We observe that for a less porous structure on amorphous carbon (Fig. 3.33 a) and b), some crystals are bigger than 10 nm, while in case of highly porous cerium oxide on CN_x100% their size does not exceed 5 nm (Fig. 3.33 c). Moreover, for very porous structures, we have to discriminate the crystals in the deeper areas (Fig. 3.33 d), in the tail of noodles, with sizes ranging from 2 to 3 nm and on the top with a size around 5 nm (Fig. 3.33 e).

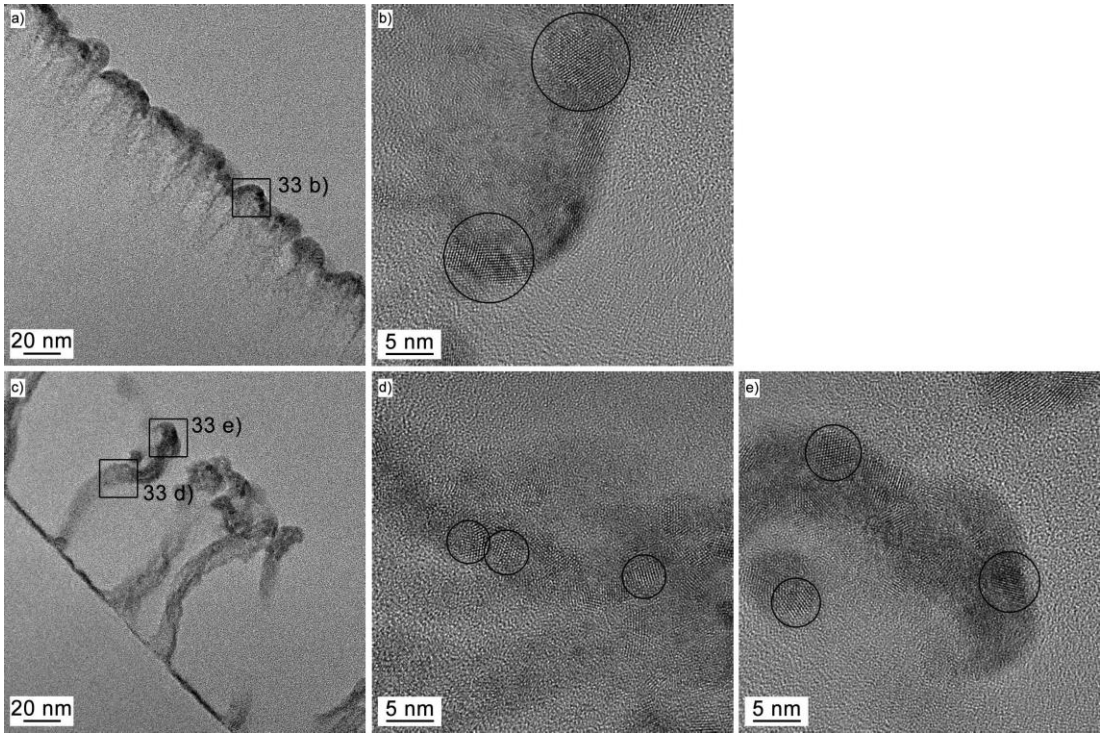

Fig. 3.33 TEM cross-sectional images of CeO_x (10 nm)/a-C a) and CeO_x (10 nm)/CN_x100% c) with magnified areas focused on the size and localization of crystals.

This phenomenon can be related to the processes occurring during the magnetron sputtering of cerium oxide. At the early stage of the deposition, cerium oxide particles cover some parts of the substrate and afterwards, the oxygen plasma etching of carbon occurs only at the unshielded places. Therefore, the porous structure in form of noodles is created. Complementary to the carbon etching, the simultaneous deposition of cerium oxide leads also to the covering of side places of the noodle structures. Since these areas are not easily accessible due to the shielding effect of the adjacent noodles, only very few cerium oxide particles reach these places. Thus, the crystals smaller in size are formed. On the other side, the upper parts of porous structure are exposed to the cerium oxide deposition all the time, which leads to the top cap growing and formation of the bigger size of cerium oxide crystals. Hence, for the crystals size determination, we have to consider not only porosity of the formed catalyst structure, but the localization of crystals, as well.

3.2.1.3 Shape of Crystals

In order to be able to investigate the shape of cerium oxide crystals, observation of really big number of samples is needed from the statistical point of view. We did it, however, oftentimes the deposition conditions were changed and therefore, we cannot compare the shape of crystals in correlation with the substrate type or the magnetron sputtering parameters. Instead of that, we can connect the shape of crystal with their size.

As it was mentioned in the previous chapter, crystals with sizes in the range of 2-20 nm were acquired. While for the particles bigger than 5 nm, we did not record any preferential shape, the smallest ones were observed mostly in the octahedral shape with {111} exposed facets and/or cubooctahedral one with {111} facets truncated by {100} (see Fig. 3.34). These observations are in good agreement with other published works [59, 66, 67], where cerium oxide crystals were prepared in a form of nanoparticles by different methods.

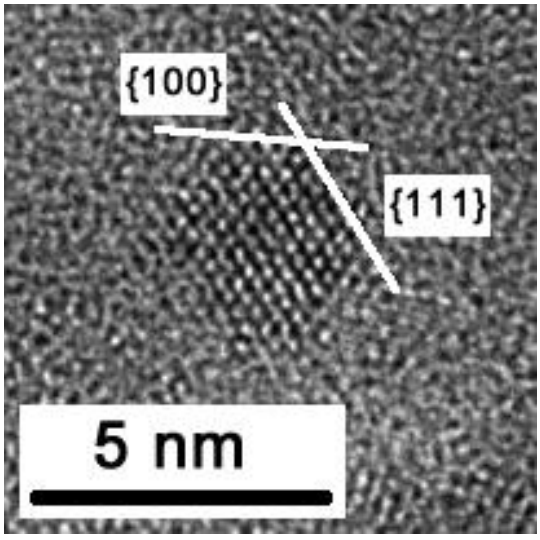

Fig. 3.34 Cubooctahedral cerium oxide crystal with {111} facets truncated by {100} facets.

Moreover, lots of researchers' attention is gained for model studies of cerium oxide preferential shapes [68-70]. Density Functional Theory (DFT) calculations predict that the octahedral shape is the most energetically favoured for the small $Ce_{19}O_{12}$ cluster [57], while for the bigger $Ce_{40}O_{80}$ one, it is a cubooctahedral with

{111} facets truncated by {100} [71]. The same results were obtained by the classical molecular dynamic methods [72]. The {110} facets are occurring neither in the experimental results, nor in the model studies, however, they are predicted as more stable than the {100} facets [73].

The model studies of the cerium oxide crystal shape appear to be very important for the investigation of Pt-CeO_x interaction at the microscopic scale. More particularly, it was shown that the {100} facets are crucial for the Pt adsorption because the presence of four oxygen atoms at {100} facet play a role of a nanopocket for one Pt incorporation [74] and/or its stabilization in the 2+ ionic state [75]. In addition, not only the {100} facets, but also the {100} nanofacets truncating the {111} plane can be the favourable places for Pt adsorption. Such a crystal is displayed in Fig. 3.35.

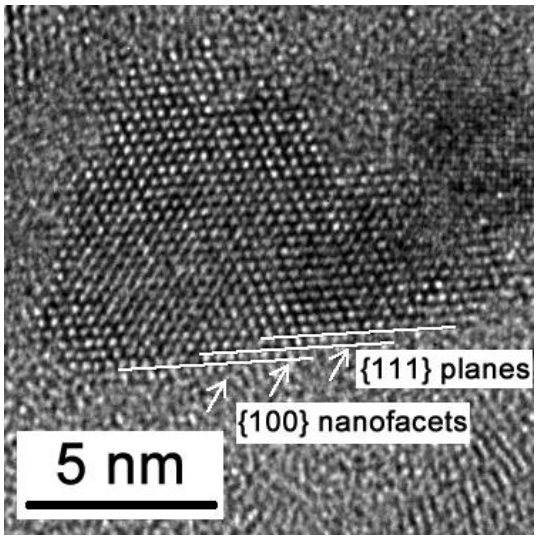

Fig. 3.35 Cerium oxide crystal with {111} facets truncated by {100} nanofacets.

3.2.2 Composition of Cerium Oxide Layers

In the previous section, we have shown the crystalline character of cerium oxide layers. Crystallites were identified mostly as CeO_2, Ce_7O_{12}, or CeC_2; we did not observe any Ce_2O_3 crystal. Despite of that, the amorphous parts between the individual crystals cannot be excluded, and therefore, such places could be filled by reduced cerium oxide.

The chemical composition of catalyst layers offers complementary and very important information about the observed systems. The supplementary methods often used in order to obtain knowledge of the chemical state of individual elements are X-ray Photoelectron Spectroscopy (XPS) and Electron Energy Loss Spectroscopy (EELS). Both of them were applied on the samples prepared in a form of thin layers (XPS) and cross-sectional lamellas (EELS).

3.2.2.1 EELS Characterization

In order to investigate the composition of the catalyst layer and to determine the cerium oxidation state, the EELS study was performed on the cross-sectional samples in form of thin lamellas prepared primary for TEM observations. The EELS spectra were acquired with a 1.5 nm probe in case of the CeO_x layer on the C-foil, and 1.0 nm probe in all other cases, an energy dispersion of 0.3 eV per channel and a Gatan Imaging Filter aperture of 2 mm. The EELS linescans or maps were obtained in STEM mode with very short acquisition time (below 1 s) in order to avoid the sample contamination via an intensive electron beam. The attention was focused on Ce $M_{4\text{-}5}$ edges. The ratio of integrated areas (A_{M5}/A_{M4}) was determined from the measured EELS spectra by applying second derivative method after the background extraction using script implemented in the Digital Micrograph software [76].

As shown in the literature [58, 66, 67], the position, shape and intensity of the Ce M_5 and M_4 peaks allows to determine the oxidation state of cerium. Considering the stoichiometric cerium (Ce^{4+}), the intensity of the M_4 edge is higher than M_5 one, and these symmetric peaks are followed by broader satellites. In case of Ce^{3+} state, the intensity ratio goes in the opposite way, thus, the M_5 edge is higher than M_4 one, and the peaks are less symmetric with weaker features in front of the main edge. Moreover, an energy shift in position to the lower energetic losses is present. On the base of the second derivative method applied on the EELS spectra after the background extraction, we are able to determine the integral ratio of M_5/M_4, where the ratio of 1.3 and higher represents the fully reduced Ce^{3+} state, while the value below 0.9 refers to the stoichiometric Ce^{4+} state [58]. For lanthanides, the ratio dependence on the oxidation state was found to be linear [66, 77], thus the values between 0.9 and 1.3 correspond to the mixture of Ce^{4+} and Ce^{3+} states.

To study the cerium oxidation state, the linescan spectrum was acquired through the sample of the 5 nm thick CeO_x layer deposited on the C-foil (the sample from a series presented in Fig. 3.9), from the substrate-layer interface to the surface, as it is marked by the yellow arrow in Fig. 3.36 a). An example of the Ce M_5 and M_4 peaks is shown in Fig. 3.36 b), where the red curve represents the spectrum acquired close to the C-foil – CeO_x interface and the brown one near the cerium oxide layer surface. Herein, the changes in the shape, energy positions and intensities for the M_5 and M_4 peak are well seen. Concerning the red curve, the M_5 peak is stronger than M_4 one, which indicates a reduced state of cerium close to the carbon surface. On the contrary, as regards the brown curve, the M_4 peak is more intense than M_5 one as cerium becomes less reduced.

In order to investigate the cerium chemical state evolution, the ratio of integrated areas (A_{M5}/A_{M4}) was calculated for the linescan in direction from the C-foil – CeO_x interface to the cerium oxide layer surface. The obtained results are displayed by histogram in Fig. 3.36 c). It can be seen that the ratio obtained close to the carbon substrate is almost 1.30 indicating that cerium occurs mostly in a reduced state. Subsequently, with the probe movement to the catalyst surface, values of the ratio are decreasing to the lowest one of 1.03. This outcome points to gradual changes of cerium stoichiometry from 3+ to 4+. At the very surface, the ratio is again higher ($A_{M5}/A_{M4} = 1.14$).

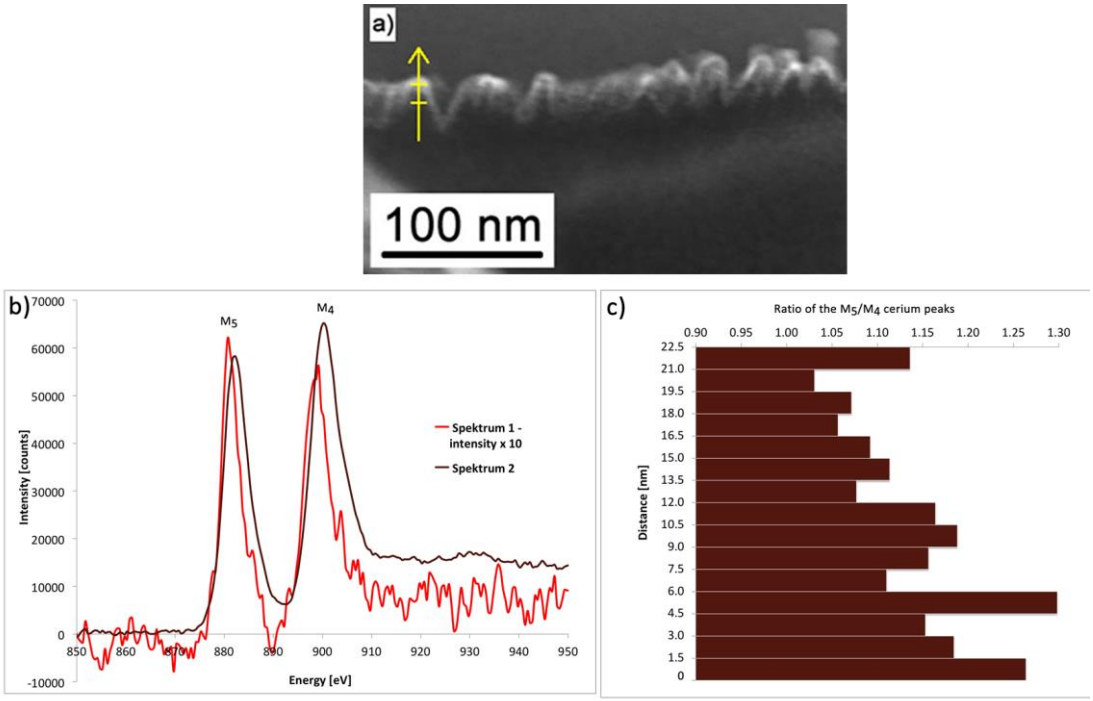

Fig. 3.36 EELS investigation of the 5 nm thick CeO_x layer deposited on the C-foil via a linescan performed from the C-foil – CeO_x interface to the cerium oxide layer surface, as marked by yellow arrow on the STEM image a). An example of Ce M_5 and M_4 edges near the C-foil – CeO_x interface (Spectrum 1, red curve) and close to the cerium oxide layer surface (Spectrum 2, brown curve) b). The plot of the ratio of integrated areas (A_{M5}/A_{M4}) calculated for each EELS linescan spectrum as a function of distance from the C-foil – CeO_x interface c).

The phenomenon of the cerium states transition was investigated by many researchers [58, 66, 67, 77-80], and the generally accepted effect is the reduction of cerium oxide at the surface. Gilliss *et al.* [78] have reported that Ce^{3+} state is present on the surface of all cerium oxide particles randomly crystallographic orientated and with varying size (from several hundreds of nanometers to tens of nanometers). Furthermore, more detailed studies [58] have shown the rapidly increasing reduction with decreasing particle size below 15 nm and the complete reduction of the particles smaller than 3 nm. Besides, the preferential reduction of {100} facets was observed [67, 81]. Turner *et al.* [67] have found that while for the {111} facets the reduced shell was extended over a single fully reduced surface plane and 1-2 underlying mixed valence planes, in case of {100} facets it extended over 5-6 planes. It should play an important role in the catalyst activity.

Concerning the sputtered cerium oxide layer on the carbonaceous support, we have observed variations in the particle size with regard on the substrate material, the deposition conditions, the layer thickness and the nanocrystallite localization. Therefore, the cerium oxide reduction has to be related to these factors, as well. Regardless of that, we have observed surface layer reduction in all cases. It can be associated with the oxygen vacancies presence on the edge of cerium oxide grains forming the surface of the deposited layer. The effect of surface reduction was confirmed by EELS by several groups [58, 67, 78].

On the other side, the reduction near the carbon – catalyst layer interface might be associated with the particle size, where the cerium oxide crystallites have been found much smaller as atop the layer. Moreover, the carbon – cerium interaction has to be considered as well. Unfortunately, to our best knowledge, there are very few publications concerning the cerium carbides [54-56]. The works suggest the cerium valence rather in the 3+ state for the CeC_2 compound. Therefore, we should include also this issue to our explanation of cerium reduction close to the carbon substrate.

In order to support the ideas described above, we display in Fig. 3.37 the ratio of integrated areas for the Ce M_5 and M_4 peaks obtained from EELS maps for the 10 nm thick CeO_x layer deposited on the a-C, CN_x100% and silicon substrates, respectively. The intense red colour represents the more reduced cerium and the more intense brown colour the stoichiometric one. Although the deposition conditions were kept the same for all used supports, the sputtering process of cerium oxide results to very different morphologies, as one can see from the STEM micrographs. Thus, some variation in the cerium oxide reduction can be also expected.

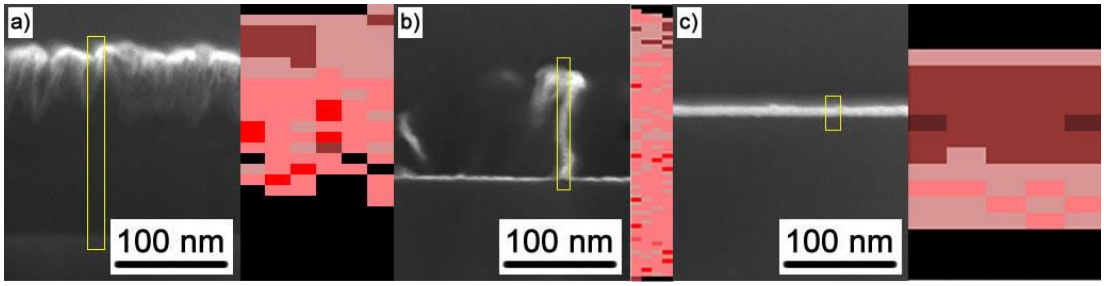

Fig. 3.37 STEM images with the regions of interest (in yellow) for EELS mapping and the related maps of A_{M5}/A_{M4} ratios calculated in each point of EELS mapping for the samples CeO_x (10 nm)/a-C a), CeO_x (10 nm)/CN_x100% b) and CeO_x (10 nm)/Si c).

As one can see from Fig. 3.37, the ratio of integrated areas (A_{M5}/A_{M4}) of the Ce M_5 and M_4 peaks acquired in each point of EELS mapping differs for used supports and also varies with the probe movement from the substrate to the catalyst layer surface. In case of amorphous carbon, the deposited catalyst layer exhibits the morphology of columnar structures. The carbon etching is not as rapid as the cerium oxide deposition, which results in the pillars of tens nanometers covered with almost continuous 8 nm thick surface layer of cerium oxide. Near the carbon substrate, values of the A_{M5}/A_{M4} ratio are ranging from 1.20 to 1.35, which correspond to the higher quantity of cerium in the 3+ state. Besides, we consider the layer to be rather amorphous close to the substrate with very few crystallites smaller than 2 nm. With the on-going scanning to the upper areas, the layer becomes fully crystalized with crystals size up to 5 nm and cerium oxide becoming stoichiometric with regards to the A_{M5}/A_{M4} ratio (0.95 – 1.15).

The catalytic layer of the noodles structure created by the CeO_x deposition on the CN_x100% substrate is reduced to a considerably extent. The EELS map was acquired through the whole structure and the subsequently calculated ratio of integrated areas (A_{M5}/A_{M4}) gives us the values in the range of 1.15 – 1.30. The cerium oxide reduction can be related with the crystal size and an amorphous character of the layer. In the previous section (3.2.1.2 Size of Crystals), we have shown that the about 100 nm long nanonoodles are speckled by crystals smaller than 2-3 nm. Moreover, we suggest that the areas between the small crystallites are fulfilled by amorphous cerium oxide. Only at the top of the layer, the caps become more stoichiometric, as the values of the A_{M5}/A_{M4} ratio are lower (0.95 – 1.15) and

the crystals were observed bigger in size (5 nm). Subsequently, at the very top of the layer, the surface oxygen vacancies result in the cerium oxide reduction.

On the contrary, the cerium oxide layer sputtered on silicon is continuous and well crystalized. The values determining the cerium valence do not exceed 1.05 in the middle area of the deposited film, which implies more or less stoichiometric cerium oxide. Such as in case of carbonaceous substrate, a slight reduction of cerium oxide close to the silicon support was also detected (1.15 – 1.25). It can be caused by the silicon – cerium interaction leading to the silicates and silicides formation [64, 65]. In addition, the surface reduction is present, as well.

From this complex study, we can conclude that the cerium chemical state is conditioned by several factors. It becomes apparent that the main parameter is the porosity of the layers, which is closely related with the crystal size. Similarly, as the smaller particles are liable to the oxygen vacancies [58-60], also in case of sputter deposited layers, the individual crystals with smaller size can lose oxygen easily. Therefore, in the deeper areas of the created catalyst structure, close to the carbon substrate, where only a very few particles are deposited; the layer is amorphous or composed from small crystals predominantly due to the lack of cerium oxide material. In these areas, cerium is present in the oxidation state close to 3+. Moreover, Wu *et al.* [58] have shown that the reduced cerium oxide nanoparticles remain in the fluorite structure, which is the same structure as the structure of bulk CeO_2, while the lattice expansion is occurring. We have observed this anomalous lattice expansion in many cases, which should indicate that longer distances between the cerium ions are due to the electrostatic repulsion originating from the missing oxygen. In addition, we cannot exclude presence of the Ce_2O_3 phase, despite the fact that we did not observe any crystal form.

Complementary, the carbon – cerium interaction leads to the cerium carbides formation. The publications concerning CeC_2 have shown cerium occurring in the 3+ state [54-56]. To exclude the morphology effect on the cerium valence and to support the idea of cerium reduction due to the interaction with carbon, a sample with rather flat, continuous and non-porous layer of CeO_x on the a-C substrate was prepared by magnetron sputtering wit the deposition rate of cerium oxide of 0.2 $nm.min^{-1}$, oxygen partial pressure 1 mPa in Ar working atmosphere and a total pressure kept at 4.10^{-1} Pa. In Fig. 3.38, the STEM image together with the marked

region of EELS mapping acquiring and the map of A_{M5}/A_{M4} ratio of integrated areas for the Ce M_5 and M_4 peaks is displayed. It is well visible that close to the carbon substrate the reduction of cerium is significant (1.20 – 1.30). In addition, by the comparison with Fig. 3.37 c), where the results for the catalyst layer sputtered on silicon are displayed, one can see the major reduction in case of the carbonaceous substrate.

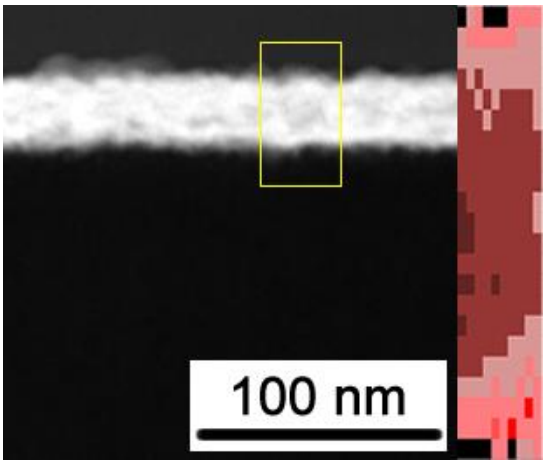

Fig. 3.38 STEM image of the region of interest for EELS mapping and the related map of A_{M5}/A_{M4} ratios calculated in the each point of EELS map for the continuous CeO_x layer deposited on the a-C substrate.

In order to study cerium-carbon interaction in detail, the 3 monolayers (ML) of cerium were evaporated in UHV conditions on C-foil substrate. The very thin, non-crystalized cerium layer as a result of such preparation is visible in Fig. 3.39, where the STEM image of cross-sectional lamella is presented. The region of interest for EELS mapping is marked by yellow rectangle. Corresponding map of A_{M5}/A_{M4} ratio calculated in each point of EELS map is displayed as well. Calculated values refer to reduce cerium through the whole layer, however stronger effect is visible for cerium close to the carbon interface. It can points to cerium reduction due to the interaction with carbon [54-56].

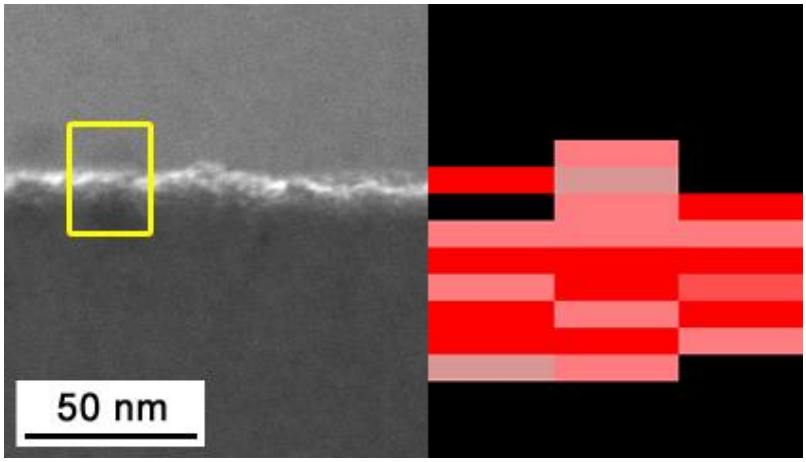

Fig. 3.39 STEM image of the region of interest for EELS mapping and the related map of A_{M5}/A_{M4} ratios calculated in the each point of EELS map for 3ML of Ce layer evaporated on the C-foil substrate.

3.2.2.2 XPS Characterization

For purpose to confirm results obtained by EELS spectroscopy concerning cerium oxide reduction, the XPS spectroscopy was performed. The XPS signal is of an integral character over the entire surface of the sample; therefore, it offers information about cerium electron state on global scale contrary to EELS data, which have a local character. Moreover, the measurement is performed on as-prepared sample, i.e. any further preparation method is needed, as it is in case of EELS spectroscopy. Such cross-sectional lamellas used for EELS analysis could be damage by gallium ions during FIB preparation [82-84], as the electronic state of cerium can be change due to the incidence of highly energetic gallium ions. In addition, during scanning through the sample in TEM, the further reduction can be caused by interaction with electron beam at high voltage [85]. Thus, the XPS spectroscopy was chosen as a supplementary method to EELS spectroscopy for cerium electronic state verification. On the other hand, it is necessary to keep in mind that XPS is a surface sensitive method with information depth is about 1-5 nm.

The chemical state and the composition of the 1, 5 and 20 nm thick CeO_x layer deposited on C-foil were investigated. In Fig. 3.40, the XPS Ce 3d core level spectra are compared. Each spectrum consists of three $3d_{5/2}$–$3d_{3/2}$ spin–orbit-split doublets characteristic of the Ce^{4+} states which are a sign of stoichiometric cerium

dioxide (CeO_2) and two doublets evidencing the formation of Ce^{3+} ions [86, 87]. An example of the decomposition of the Ce 3d spectrum to sums of Ce^{4+} and Ce^{3+} doublets is shown for the 1 nm thick layer of CeO_x (according to Skala *et al.* work [88]). From the shapes of the Ce 3d spectra in Fig. 3.40 one can see that the contribution of the Ce^{3+} states in comparison with Ce^{4+} ones is increasing with decreasing thickness of the cerium oxide layer.

In the bottom part of Fig. 3.40, there are two curves (solid and dotted) added representing Ce 3d spectra taken for the CeO_x (5 nm)/C-foil sample after removal of the catalyst layer in H_2SO_4 acid. The solid line shows the spectrum at the same scale as the other Ce 3d spectra presented. The intensity of the Ce 3d spectra for the sample after flushing out is negligibly small (the bottom solid line). The spectrum multiplied by 10 (the dotted line) shows that cerium is solely in the Ce^{3+} state. The results indicated that it could be the residues of cerium carbide where cerium atoms are in the Ce^{3+} oxidation state [54, 55]. We can conclude that acid treatment successfully removed the cerium oxide layer except only traces of the catalyst.

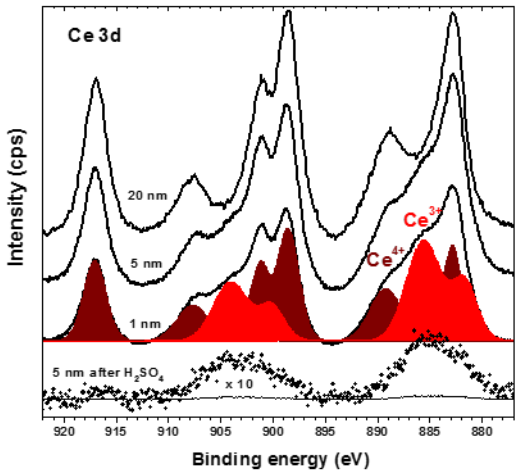

Fig. 3.40 XPS Ce 3d core level spectra of 1, 5 and 20 nm thick CeO_x layer deposited on the C-foil substrate complemented by the spectra after removing the CeO_x layer of 5 nm nominal thickness in H_2SO_4 acid (bottom curves). Red and brown lines represent the decomposition of the Ce 3d spectrum to sums of Ce^{4+} and Ce^{3+} doublets for a 1 nm thick layer of CeO_x/C-foil.

The data presented in Fig. 3.40 point to the fact that the cerium oxide catalyst layers are of Ce^{3+} and Ce^{4+} mix valence and the cerium reduction is irreversibly dependent on the layer thickness. In the thin CeO_x layers (nominal thicknesses of 1 nm and 5 nm) cerium occurs substantially in the Ce^{3+} state (43% and 40% of cerium atoms) and with increasing thickness of the catalyst layer it occupies more the Ce^{4+} states. The layer with 20 nm of nominal thickness looks nearly stoichiometric (with 75% of cerium atoms in the Ce^{4+} state). The value agrees well with the A_{M5}/A_{M4} ratios obtained for the upper part of the layer (Fig. 3.36 c). It is necessary to note that in case of XPS the Ce^{3+} concentration in a sub-surface region, is not a simple average value because the signal intensity is attenuated according to the Beer–Lambert law with depth. So, since more reduced cerium oxide occurs at the carbon–CeO_x interface, the Ce^{3+} state is suppressed in this case. This behaviour fits very well with the EELS data obtained by linescan through the 5 nm thick layer from the interface to its surface (Fig. 3.36). The EELS spectra show reduced cerium oxide at the C-foil–CeO_x layer interface becoming gradually more stoichiometric to the surface. The presence of cerium atoms solely in the Ce^{3+} state at the C-foil surface was also confirmed by XPS on the sample after removing the cerium oxide layer in H_2SO_4 acid.

In order to study cerium-carbon interaction by XPS method in detail, the Ce 3d spectra for 3 ML cerium catalyst evaporated in UHV conditions on C-foil were acquired. As one can see in Fig. 3.41, the as-prepared cerium layer measured *in situ* is fully reduced (the bottom spectrum), with cerium solely in 3+ state. However, after the exposure to the air, the doublets for Ce^{4+} have appeared (the top spectrum). It points to easily surface cerium oxidation, while cerium in deeper areas stays in reduced form. It can be again associated with cerium-carbon alloys formation, in which Ce in 3+ state is present [54-56]. This spectrum is comparable with the map of A_{M5}/A_{M4} ratios calculated in each point of EELS mapping displayed in Fig. 3.39. Cerium is reduced through the entire layer, however stronger reduction effect is visible for cerium-carbon interface.

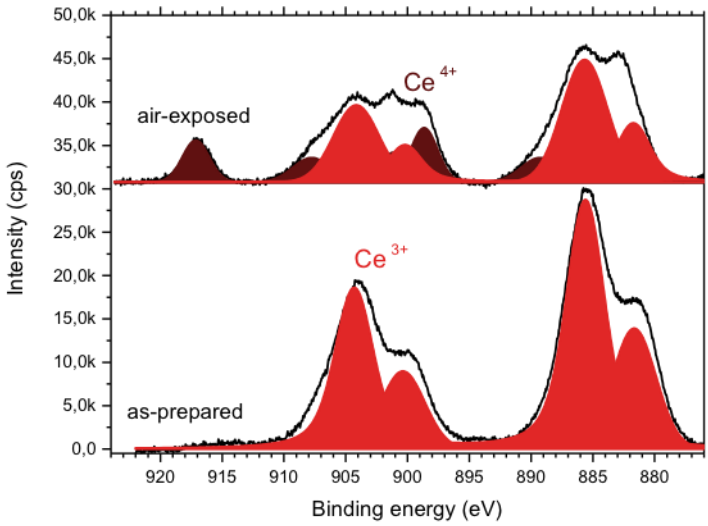

Fig. 3.41 XPS Ce 3d core level spectra of 3 ML thick Ce layer evaporated on the C-foil substrate. The bottom spectrum represents as-prepared film acquired *in situ* in UHV conditions, the top spectrum the film after the air exposure. Red and brown lines represent the decomposition of the Ce 3d spectrum to sums of Ce^{4+} and Ce^{3+} doublets.

Thus, the obtained results allow us to complete the growth model of cerium oxide on carbonaceous substrates proposed in Figs. 3.12 and 3.19 [17]. The cerium oxide sputtering process on carbon material leads to the simultaneous cerium oxide deposition and carbon etching by oxygen plasma. It results in changes in morphology and porous structure formation, which can be tuned by suitable deposition conditions. Moreover, cerium carbide compounds are formed close to the carbon – catalyst layer interface. In addition, the variation of the cerium chemical state is observed, as schematically drawn in Fig. 3.42. Near the carbon support, where the very small crystals dispersed in an amorphous layer are observed, cerium occurs in the 3+ oxidation state, while with ongoing movement to the surface of the catalyst layer, and thus to the caps with bigger crystals, the Ce valence is gradually changed to stoichiometric cerium in the 4+ state. At the very surface, cerium is becoming slightly reduced to Ce^{3+} due to the oxygen surface vacancies.

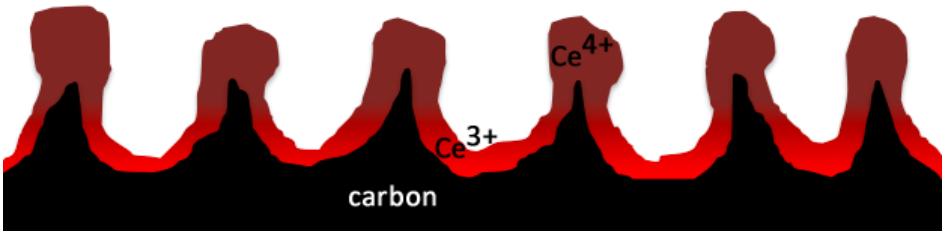

Fig. 3.42 Schematic model of a cerium oxide layer deposited on a carbonaceous substrate exhibiting a porous structure supplemented by the cerium chemical state (intense red – Ce^{3+}, brown – Ce^{4+}).

3.3 Platinum Doped Cerium Oxide Layers

Chosen method of preparation, magnetron sputtering, constitutes a fast and inexpensive way of preparing high-surface-area nanostructure catalyst films that allows to synthesize a large variety of catalytic materials based on a myriad of elements combinations at many different compositions. In case of a combination of the carbonaceous substrate and cerium oxide as deposited material the sputter deposition exhibits specific features. As we have shown, the selection of appropriate deposition parameters and/or conditions leads to the extremely porous structure formation influencing also the crystallographic structure of the prepared cerium oxide layer as well as its stoichiometry. The above-presented investigation concerning the catalyst support structure and composition, as well as the cerium oxide layer itself and related morphological and compositional changes, extended our knowledge about fundamental processes occurring during the cerium oxide magnetron sputtering, which play a key role in catalyst preparation. This detailed knowledge about elemental processes and effects taking place in the preparation of the catalytic system on the base of carbonaceous material supported cerium oxide allows us to prepare catalytic surfaces of designed properties. The last unknown parameter, to which it is necessary to focus, is an influence of platinum doping.

Herein, in this section, we will deal with the study of cerium oxide based catalyst layers enriched by platinum with a special focus on the impact of the Pt concentration on changes in the layer morphology, crystal structure and composition. The simultaneous deposition of Pt and CeO_x was carried out via magnetron sputtering of ceria target with platinum wires placed on the surface, which number varied from 0 to 3 to achieve layers with different Pt concentration. The total concentration of Pt dopant was set on the basis of XPS measurements, as 0%, 6%, 16% and 28%, respectively. Note that in following sections, we use labelling Pt0, Pt1, Pt2 and Pt3 to describe the Pt wires number used for the preparation of the catalyst layers rather than the Pt concentration.

3.3.1 Changes in Morphology

In order to study the influence of platinum doping on cerium oxide film morphology, the 2, 10 and 20 nm thick Pt-CeO_x layers were sputtered on the 200 nm thick a-C, CN_x100% and CN_x50% (100 nm)/a-C (100 nm) films supported by silicon (see Section 3.1.1. Morphology and Structure of Catalyst Support). The TEM micrographs acquired from the cross-sectional lamellas are displayed by collages in Fig. 3.43, 3.45 and 3.47 for the a-C, CN_x100% and CN_x50%/a-C films, respectively. Moreover, the values of thickness for non-etched carbon and the created porous structure are presented in charts in Fig. 3.44, 3.46 and 3.48.

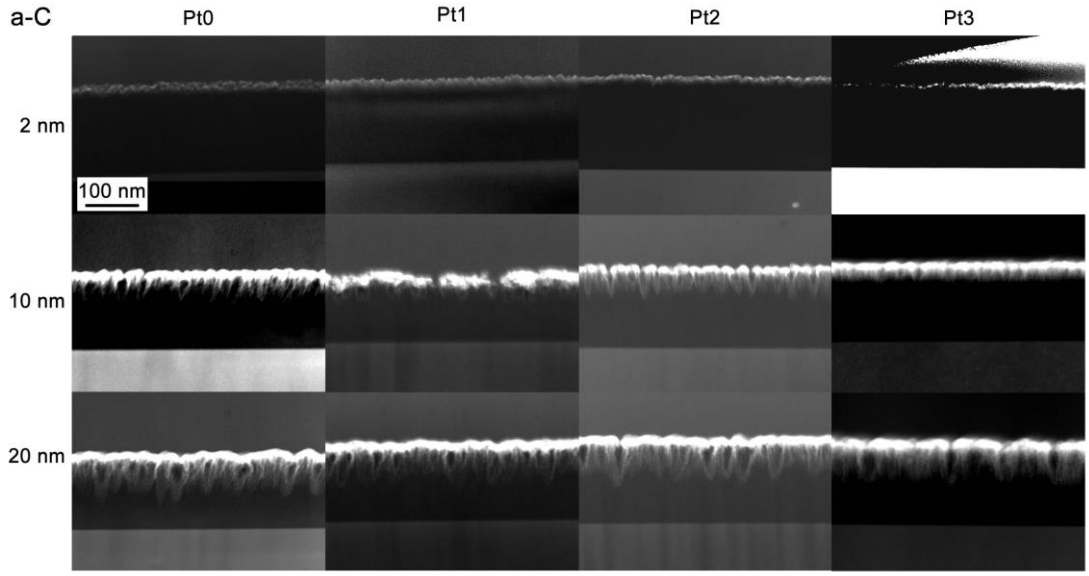

Fig. 3.43 STEM cross-sectional images of the 2, 10 and 20 nm thick Pt-CeO_x layers as a function of Pt doping (Pt0, 1, 2, and 3, respectively) on the a-C film supported by silicon.
Si is present at bottom part of the micrographs.

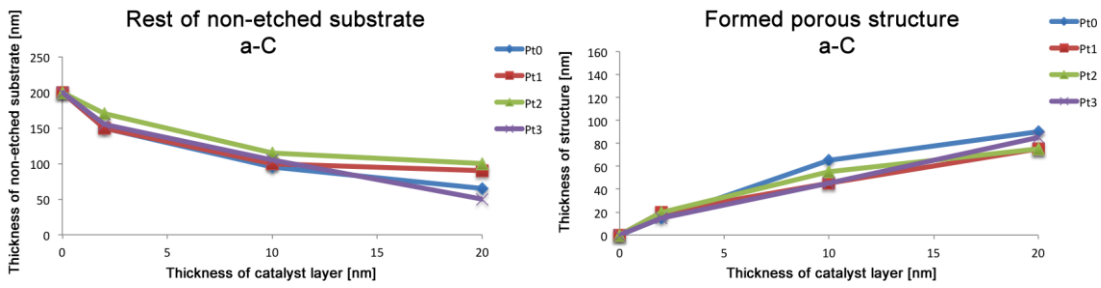

Fig. 3.44 Thicknesses of non-etched substrate versus thickness of deposited catalyst layer for different Pt doping (Pt0, 1, 2, and 3, respectively) measured on the Pt-CeO_x layers supported by the a-C film on silicon.

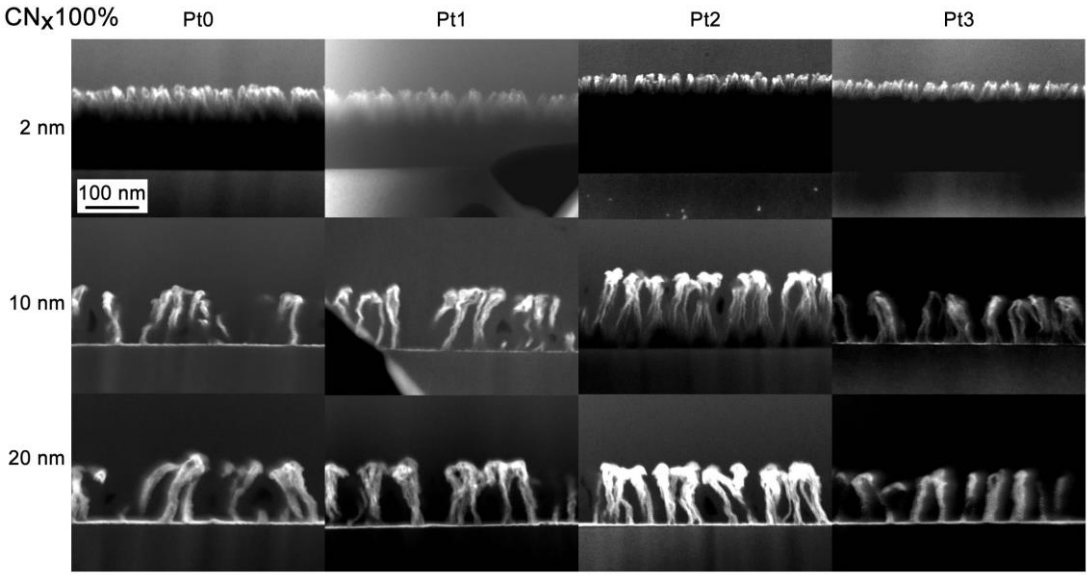

Fig. 3.45 STEM cross-sectional images of the 2, 10 and 20 nm thick Pt-CeO_x layers as a function of Pt doping (Pt0, 1, 2, and 3, respectively) on the CN_x100% film supported by silicon.
Si is present at bottom part of the micrographs.

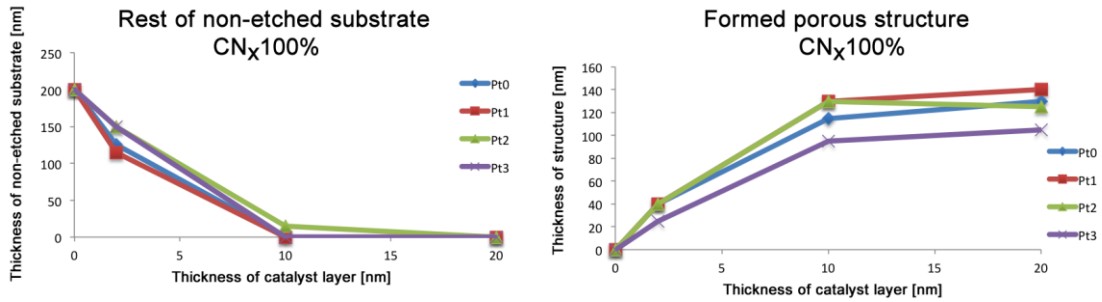

Fig. 3.46 Thicknesses of non-etched substrate versus thickness of deposited catalyst layer for different Pt doping (Pt0, 1, 2, and 3, respectively) measured on the Pt-CeO_x layers supported by the CN_x100% film on silicon.

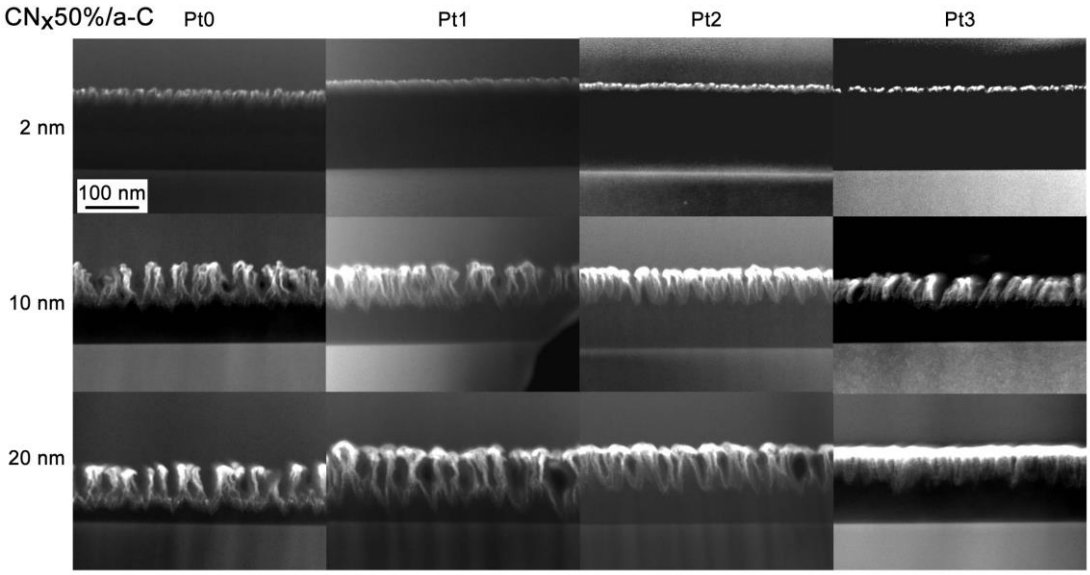

Fig. 3.47 STEM cross-sectional images of of 2, 10 and 20 nm thick Pt-CeO_x layers as a function of Pt doping (Pt0, 1, 2, and 3, respectively) on the CN_x50%/a-C film supported by silicon.
Si is present at bottom part of the micrographs.

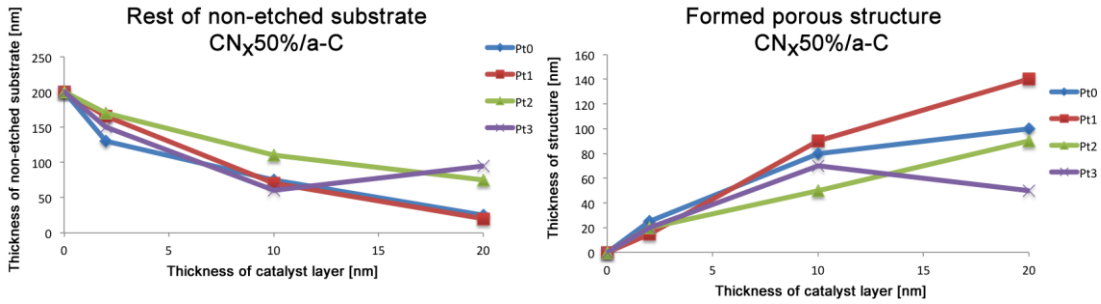

Fig. 3.48 Thicknesses of non-etched substrate versus thickness of deposited catalyst layer for different Pt doping (Pt0, 1, 2, and 3, respectively) measured on the Pt-CeO_x layers supported by the CN_x50%/a-C film on silicon.

As one can see by comparing the images in Fig. 3.43 and 3.45 and/or the values set in chart in Fig. 3.44 and 3.46, respectively, the changes in morphology with increasing Pt concentration are not so significant for the a-C and CN_x100% substrates.

In case of the a-C substrate (Fig. 3.43 and 3.44), some small differences can be slightly visible for higher Pt amount: the non-etched carbon thickness is increasing, while the thickness of created porous structure is decreasing. However, the changes in morphology with increasing deposition time of the catalyst layer, i.e.

with the deposited thickness of catalyst layer, are well comparable. Similarly to the case of cerium oxide deposited on C-foil (see Section 3.2.1.3.1 Influence of Cerium Oxide Deposition Time), at the early step of growth, the grainy structure of cerium oxide is visible. With on-going deposition, the etching of carbon substrate is taking place and thus, the porous structure formation occurs. Further catalyst layer deposition does not change the thickness of etched carbon significantly, while the surface is covered by deposited material, which prohibits oxygen plasma etching of carbon. Regrettably, some break during the deposition process of Pt1-CeO_x (10 nm)/a-C has occurred, as the morphology study shows the high conglomeration of the catalyst layer.

Concerning the CN_x100% film (Fig. 3.45 and 3.46), the etching effect of nitrogenated carbon is much higher than for the a-C substrate, as it was reported in Section 3.2.1.3.2 Influence of Different Carbonaceous Catalyst Support. At the beginning of magnetron sputtering, the hilly-like structure is formed. Herein, the slight influence of Pt amount increase in deposited layer is visible: the higher Pt concentration, the slower CN_x100% film etching (case of the 2 nm thick Pt2-CeO_x and Pt3-CeO_x layers). With further deposition, the whole carbonaceous substrate is etched and noodle structure has almost the same height regardless the Pt concentration, except the 10 nm thick Pt2-CeO_x layer, where the rest of non-etched carbon substrate can be seen. Thus, we can conclude that the very high etching rate of the CN_x100% film prevails over the Pt adding effect. Moreover, it seems that some break occurred in deposition conditions for the magnetron sputtering process with 3 platinum wires, as the values of total thickness is smaller than in case of 2 wires.

It is apparent that the most sensitive substrate to the Pt amount variation is the combination of the CN_x50% and a-C layers (Fig. 3.47 and 3.48). The non-doped CeO_x layer deposition results in the very porous structure containing individual noodles created from CN_x50% accompanied by small peaks occurring between them as a result of the a-C film etching. This effect is caused by double layer composition, as the etching rate of CN_x50% and the a-C support is different. Comparing the images for 10 nm thick Pt-doped and non-doped catalyst layers the differences are negligible. On the contrary, the changes in morphology caused by adding platinum are significant for the catalyst layers after deposition of 20 nm catalyst. The thickness of porous structure, as well as the thickness of non-etched carbon is

significant higher for the doped layer by using 1 Pt wire than for the non-doped one. It confirms that by adding Pt in the catalyst layer, the etching rate of carbon is slower, thus, the porous structure and non-etched carbon are thicker. Additionally, further increase of Pt concentration in the catalyst layer results in even thicker non-etched carbon part. However, the thickness of porous structure is smaller with less opened pores. We do not include to this comparison catalyst layesr with 3 Pt wires, since it seems that some break during the deposition process has occurred.

From herein mentioned results regarding the morphological changes with variable Pt concentration, we assume that the higher amount of Pt leads to the faster covering of carbonaceous substrate. As a consequence, larger carbon surface area is shielded by deposit at the beginning of magnetron sputtering process and the oxygen plasma etching of carbon is prohibited at many places. Hence, the thickness of non-etched carbon is increasing with higher Pt concentration, while the formed structure is less porous and smaller. In addition, the total thickness of the Pt-CeO_x/carbonaceous substrate system is increasing, as well. Therefore, it can be claimed that the more Pt in the catalyst layer, the slower etching effect of carbon and subsequently, formation of the less porous structure.

3.3.2 Changes in Crystallography

The crystallography observations of the non-doped cerium oxide layers, mentioned in the previous part (Section 3.2.1 Crystallography Study) have shown that the deposition process leads to the formation of cerium oxides and cerium carbides crystals. The simultaneous sputtering of Pt and CeO_2 on carbonaceous substrates can result to the additional presence of Ce-Pt compounds, platinum oxides or carbides and/or metallic Pt crystallites. Hence, the unambiguous crystal identification is even more complicated than for the non-doped layers due to the large amount of elements and their possible combinations.

In order to perform the crystallographic investigation in detail, the 2, 10 and 20 nm thick layers of Pt-CeO_x with variable Pt concentration (marked as Pt1, 2 and 3, respectively) were deposited on the a-C, CN_x100% and CN_x50%/a-C films and the Si substrate used as a reference. After the lamellas preparation suitable for HRTEM

observation, a profusion of images was acquired, analysed and compared with data obtained from the crystallographic database [51].

Concerning the Pt1-CeO_x catalyst layer sputtered from the CeO_2 target with one Pt wire placed on its surface, in the most cases, besides the CeO_2 and CeC_2 crystals, we observed some distances and angles, which correspond to the zone axis of $CePt_2$ [001]. Nevertheless, this identification is not unambiguous due to the very similar values for the CeC_2 [001] crystal. Therefore, we will not mention this zone axis any more for any Pt concentration. Despite of difficulties, which resulted from similarity of values for different crystallites, we identified some of them without any doubts. The $CePt_2$ [111] crystal was observed for the CN_x50%/a-C substrate (Fig. 3.49 a), as well as $CePt_5$ [100] and $CePt_5$ [421] (not displayed) for the silicon support. Even though the Pt concentration in CeO_x is rather small (i.e. case of Pt1 loading) for metallic clusters formation, the Pt [001] crystal was acquired on the Si substrate. The platinum oxide observation was rare as well, as we report only one PtO_2 [110] crystal on the CN_x100% film. We note that all these crystallites were observed for thicker catalyst layers, with nominal thicknesses of 10 and/or 20 nm.

For the Pt2-CeO_x system, i.e. with higher Pt concentration (2 Pt wires), the probability to identify the platinum oxide crystals and metallic Pt particles has increased. Small Pt [101] crystallites were observed not solely for the Si substrate, but also in case of the a-C (Fig. 3.49 c) and CN_x100% films. Similarly, PtO_2 [110] was found for the 20 nm thick Pt-CeO_x layer on the a-C film (Fig. 3.49 d). Moreover, CePt compounds in form of $CePt_5$ [100] were acquired on carbonaceous substrates (Fig. 3.49 b).

In case of the Pt3-CeO_x layers sputtered from 3 Pt wires with 28% Pt concentration, we did not obtain any CePt compounds, nor platinum oxides, but solely metallic Pt crystals with zone axis orientation [101].

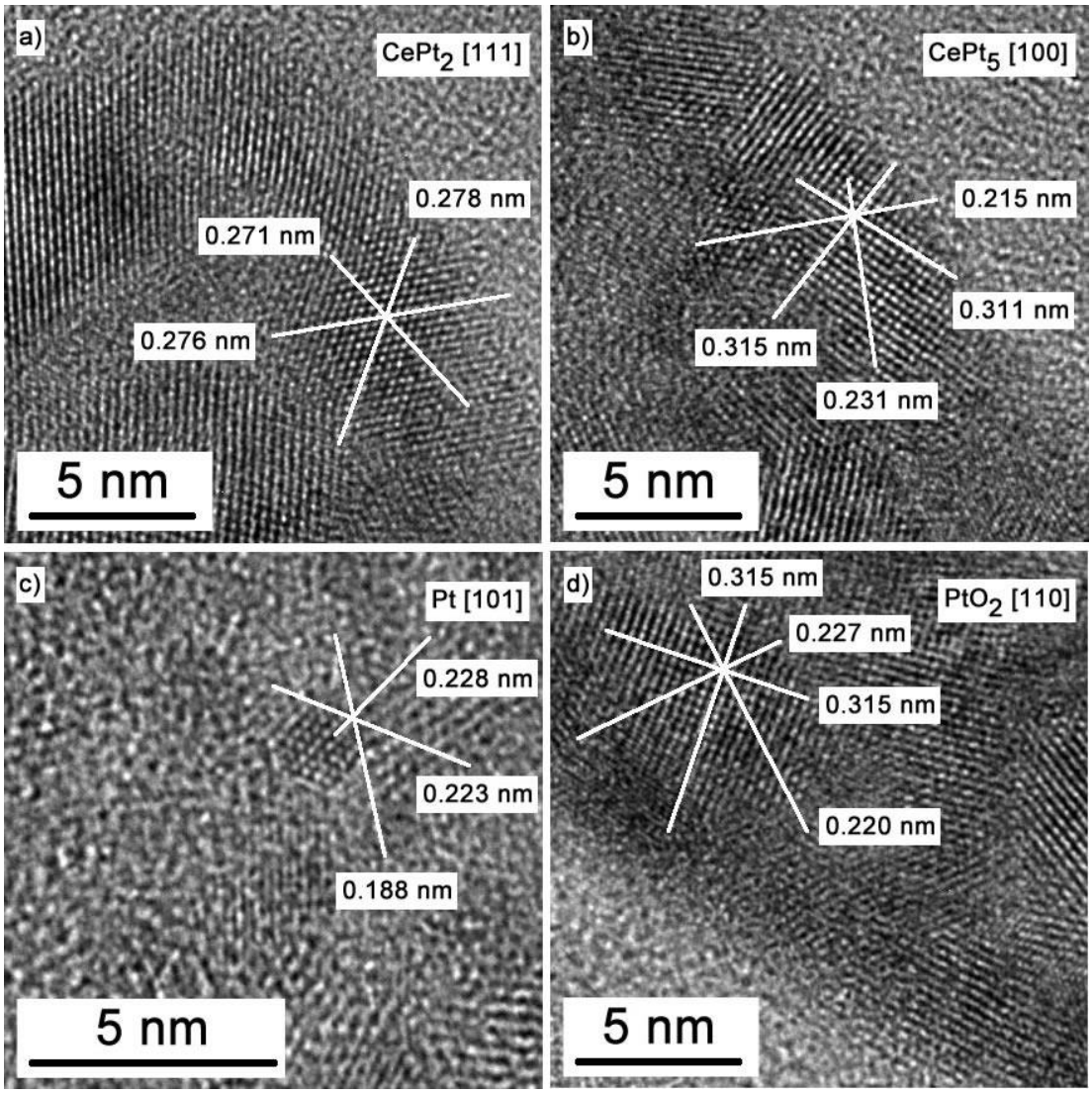

Fig. 3.49 HRTEM micrographs of nanocrystals observed in Pt doped cerium oxide layers on carbonaceous substrate and silicon identified as $CePt_2$ [111] (Pt1-CeO_x(20 nm)/CN_x50%/a-C) a), $CePt_5$ [100] (Pt2-CeO_x(20 nm)/CN_x100%) b) Pt [101] (Pt2-CeO_x(20 nm)/a-C) c) and PtO_2 [110] (Pt2-CeO_x(20 nm)/Si) d).

The crystallographic investigation for different substrates and variable concentration of Pt has shown the evolution of crystals variation with amount of Pt dopant. Doping of CeO_x layers by Pt results in the CePt compounds creation, in our case, in form of $CePt_2$ and $CePt_5$ [49, 89, 90]. However, the phase diagram of bulk binary Ce-Pt alloys exhibits a number of stable intermetallic phases [91], which display a variety of electronic and magnetic ground state properties [92, 93]. In addition, Janghorban *et al.* [91] have shown in phase diagram that the Ce-Pt alloys revealed a rich variety of atomic structures appearing with variation in Pt concentration during alloying procedure. The $CePt_2$ crystallites contain homogeneity

domains with 66-75% of Pt in crystal structure, while in $CePt_5$ was found 85-95% of platinum. Then, we can assume that for crystal formation of $CePt_5$ higher Pt concentration is needed, i.e. the $CePt_2$ can be preferentially created in case of lower Pt amount in the Pt-CeO_x layer. It is in accordance with our observation, as the most recorded crystals matched with $CePt_2$. Nevertheless, the energy configuration and findings concerning the electronic structure for Ce-Pt compounds are inconsistent and they are the subjects of very recent experimental and theoretical studies [94-96].

The increasing amount of Pt in the catalyst layer leads to the higher quantity of platinum oxide crystals. Additionally, higher Pt concentration causes formation of Pt atoms to the clusters and/or to the metallic Pt crystals, as it is visible from Fig. 3. 50 (small dark spots correspond to Pt clusters). Complementary to the more frequent observation of Pt crystallites with higher Pt concentration, we noticed that the crystals size is decreasing with Pt amount increasing. In Table 3.6, the number of observed crystallites with approximate size as a function of number of used Pt wires is shown.

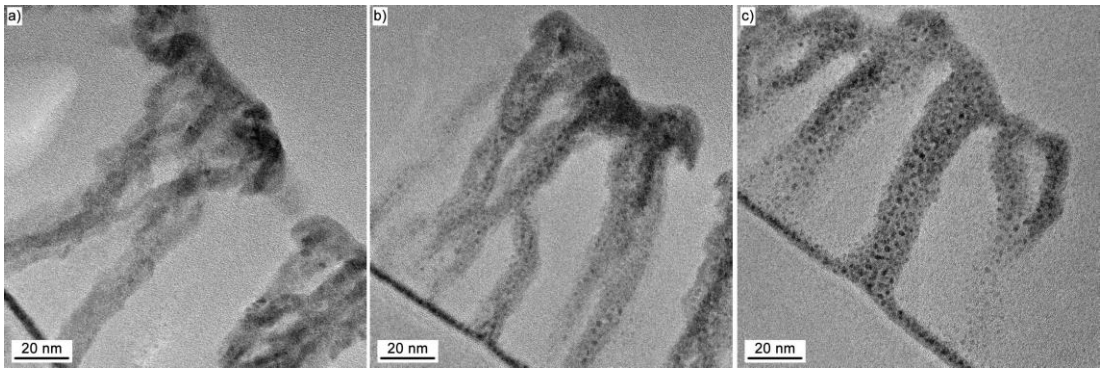

Fig. 3.50 TEM images reporting to changes in crystallography due to increasing Pt concentration in the 20 nm thick Pt-CeO_x catalyst layer sputtered on the CN_x100% film supported by silicon; Pt1-CeO_x a), Pt2-CeO_x b) and Pt3-CeO_x c).

Crystallite	Pt1	Pt2	Pt3
PtO_2	1x (20 nm/CN_x100%, size ≈ 7 nm)	2x (20 nm/a-C, 20 nm/Si, size ≈ 5-7 nm)	-
$CePt_2$	3x (20 nm/CN_x50%/a-C, 10 nm/Si, 20 nm/Si, size ≈ 8-10 nm)	1x (20 nm/Si, size ≈ 6 nm)	-
$CePt_5$	2x (10 nm/Si, size ≈ 8 nm)	2x (20 nm/a-C, 20 nm/CN_x100%, size ≈ 7-8 nm)	-
Pt	1x (10 nm/Si, size ≈ 4 nm)	4x (10 nm/a-C, 20 nm/a-C, 20 nm/CN_x100%, size ≈ 2 nm)	9x (20 nm/CN_x50%/a-C, 10 nm/CN_x100%, 20 nm/CN_x100%, size ≈ 2-3 nm)

Table 3.6 The number of observed crystallites with approximate size as function of number of Pt wires.

3.3.3 Changes in Composition

3.3.3.1 EDX Characterization

In order to study the Pt distribution in the Pt-CeO_x layers, the EDX spectra were acquired in the frame of linescans and/or mapping through the created porous structures on the carbonaceous substrates.

In Fig. 3.51, the EDX linescan spectra acquired through the 20 nm thick Pt-CeO_x layers with different Pt concentration deposited on the a-C films are compared. For better illustration, we display signals of all elements detected in the area marked by the green line in corresponding STEM image of the sample presented below the EDX linescan spectra.

As one can see, for low amount of Pt (Fig. 3.51 a), i.e. one Pt wire, we did not detect almost any Pt signal. The slight increase of intensity occurs at the brightest places of the sample; however, we cannot exclude the parasite signal. Contrary, the cerium signal is increasing with on-going probe movement from the silicon support, through the carbonaceous film and the catalyst porous structure to the cerium oxide surface. It is possible to estimate the thickness of silicon oxide layer at the interface between the silicon support and the deposited a-C film, the thickness of non-etched carbon, as well as the thickness of created porous structure. These values are in good agreement with the results obtained by the direct thickness measurement from the TEM image (see Figs. 3.43 and 3.44). Moreover, the shape of Ce signal indicates that the distribution of cerium is not uniform along the porous structure. The significant increase of Ce signal intensity confirms the caps formation on the top of structure, which merge to continuous layer as more material is deposited, while in the deeper areas the signal is smoothly decreasing with decreasing amount of cerium oxide deposited in deeper regions of formed porous strucutre.

In contrast, we detect very strong Pt signal for the Pt2-CeO_x layer on the a-C film (Fig. 3.51 b). Furthermore, the tendency of platinum intensity is similar to the cerium one, i.e. it is continuously increasing from the bottom of the porous structure to its surface. Then again, at the very surface, the most intense signal points at the caps on the top of the structure and continuous layer formation. The rapid drop in signal demonstrates the sharp end of the porous structure. On the other side, it is remarkable that the intensity of Pt and Ce signal in the deeper areas has similar values. The higher Pt concentration in comparison to Ce can lead to the Pt clusters formation, and therefore, it can explain the observation of metallic Pt crystals mostly in these areas.

Similarly, the EDX linescan spectrum through the Pt3-CeO_x layer on the a-C film evinces the same character as in case of Pt2, though the Pt signal intensity is even higher (Fig. 3.51 c).

It should be noted that the Si signal detected on the left side of the linescan spectra originates from the silicon substrate. On the right side, it is coming from the silicon protective layers deposited on the samples surfaces prior the lamella preparation in order to protect the sample surfaces.

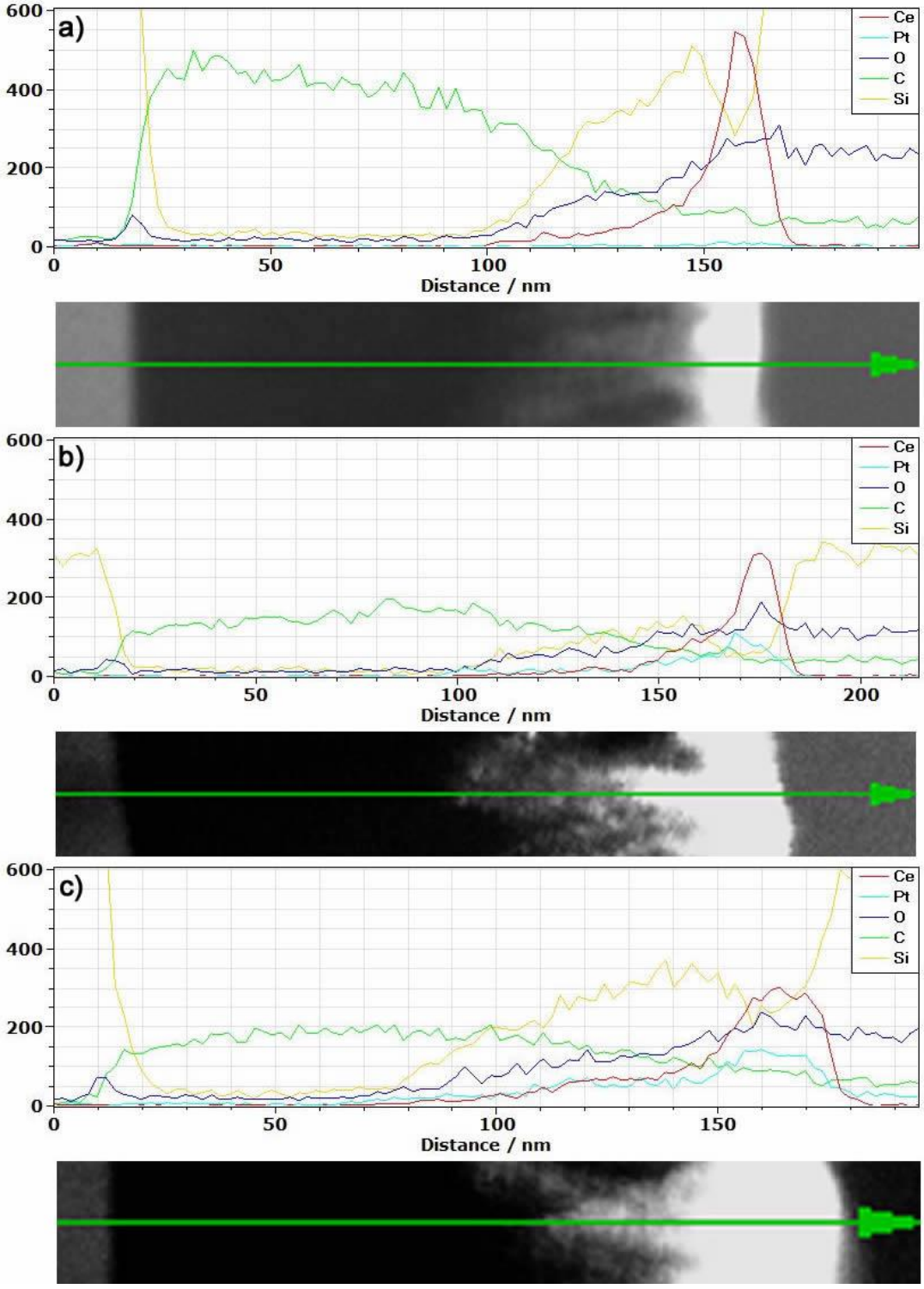

Fig. 3.51 EDX spectra of platinum and cerium signal acquired through the Pt-CeO_x layers with various amount of Pt deposited on the a-C substrates. Pt1-CeO_x (20 nm)/a-C a), Pt2-CeO_x (20 nm)/a-C b) and Pt3-CeO_x (20 nm)/a-C c).

Due to the variation in the platinum and cerium signal intensity, i.e. in their concentration, through the porous structure created on the amorphous carbon film, we are not able to set the amount of platinum in deposited layers, which would be

comparable with the value of concentration determined from XPS measurement. For this reason, we displayed in Fig. 3.52 the mass percentage quantification of elements contained in the linescan EDX spectra acquired through the 10 nm thick Pt2-CeO_x layer on the silicon substrate. As one can see, the concentration of Pt and Ce has similar tendency with maximum in the middle of deposited layer, where the Pt concentration varies in range of 10-15%. It is close to 16% determined by XPS, however, we are rather careful with such a comparison. It should be borne in mind that the concentration calculation of platinum and cerium in the deposited layers using EDX and XPS spectroscopies has its limitations. The XPS signal is of an integral character over the entire surface of the sample, i.e. XPS "sees" the tops of hilly-like carbon structures as well as on their flanks and across the valley, and a signal from deeper regions of the deposited layers is attenuated. On the other hand, the EDX measurements were done on the cross-sectional sample prepared by FIB. During the lamella preparation, platinum from the precursor used for fixation of the lamella on tip by the ion beam deposition technique as well as on TEM copper grid and the further polishing could redeposit such kind of platinum on the lamella. Moreover, the non-uniform thickness of lamella could also cause the signal variation.

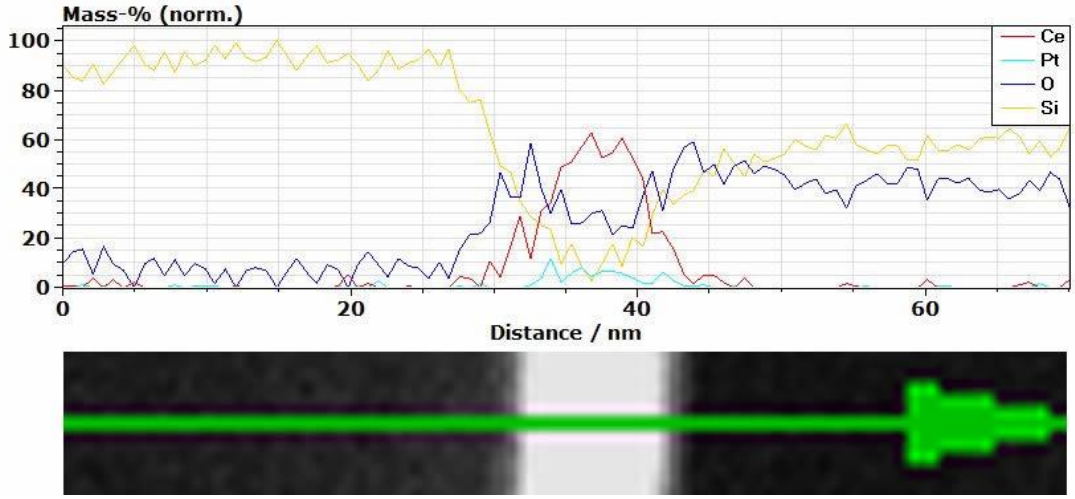

Fig. 3.52 Mass percentage elements quantification obtained from EDX spectra acquired through the 10 nm thick Pt2-CeO_x layers deposited on the Si substrate.

Instead of precise concentration determination, we focused our attention on the spatial distribution of elements in the porous structures with different

carbonaceous films. Fig. 3.53 shows the element maps of Pt and Ce acquired on areas displayed in corresponding STEM images for the 20 nm thick catalyst layers sputtered from the ceria target with 2 Pt wires on its surface.

In case of the a-C film (Fig. 3.53 a), the results support the above-presented linescan data, which point at the preferential distribution of Pt and Ce in the upper areas of the sample. It is connected with the shape of the porous structure, where the caps atop the surface are formed. As more material is sputtered, they become bigger and merge to the continuous catalyst layer. Therefore, further carbon etching is prohibited, as well as the deposition of Pt and Ce in the deeper areas.

The extremely porous structure in form of individual nanonoodles is formed as a result of the deposition of the Pt2-CeO_x layer on the CN_x100% film. In contrast to the a-C substrate, the whole noodles structures are strewn with cerium and platinum (Fig. 3.53 b). As mentioned before, it is connected with the nature of sputtering process including the catalyst deposition and very fast CN_x100% film etching. The distances between the individual nanonoodles are large and thus, lots of places are “opened” to the Pt and Ce species adsorption. Nevertheless, the highest concentration belongs also to the areas near the surface.

Finally, the double layer of CN_x50%/a-C was examined (Fig. 3.53 c). The results come up to our expectation, the elements are well dispersed along the porous structure. The deeper areas are not deprived of the catalyst material as significant as in case of the a-C film, however, the places close to the surface have still the highest concentration of platinum and cerium.

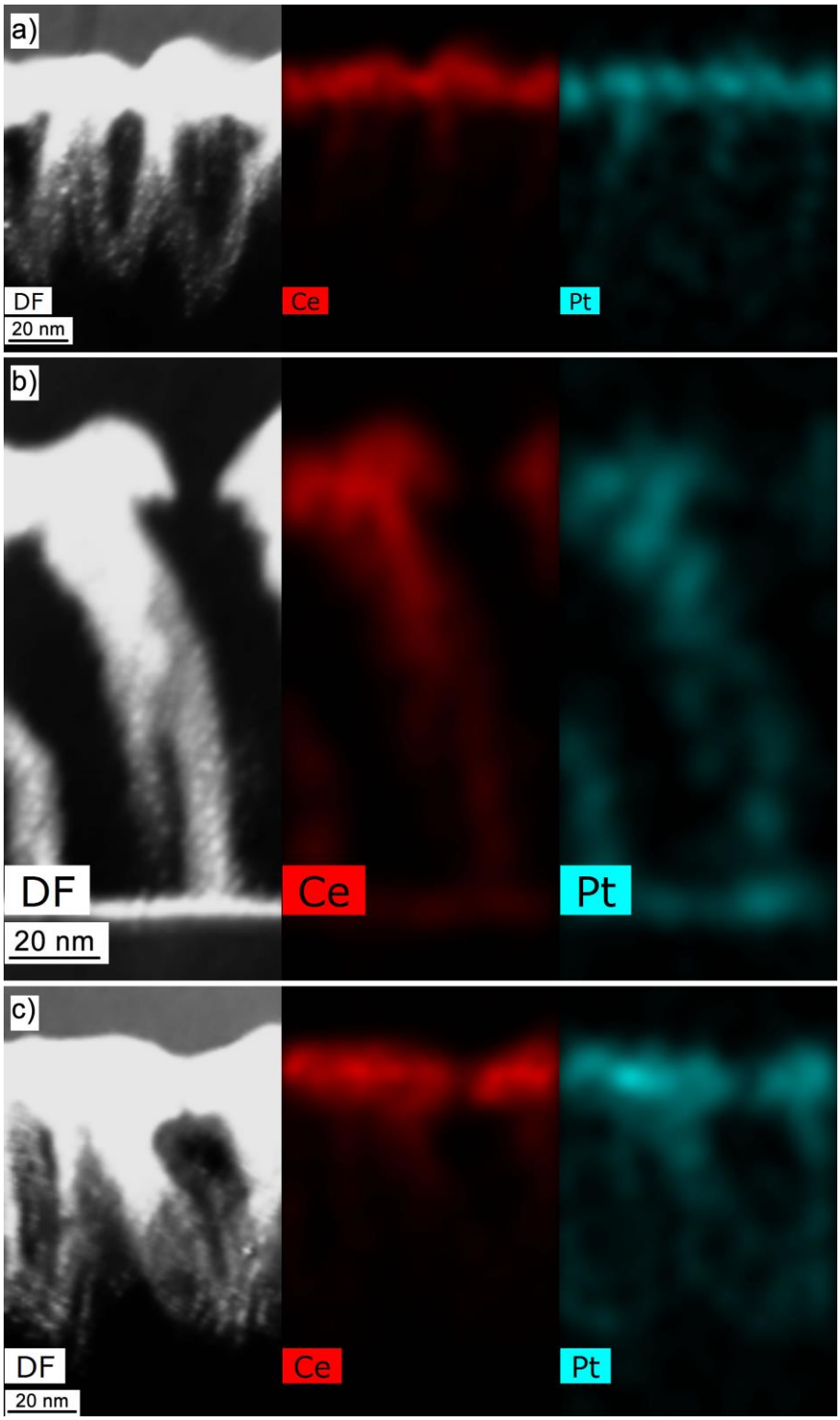

Fig. 3.53 Element maps of platinum and cerium obtained from EDX spectra acquired in each point of area displayed in corresponding STEM image. Pt2-CeO_x (20 nm)/a-C a), Pt2-CeO_x (20 nm)/CN_x100% b) and Pt2-CeO_x (20 nm)/CN_x50%/a-C c).

3.3.3.2 XPS Characterization

In order to study influence of platinum doping on chemical state of elements in catalyst layers, the XPS spectroscopy was performed on Pt-doped cerium oxide layer. For purpose to investigate changes of the catalyst layer composition due to the increasing Pt amount for different thicknesses of the deposited catalyst layers and varied porosity related to used catalyst support, the Ce 3d and Pt 4f spectra were acquired. Our attention is focused on cerium in 3+ and/or 4+ state and amount of platinum in metallic and/or ionic states.

Fig. 3.54 represents the XPS Ce 3d spectra measured on the 2 nm thick CeO_x catalyst layer doped by platinum with concentrations of 6, 16 and 28% prepared by Pt and CeO_2 co-deposition via magnetron sputtering on the 200 nm thick a-C film supported by silicon (samples labelling is in accordance with above mentioned, as Pt1-, Pt2- and Pt3-CeO_x/a-C). The spectra are present in ascending order concerning Pt concentration, i.e. the bottom black curve represents the Pt1-CeO_x layer, the very top curve the Pt3-CeO_x layer. An example of the decomposition of the Ce 3d spectrum to the Ce^{4+} and Ce^{3+} doublets according to Skala *et al.* work [88] is shown for the Pt1-CeO_x/a-C sample. As one can see, each spectrum consists of three $3d_{5/2}$–$3d_{3/2}$ spin–orbit-split doublets characteristic of the Ce^{4+} states which are a sign of stoichiometric cerium dioxide (CeO_2) and two doublets evidencing the formation of Ce^{3+} ions, thus the reduced cerium [86, 87]. From the shapes of the Ce 3d spectra in Fig. 3.54 one can see that the contribution of the Ce^{3+} states in comparison with Ce^{4+} ones is slightly increasing with Pt concentration. Such increase in signal of reduced cerium can be related with decreasing size of cerium oxide particles [60]. In a number of other studies [58-60], it was presented that the fraction of Ce^{3+} ions in cerium oxide particles rapidly increases with decreasing particle size because of the increasing amount of the oxygen vacancies. Therefore, we assume the relation between the Pt concentration, the particle size and the reduction of cerium. Moreover, reactions occurring during magnetron sputtering can lead to mixed oxide species $Ce^{3+}_{2-x}Pt^{2+}_xO_{3-\delta}$, where cerium is reduced [5].

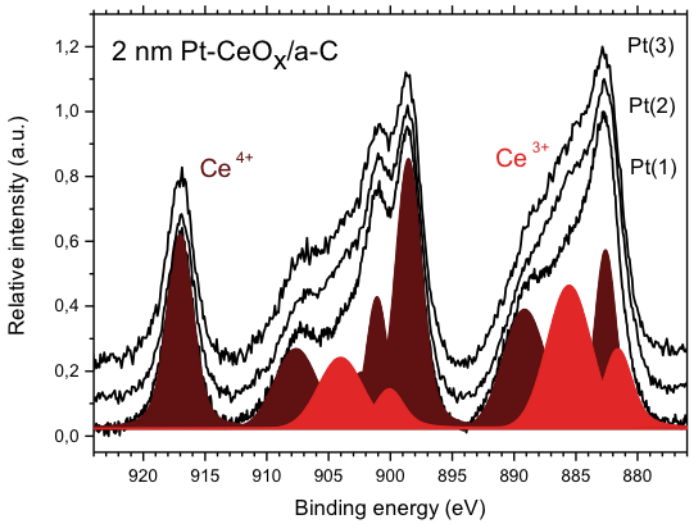

Fig. 3.54 XPS Ce 3d core level spectra of the 2 nm thick Pt1-, Pt2- and Pt3-CeO_x layers deposited on the a-C substrate (in ascending order). Red and brown colours represent contributions of the Ce^{3+} and Ce^{4+} states.

Similar investigation concerning changes in chemical composition were done for Pt 4f spectra. Fig. 3. 55 displayes XPS 4f spectra acquired for the 20 nm thick CeO_x catalyst layers doped by platinum with concentrations of 6, 16 and 28%. The spectra reveal Pt $4f_{7/2}$–$4f_{5/2}$ doublets at energies 72.7/76.0 eV and 74.4/77.7 eV, respectively. The first one can be associated with Pt^{2+} species (cyan curve) while the second corresponds to Pt^{4+} ions (blue curve) [97]. Observable increase in Pt^{4+} ions signal contribution is visible with increasing number of Pt wires used for the catalyst layer deposition, while concentration of Pt^{2+} ions is almost unchanged. Surprisingly, we did not acquire any signal corresponding to metallic Pt, not even for highest Pt concentration. Based on crystallography study, we can say that as metallic Pt particles were observed mostly in deeper areas of porous structures and XPS is a surface sensitive method, we are not able to "see" metallic platinum by this technique.

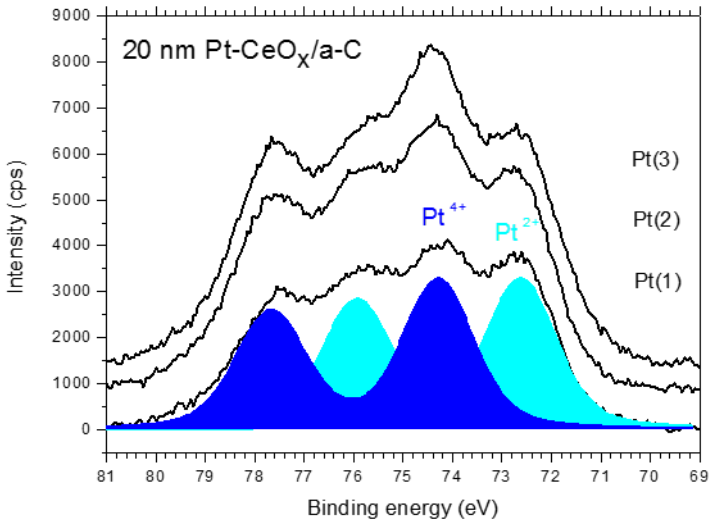

Fig. 3.55 XPS Pt 4f core level spectra of the 20 nm thick Pt1-, Pt2- and Pt3-CeO_x layers deposited on the a-C substrate (in ascending order). Cyan and blue colours represent the decomposition of the Pt 4f spectrum to Pt^{2+} and Pt^{4+} doublets.

In Fig. 3.56, an example of the Ce 3d spectra acquired on the Pt3-CeO_x (2 nm)/a-C sample for increasing amount of deposited calatytic material is presented. Similarly to the previously presented Ce 3d spectra, the decomposition of the Ce 3d spectrum to Ce^{4+} and Ce^{3+} doublets is shown for the 2 nm thick Pt3-CeO_x layer deposited on the a-C substrate. As it can be seen from the spectra shapes, the presence of reduced cerium oxide in very thin layer (2 nm) is suppressed with increasing thickness of the deposited layer, while Ce^{4+} signal is rising. The discussion concerning such behaviour is the same as for the non-doped cerium oxide layer deposited on C-foil (Fig. 3.40). With on-going deposition the small particles merge in bigger ones, which are less susceptible to oxygen vacancies formation and they are not affected more by interaction with the carbon substrate. The thicker layer is, the more stoichiometric cerium oxide can be seen by the XPS technique. It emerges also from the character of XPS method, which is very surface sensitive analysis with an information depth of about 1-5 nm. Therefore the signal originated from reduced layer close to catalyst-carbon support interface gives us very low contribution to the Ce 4d spectra.

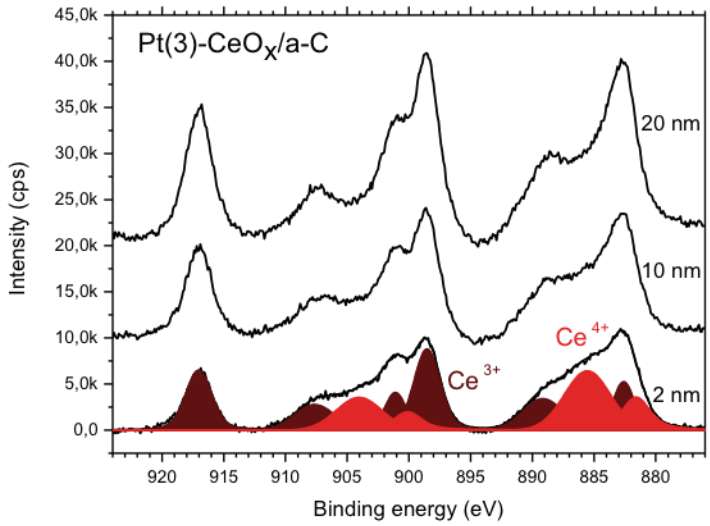

Fig. 3.56 XPS Ce 3d core level spectra of the 2, 10 and 20 nm thick Pt3-CeO_x layers deposited on the a-C substrate. Red and brown colours represent contributions of the Ce^{3+} and Ce^{4+} states.

The XPS analysis of the Pt3-CeO_x layer on the a-C substrate is accompanied by Pt 4f spectra presented in Fig. 3.57. As one can see in Fig. 3.57, the thin catalyst layer (2 nm) contents more Pt^{2+} ions than Pt^{4+}. With increasing amount of deposited layer, the amount of Pt^{4+} ions is increasing as well, while Pt^{2+} contribution remain almost static. The signal of Pt^{4+} prevails over the Pt^{2+} ones for the 20 nm thick Pt3-CeO_x layer. Such electronic state transition of platinum was observed in our previous studies [5, 98] and we can relate it with less porous and more continuous structure formation.

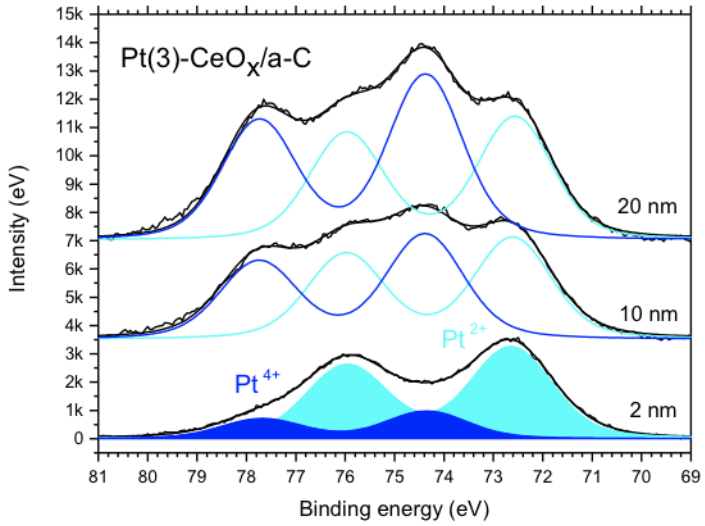

Fig. 3.57 XPS Pt 4f core level spectra of the 2, 10 and 20 nm thick Pt3-CeO_x layers deposited on the a-C substrate. Cyan and blue colours represent the decomposition of the Pt 4f spectrum to Pt^{2+} and Pt^{4+} doublets.

For comparison, the same study of chemical states of cerium and platinum was performed for the Pt3-CeO_x layer deposited on the silicon substrate. As it was shown in our previous work [5], the Pt-doped cerium oxide layer deposited on silicon grows as non-porous and continuous, contrary to ones prepared on the carbonaceous substrates. In addition, the EELS study present in Section 3.2.2.1 EELS Characterization has shown that the cerium oxide layer on silicon (Fig. 3.37 c) evinces the more stoichiometric character than on the a-C film (Fig. 3.37 a). A similar behaviour can be seen from comparison of Ce 3d spectra displayed in Fig. 3.58, where the Pt3-CeO_x/Si samples were investigated. Regardless the thickness of deposited layer, the cerium oxide is less reduced for the Si support than for the a-C substrate. It can be related to the less porous and more compact catalyst layer, as well as to the absence of cerium-carbon interaction. However, as it was mentioned before, in the case of the silicon support, the interaction between cerium oxide and silicon leads to the silicates and silicides formations [64, 65]. Their existence was confirmed by EELS and XPS spectroscopies.

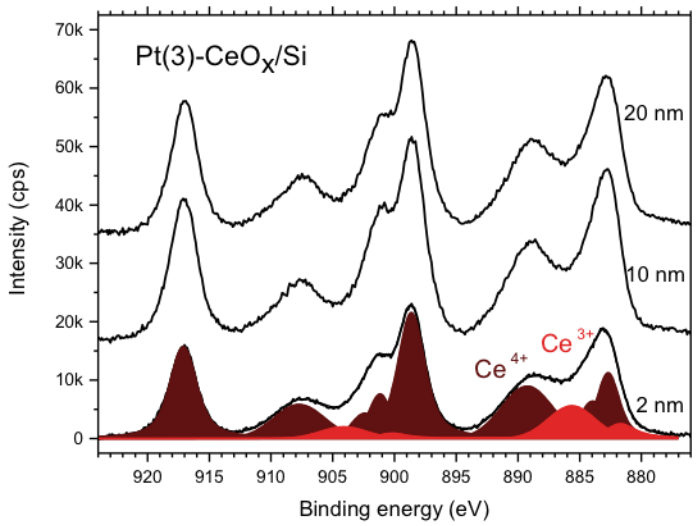

Fig. 3.58 XPS Ce 3d core level spectra of the 2, 10 and 20 nm thick Pt3-CeO_x layers deposited on the Si substrate. Red and brown colours represent contributions of the Ce^{3+} and Ce^{4+} states.

In order to complete the XPS study of Pt-doped CeO_x layers on the a-C and Si substrates, the Pt 4f spectra for the 2, 10 and 20 nm thick Pt3-CeOx layers deposited on the silicon support are displayed in Fig. 3.59. The spectra decomposition to Pt $4f_{7/2}$–$4f_{5/2}$ doublets associated with Pt^{2+} ions and Pt^{4+} ions is represented by cyan curve and blue curve, respectively. The signal associated with the presence of Pt^{2+} ions was acquired only for the 2 nm thick catalyst layer. For the thicker Pt3-CeO_x layers deposited on the Si substrate, Pt occurs solely in the Pt^{4+} state. Similarly, as in previous case, the Pt^{4+} formation is connected with less porous structure. It was shown in our previous studies [5, 98] that in cases of the 10 nm thick Pt-CeO_x catalyst layer on the silicon wafer and the carbonaceous substrate, the Pt occurs solely in Pt^{4+} state for the Si support, while mixture of Pt^{2+} and Pt^{4+} is present for the carbonaceous film. It is in good agreement with herein displayed results.

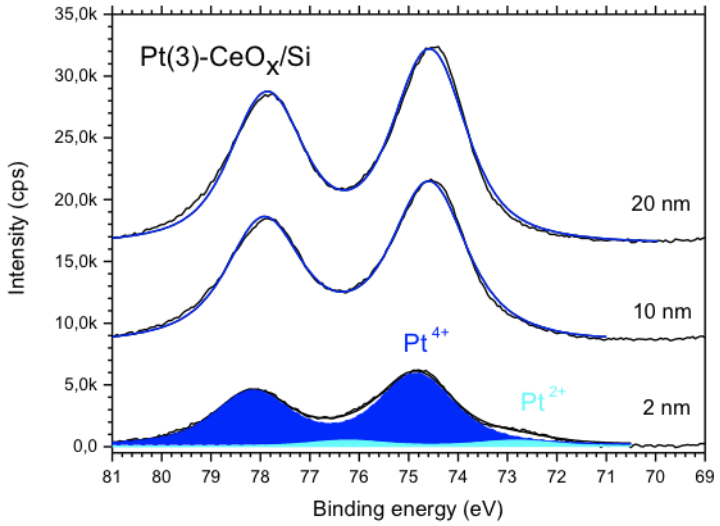

Fig. 3.59 XPS Pt 4f core level spectra of the 2, 10 and 20 nm thick Pt3-CeO_x layers deposited on the Si substrate. Cyan and blue colours represent the decomposition of the Pt 4f spectrum to Pt^{2+} and Pt^{4+} doublets.

However, while TEM crystallographic studies show us platinum in form of metallic clusters, we did not observe any signal corresponding to Pt^0 for the Si support, nor the a-C film. In case of thicker catalyst layers (10 and 20 nm), it can be explained by small information depth of the XPS technique. We have to note that all Pt nanonocrystals were observed in deeper areas of porous structure. Therefore, the XPS method cannot be able to detect signal originating from such places. For the 2 nm thick catalyst layer the amount of deposited material is not enough for platinum clusters formation. Therefore, other techniques as HRTEM imaging have to be used to obtain the more complete information about such complex catalyst system. Moreover, in our previous studies we have shown [5, 98, 99] that the Pt^{2+} ions are well dispersed on the surface region of porous catalyst layer, while Pt^{4+} ions are embedded in the bulk.

The EELS results are not shown, as the changes in cerium stoichiometry are negligible and the platinum signal is difficult to be acquired with our experimental device.

3.4 Catalyst Layer Application in PEMFC

Our investigation and obtained results presented in previous chapter led to the better understanding of processes occurring during the magnetron sputtering of catalyst layers on carbonaceous substrates and gave us a detailed knowledge about prepared system at nanoscale. Therefore, it allows us to shift the model studies to the real applications. The herein presented findings are focused on tuning the commercial catalyst support morphology by using nitrated carbonaceous films and thin film deposition. Such prepared catalyst is used and tested as an anode catalyst in PEMFC. The complex study including properties of Pt-CeO_x layers, durability tests and performance in fuel cell is the subject of a manuscript under preparation. Since the part concerning catalyst testing in FC devices is not the subject of this thesis the results are not included.

To increase the active area of an anode catalyst and to use platinum as efficient as possible, the commercial gas diffusion layer (GDL) composed from the macroporous carbon fibre paper coated with microporous amorphous carbon black (SGL TECHNOLOGIES GmbH, Sigratec GDL 25BC) in form of the small grains with size of 50-250 nm, called nanoGDL, was modified. The surface structure of such GDL can be seen in SEM image displayed in Fig. 3.60 a). In accordance with our morphology study presented in this thesis, the 100 nm thick CN_x50% film was deposited by magnetron sputtering on the surface of the nanoGDL support. The surface morphology of the nanoGDL after the CN_x50% film deposition is visible in Fig. 3.60 d). It is well seen that the carbon grains coated with carbon nitride reach bigger size than for uncoated ones; however, the surface area shows the original rounded features.

In order to compare the morphological changes after the Pt-CeO_x layer deposition, the SEM images of surfaces of the Pt-CeO_x (20 nm)/nanoGDL and Pt-CeO_x (20 nm)/CN_x50% (100 nm)/nanoGDL samples are shown in Fig. 3.60 b) and e), respectively. The Pt concentration is around 6%, as 1 Pt wire was used for magnetron co-sputtering. In case of the catalyst layer supported by the uncoated nanoGDL (Fig. 3.60 b), the changes are not very significant. The carbon grains seem less rounded with more pointed edges, indicating the carbon etching during the

magnetron sputtering process of the catalytic layer. Contrary, the differences between the nanoGDL coated by CN_x50% film before and after the Pt-CeO_x layer deposition are considerable. The well-rounded carbon particles are changed to the fractal-like structures (Fig. 3.60 e).

The TEM side-view images of the samples confirm the idea that the simultaneous carbon etching and material deposition have led to the porous structure formation during the magnetron sputtering process of the Pt-CeO_x layers. For the uncoated nanoGDL substrate, the grains of carbon black are only slightly modified. (Fig. 3.60 c). The structure is similar to the one formatted on the amorphous carbon film, presented in the model studies. In contrast, the extremely large surface area was achieved for the Pt-CeO_x (20 nm)/CN_x50% (100 nm)/nanoGDL system, as one can see in Fig. 3.60 f). It is visible that the porous structure is created mainly from the CN_x50% film with the grains of carbon black lying below. They play the role of the a-C layer, similar as in case of the model studies for the CN_x50%/a-C/Si support.

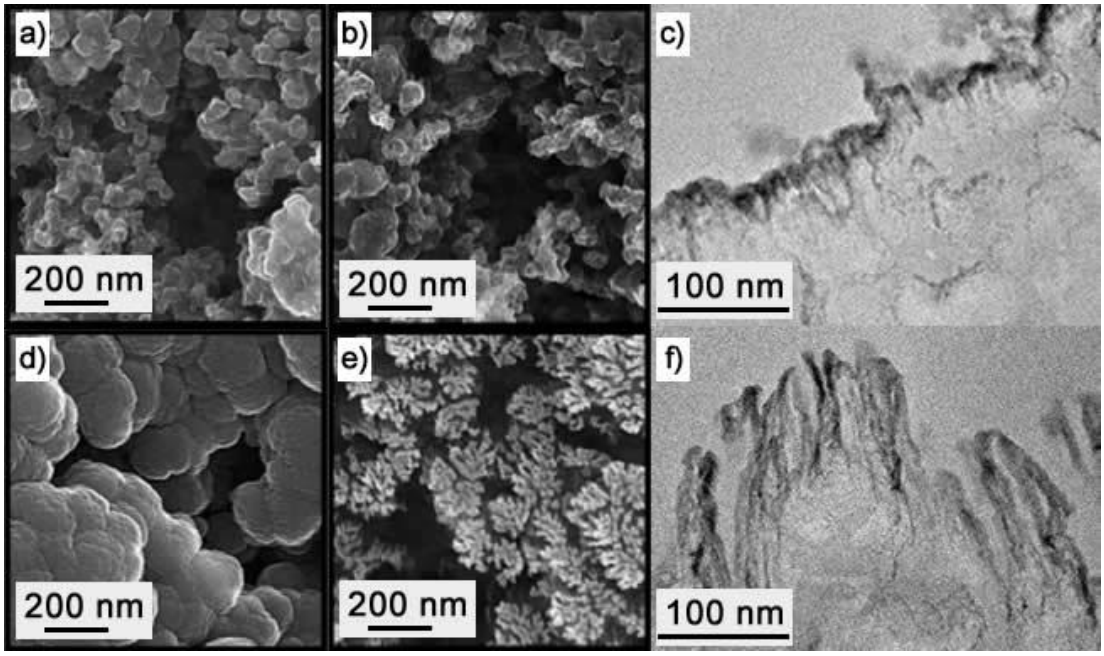

Fig. 3.60 The morphological changes caused by the CN_x film application on the nanoGDL and afterwards by the Pt-CeO_x sputtering. SEM images of the uncovered nanoGDL substrate a) and after the Pt-CeO_x layer deposition b), TEM side-view image of the Pt-CeO_x/nanoGDL system c). SEM images of the nanoGDL substrate coated by the CN_x50% film d) and after the Pt-CeO_x layer deposition e), TEM side-view image of the Pt-CeO_x/CN_x50%/nanoGDL system f).

The tuning of the commercial carbon support morphology by carbon nitride film for FC application is illustrated in Fig. 3.61. We propose to enlarge the surface area by applying the CN_x thin film on top of the nanoGDL support. The grains (carbon nanoparticles – CNP) reach bigger size; however, they are playing a role of the mask for further magnetron sputtering process. During the deposition of Pt-CeO_x catalyst layer, the simultaneous carbon etching by oxygen plasma and material deposition leads to the porous structure formation. The morphology can be tuned by changes in deposition parameters (time, rate, residual pressure) and/or by coating film composition. Hence, the final properties of the structure can be adapted for specific application. Moreover, our very recent results point not only at morphology tuning but also at the higher performance in fuel cells and the better stability during the durability tests for nanoGDL supports upgraded by CN_x films (not shown here).

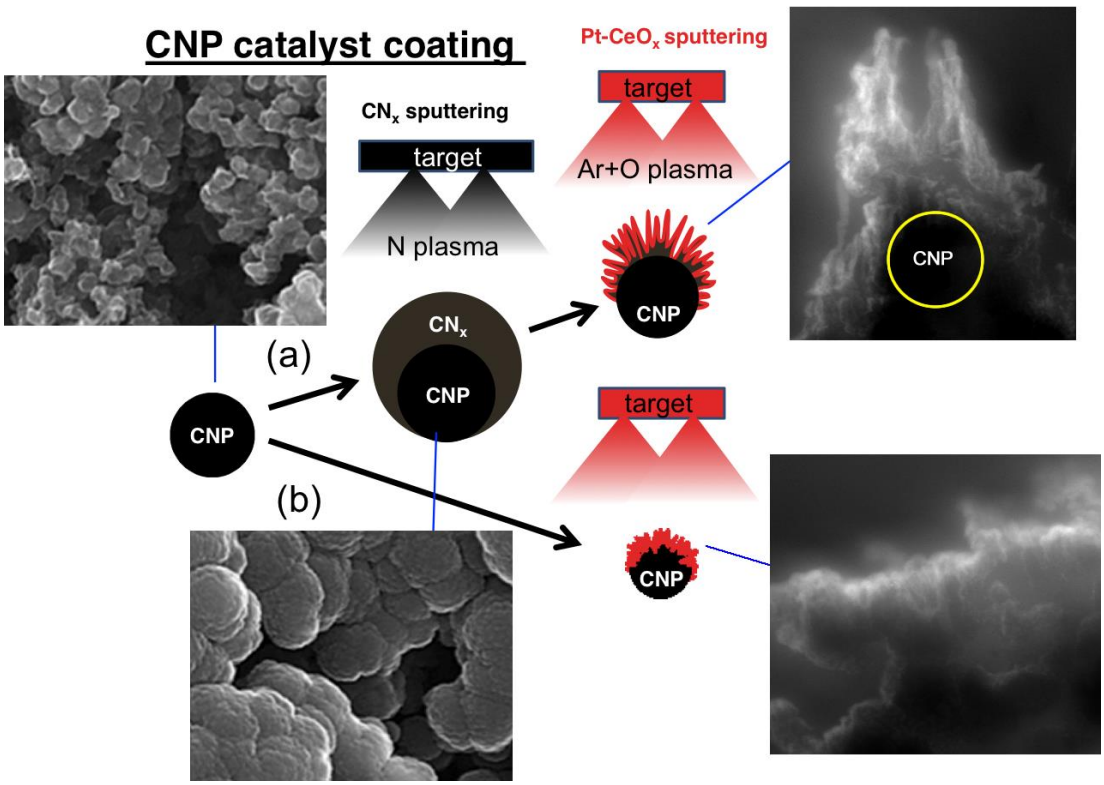

Fig. 3.61 Illustration of tuning the morphology of commercial catalyst support by CN_x thin film coating and further Pt-CeO_x catalyst layer deposition by magnetron sputtering.

Bibliography of Chapter 3.

[1] V. Matolin, I. Matolinova, M. Vaclavu, I. Khalakhan, M. Vorokhta, R. Fiala, I. Pis, Z. Sofer, J. Poltierova-Vejpravva, T. Mori, V. Potin, H. Yoshikawa, S. Ueda, K. Kobayashi, *Langmuir* 26 (2010) 12824.

[2] I. Matolinova, R. Fiala, I. Khalakhan, M. Vorokhta, Y. Sofer, H. Yoshikawa, K. Kobayashi, V. Matolin, *Appl. Surf. Sci.* 258 (2012) 2161.

[3] V. Matolin, M. Cabala, I. Matolinova, M. Skoda, M. Vaclavu, K.C. Prince, T. Skala, T. Mori, H. Yoshikawa, Y. Yamashita, S. Ueda, K. Kobayashi, *Fuel Cells* 10 (2010) 139.

[4] R. Fiala, I. Khalakhan, I. Matolinova, M. Vaclavu, M. Vorokhta, Y. Sofer, S. Huber, V. Potin, V. Matolin, *J. Nanosci. Nanotechnol.* 11 (2011) 5062.

[5] M. Vorokhta, I. Khalakhan, I. Matolinova, M. Kobata, H. Yoshikawa, K. Kobayashi, V. Matolin, *Appl. Surf. Sci.* 267 (2013) 119.

[6] I. Khalkhan, M. Dubau, S. Haviar, J. Lavkova, I. Matolinova, V. Potin, M. Vorokhta, V. Matolin, *Ceram. Int.* 39 (2013) 3765.

[7] V. Matolin, R. Fiala, I. Khalakhan, J. Lavkova, M. Vaclavu, M. Vorokhta, *Int. J. Nanotechnol.* 9 (2012) 680.

[8] Zs. Czigany, J. Neidhardt, I.F. Brunell, L. Hultman, *Ultramicroscopy* 94 (2003) 163.

[9] A.Z. Sadek, M. Kracica, A. Moafi, D.W.M. Lau, J.G. Partridge, D.G. McCulloch, *Diamond Relat. Mater.* 45 (2014) 58.

[10] M. Dubau, J. Lavkova, I. Khalakhan, S. Haviar, V. Potin, I. Matolinova, V. Matolin, *ACS Appl. Mater. Interfaces* 6 (2014) 1213.

[11] N. Hellgren, M.P. Johansson, E. Broitman, L. Hultman, J-E. Sundgren, *Phys. Rev. B* 59 (1999) 5162.

[12] J. Neidhardt, L. Hultman, *J. Vac.Sci. Technol. A* 25 (2007) 633.

[13] S. Muhl, J.M. Mendez, *Diamond Relat. Mater.* 8 (1999) 1809.

[14] L. Wan, R.F. Egerton, *Thin Solid Films* 279 (1996) 34.

[15] R. Kaltofen, T. Sebald, G. Weise, *Thin Solid Films* 290-291 (1996) 112.

[16] R. Kaltofen, T. Sebald, G. Weise, *Thin Solid Films* 308-309 (1997) 118.

[17] S. Haviar, M. Dubau, J. Lavkova, I. Khalakhan, V. Potin, V. Matolin, I. Matolinova, *Sci. Adv. Mater.* 6 (2013) 1278.

[18] A. Incze, A. Pasturel, C. Chatillon, *Surf. Sci.* 537 (2003) 55.

[19] V.G. Zavodinskii, E.A. Mikhailenko, *Combustion, Explosion, and Shock Waves* 42 (2006) 247.

[20] M.A. Baker, *Thin Solid Films* 69 (1980) 359.

[21] J.I. Paredes, A. Martinez-Alonso, J.M.D. Tascon, *Carbon* 38 (2000) 1183.

[22] N.M.D. Brown, N. Cui, A. McKinley, *Appl. Surf. Sci.* 133 (1998) 157.

[23] V. Philipps, G. Sergienko, A. Lyssoivan, H.G. Esser, M. Freisinger, A. Kreter, U. Samm, *J. Nucl. Mater.* 363-365 (2007) 929.

[24] H-X. You, N.M.D. Brown, K.F. Al-Assadi, *Surf. Sci.* 284 (1993) 263.

[25] M. Vinnichenko, R. Gago, H, Huang, Y.X. Leng, H. Sun, U. Kreissig, M.P.Kulish, M.F. Maitz, *Thin Solid Films* 455-456 (2004) 530.

[26] H.Y. Dai, X.R. Cheng, C.F. Wang, Y.C. Xue, Z.P. Chen, *Optik* 126 (2015) 861.

[27] J. Lavkova, I. Khalakhan, M. Chundak, M. Vorokhta, V. Potin, V. Matolin, I. Matolinova, *Nanoscale* 7 (2015) 4048.

[28] L. Jiang, A.G. Fitzgerald, M.J. Rose, A.M. Gundlach, R. Cheung, *Surf. Interface Anal.* 34 (2002) 728.

[29] I. Bertoti, M. Mohai, A. Toth, B. Zelei, *Nucl. Instr. and Meth. in Phys. Res. B* 148 (1999) 645.

[30] N. Mubumbila, B. Bouchet-Fabre, C. Godon, C. Marhic, B. Angleraud, P-Y. Tessier, T. Minea, *Diamond Relat. Mater.* 13 (2004) 1433.

[31] J. Robertson, *Mater. Sci. Eng. R* 37 (2002) 129.

[32] S.E. Rodil, S. Muhl, *Diamond Relat. Mater.* 13 (2004) 1521.

[33] C. Spaeth, M. Kuhn, F. Richter, U. Falke, M. Hietschold, R. Kilper, U. Kreissig, *Diamond Relat. Mater.* 7 (1998) 1727.

[34] J.C. Sanchez-Lopez, C. Donnet, F. Lefebvre, C. Fernandez-Ramos, A. Fernandez, *J. Appl. Phys.* 90 (2001) 675.

[35] N. Axen, G.A. Botton, R.E. Somekh, I.M. Hutchings, *Diamond Relat. Mater.* 5 (1996) 163.

[36] F. Alvarez, M.C. dos Santos, *J. Non-Cryst. Solids* 266-269 (2000) 808.

[37] B. Angleraud, N. Mubumbila, P.Y. Tessier, V. Fernandez, G. Turban, *Diamond Relat. Mater.* 10 (2001) 1142.

[38] A.K.M.S. Chowdhury, D.C. Cameron, M.S.J. Hashmi, *Surface Coatings and Technology* 112 (1999) 133.

[39] S. Lopez, H.M. Dunlop, M. Benmalek, G. Tourillon, M-S. Wong, W.D. Sproul, *Surf. Interface Anal.* 25 (1997) 315.

[40] D. Marton, K.J. Bpyd, A.H. Al-Bayati, S.S. Todorov, J.W. Rabalais, *Phys. Rev. Lett.* 73 (1994) 118.

[41] M.A. Baker, P. Hammer, *Surf. Interface Anal.* 25 (1997) 301.

[42] W.T. Zheng, H. Sjostrom, I. Ivanov, K.Z. Xing, E. Broitman, W.R. Salancek, J.E. Greene, J-E. Sundgren, *J. Vac. Sci. Technol. A* 14 (1996) 2696.

[43] F. Rossi, B. Andre, A. van Veen, P.E. Mijnarends, H. Schut, F. Labohm, M.P. Delplancke, H. Dunlop, E. Anger, *Thin Solid Films* 253 (1994) 85.

[44] W.J. Gammon, O. Kaft, A.C. Reilly, B.C. Holloway, *Carbon* 41 (2003) 1917.

[45] M. Barber, J.A. Connor, M.F. Guest, I.H. Hillier, M. Schwartz, M. Stacey, *Chem. Soc., Faraday Trans. 2* 69 (1973) 551.

[46] I. Gouzman, R. Brener, A. Hoffman, *Surf. Sci.* 331-333 (1995) 283.

[47] L. Jiang, A.G. Fitzgerald, M.J. Rose, R. Cheung, B. Rong, E. Van der Drift, *Appl. Surf. Sci.* 193 (2002) 144.

[48] R.W.G. Wyckoff, Crystal Structures, *Interscience Publishers*, New York, USA, (1963), ISBN 978-0898743876.

[49] W.H. Zachariasen, *Z. Phys. Chem.* 123 (1926) 134.

[50] E.A. Kummerle, G, Heger, *J. Solid State Chem.* 147 (1999) 485-500.

[51] Crystalography database, available online www.crystallography.net

[52] P.A. Stadelmann, *Ultramicroscopy* 21 (1987) 131.

[53] H. Wilkens, O. Schuckmann, R. Oelke, S. Gevers, A. Schaefer, M. Baumer, M.H. Zoellner, T. Schroeder, J. Wollschlager, *Appl. Phys. Lett.* 102 (2013) 111602.

[54] M. Atoji, *Phys. Lett.* 22 (1966) 21.

[55] T. Sakai, G. Adachi, J. Shiokawa, *Mat. Res. Bull.* 15 (1980) 1001.

[56] B-B. Liu, G-T. Zou, H-B. Yang, S. Yu, J-S. Lu, Z-Y. Liu, S-Y. Liu, W-G. Xu, *J. Phys. Chem. Soilds* 58 (1997) 1873.

[57] Ch. Loschen, A. Migani, S.T. Bromley, F. Illas, K.M. Neyman, *Phys. Chem. Chem. Phys.* 10 (2008) 5730.

[58] L. Wu, H.J. Wiesmann, A.R. Moodenbaugh, R.F. Klie, Y. Zhu, D O. Welch, M. Suenaga, *Phys. Rev. B* 69 (2004) 125415.

[59] F. Zhang, P. Wang, J. Koberstein, S. Khalid, S-W. Chan, *Surf. Sci*. 563 (2004) 74.

[60] S. Tsunekawa, T. Fukuda, A. Kasuya, *Surf. Sci.* 457 (2000) L437.

[61] R. Vidhya, M.P. Antony, P.R. Vasudeva Rao, B. Viswanathan, *J. Nucl. Mater.* 317 (2003) 102.

[62] H. Wilkens, O. Schuckmann, R. Oelke, S. Gevers, A. Schaefer, M. Baumer, M.H. Zoellner, T. Schroeder, J. Wollschlager, *Appl. Phys. Lett.* 102 (2013) 111602.

[63] P. Knappe, L. Eyring, *J. Solid State Chem.* 58 (1985) 312.

[64] V. Potin, J.Lavkova, S. Bourgeois, M. Dubau, I. Matolinova, V. Matolin, *Mater. Today: Proc.* 2 (2015) 101.

[65] T. Skala, V. Matolin, *Appl. Surf. Sci.* 265 (2013) 817.

[66] S. Yang, L. Gao, *J. Am. Chem. Soc.* 128 (2006) 9330.

[67] S. Turner, S. Lazar, B. Freitag, R. Egoavil, J. Verbeeck, S. Put, Y. Strauven, G. van Tendeloo, *Nanoscale* 3 (2011) 3385.

[68] Ch. Loschen, S.T. Bromley, K.M. Neyman, F. Illas, *J. Phys. Chem. C* 111 (2007) 10142.

[69] S.T. Bromley, I. de P.R. Moreira, K.M. Neyman, F. Illas, *Chem. Soc. Rev.* 38 (2009) 2657.

[70] A. Migani, K.M. Neyman, S.T. Bromley, *Chem. Commun.* 48 (2012) 4199.

[71] A. Migani, G. N. Vayssilov, S.T. Bromley, F. Illas, K.M. Neyman, *J. Mater. Chem.* 20 (2010) 10535.

[72] T.X.T. Sayle, S.C. Parker, D.C. Sayle, *Chem. Commun.* (2004) 2438.

[73] U.M. Bhatta, I.M. Ross, T.X.T. Sayle, D.C. Sayle, S.C. Parker, D. Reid, S. Seal, A. Kumar, G. Mobus, *ACSNano* 6 (2012) 421.

[74] A. Bruix, Y. Lykhach, I. Matolinova, A. Neitzel, T. Skala, N. Tsud, M. Vorokhta, V. Stetsovych, K. Sevcikova, J. Myslivecek, K.C. Prince, Stephanie Bruyere, V. Potin, F. Illas, V. Matolin, J. Libuda, K.M. Neyman, *Angew. Chem.-Int. Ed.* 53 (2014) 10525.

[75] F. Dvorak, M.F. Camellone, A. Tovt, N-D. Tran, F-R. Negreiros, M. Vorokhta, T. Skala, I. Matolinova, J. Myslivecek, V. Matolin, S. Fabris, *Nat. Commun.* 7 (2016) 10801.

[76] Gatan Inc., Digital Micrograph, www.gatan.com

[77] H. Xu, Y. Wang, *J. Nucl. Mater.* 266 (1999) 117.

[78] S.R. Gilliss, J. Bentley, C.B. Carter, *App. Surf. Sci.* 241 (2005) 61.

[79] D.R. Mullins, S.H. Overbury, D.R. Huntley, *Surf. Sci.* 409 (1998) 307.

[80] M. Song, W. Weiguo, F. Chu, X. Yang, K. Mitsuishi, K. Furuya, H. Yasuda, *Nucl. Instrum. Methods Phys. Res., Sect. B* 191 (2002) 586.

[81] R. Wang, S.I. Mutinda, *Chem. Phys. Lett.* 517 (2011) 186.

[82] L.A. Giannuzzi, F.A. Stevie, *Micron* 30 (1999) 197.

[83] S. Rubanov, P.R. Munroe, *J. Microsc.* 214 (2004) 213.

[84] N.I. Kato, *J. Electron Microsc.* 52 (2004) 451.

[85] L.A.J. Garvie, P.R. Buseck, *J. Phys. Chem. Solids* 60 (1999) 1943.

[86] M. Romeo, K. Bak, J. El Fallah, F. Le Normand, L. Hilaire, *Surf. Interface Anal.* 20 (1993) 508.

[87] P. Patsalas, S. Logothetidis, L. Sygellou, S. Kennou, *Phys. Rev. B*, 68 (2003) 035104.

[88] T. Skala, F. Stutara, K.C. Prince, V. Matolin, *J. Electron Spectrosc. Relat. Phenom.* 169 (2009) 20.

[89] A.E. Dwight, *Trans ASM* 53 (1961) 479.

[90] D.T. Adroja, S.K. Malik, B.D. Padalia, R. Vijayaraghavan, *Solid State Commun.* 71 (1989) 649.

[91] A. Janghorban, M. Lomello-Tafin, J.M. Moreau, Ph. Galez, *Intermetallics* 18 (2010) 2208.

[92] A. Schroder, R. van den Berg, H.v. Lohneysen, W. Paul, H. Lueken, *Solid State Commun.* 65 (1988) 99.

[93] G-F. von Blackenhagen, M. Lenkewitz, G.R. Stewart, *J. Alloys and Compd.* 261 (1997) 37.

[94] C. Praetorius, M. Zinner, A. Kohl, H. Kiesling, S. Bruck, B. Muenzing, M. Kamp, T. Kachel, F. Choueikani, P. Ohresser, F. Wilhelm, A. Rogalev, K. Fauth, *Phys. Rev. B* 92 (2015) 045116.

[95] J. Kemmer, C. Praetorius, A. Kronlein, P-J. Hsu, K.Fauth, M. Bode, *Phys. Rev. B* 90 (2014) 195401.

[96] P. Tereshchuk, M.J. Piotrowski, J.L.F. Da Silva, *RSC Adv.* 5 (2015) 521.

[97] L. Osterlund, S. Kielbassa, C. Werdinius, B. Kasemo, *J. Catal.* 215 (2003) 94.

[98] H. Yosikawa, I. Matolinova, V. Matolin, *J. Electron Spectrosc. Relat. Phenom.* 190 (2013) 268.

[99] M. Vaclavu, I. Matolinova, J. Myslivecek, R. Fiala, V. Matolin, *J. Electrochem. Soc.* 156 (2009) B938.

Conclusion

The present work was focused on the study of anode catalyst material for fuel cell application based on Pt-doped CeO_x layers deposited on carbonaceous substrates. The investigation concerning morphology, structure and composition of the catalyst and the catalyst support was performed by electron microscopies and complementary spectroscopies. It was shown that by suitable combination of deposition conditions, we are able to tune catalyst morphology and to obtain very porous structure with high surface area. Simultaneously, porosity of such prepared layers is related with their composition. We have shown that more porous layers evince smaller and better-dispersed crystallites, which can be a determining factor for fuel cell activity. Herein proposed system of Pt-CeO_x/CN_x was applied on commercial GDL used as a catalyst support. Possibility of active surface area enlargement was shown.

The partial results led to better understanding of the studied system nature. We have shown that composition of carbonaceous support has significant impact on formation of final structure. Thin films of amorphous carbon and carbon prepared in nitrogen atmosphere by magnetron sputtering were studied and compared. Obtained results allow us to conclude that the higher amount of nitrogen in working atmosphere leads to higher nitrogen concentration in prepared films, however it is not exceeding 30%. As a consequence of nitrogen enrichment, lower resistance to oxygen plasma etching was demonstrated. Hence, this nature of nitrogenated cafrom films was responsible for extremely porous structure formation during CeO_x layers deposition.

In fact, the key aspect discussed in this thesis was the influence of several factors causing morphological changes of prepared catalyst layers. The deposition time of CeO_x layers, the deposition rate and the composition of working atmosphere during magnetron sputtering were considered as the most important. In brief, the more continuous layer can be achieved by longer and faster deposition of cerium oxide. Dependence on partial oxygen pressure in working chamber was not linear

and some equilibrium had to be found. By considering all these aspects, it was concluded that two main processes were occurring simultaneously during the magnetron sputtering: deposition of cerium oxide and oxygen plasma etching of carbon. The main steps of the mechanism can be described as follows: at the early stage of growth, small amount of cerium oxide sputtered on carbonaceous substrate forms fine grainy and non-continuous structure. These grains are resistant to oxygen plasma etching and play a role of shielding mask for underlying carbon. With on-going process, unprotected parts of carbon are exposed to oxygen plasma, which leads to volatile carbon oxides formation (CO and CO_2) and/or nitrogen oxides and carbides (NO, CO_2, CN) giving rise to surface erosion. Further deposition process deepens carbon hollows, while deposited cerium oxide merges to caps atop. It leads to hilly-like structure formation. Based on these findings, we proposed the growth model for CeO_x layers on carbonaceous substrates.

Morphology studies were completed by crystallographic investigation, which pointed out to CeO_2 and Ce_7O_{12} crystallites formation. Surprisingly, numerous crystals were identified as CeC_2 without any doubt. It demonstrates cerium-carbon interaction during sample elaboration, as they were located close to the catalyst-support interface. Crystal size was related to the amount of deposited material and porosity of structure. By HRTEM, the cerium oxide crystals in octahedral shape proposed by DFT calculation was observed. Nevertheless, their occurrence was rare. Therefore, our attention was focused on {111} planes truncated by {100} nanofacets suggested as favourable places for Pt adsorption.

View on electronic state of cerium was given by EELS and XPS spectroscopies. In case of EELS, cross-sectional samples in form of thin lamellas were investigated in order to obtain local information. It was shown that cerium reduction is closely related to the cerium-carbon interaction, the type of the catalyst support, porosity and the thickness of CeO_x layers, as well as the crystals size. Susceptibility of cerium oxide for oxygen vacancies formation in context of particle size and their localization was discussed. The results were confirmed by XPS technique; however, we have to note that this method has an integral character of surface science analysis with relatively low information depth. Complementary EELS and XPS studies allowed us to complete herein proposed model of growth by electronic state of cerium, which is more reduced close to the carbon film and becomes stoichiometric moving to upper parts of the structure.

Knowledge of CeO_x/carbon system allowed us to study such prepared layers doped by platinum. The main emphasis was placed on morphological and structural changes caused by Pt-doping. Although no significant changes in morphology were not observed for the a-C and CN_x100% supports, slight influence was identified in case of the double-layer composition of CN_x50%/a-C film. With increasing Pt concentration, covering of the carbonaceous substrate by the deposited material was increasing as well, and therefore, carbonaceous substrate etching by oxygen plasma was suppressed. In contrast, the increase in Pt concentration had significant influence on crystals size, as more platinum doping was linked to smaller sizes of crystallites. In addition, metallic Pt particles were pointed out in deeper areas of formed structures, while Pt-Ce alloys were observed on the top. Based on EDX spectroscopy, it was shown that distribution of elements in catalyst layers is not homogeneous through the structure. However, XPS spectroscopy is suitable for very thin layers and surface observation. Thus, electron state of cerium and platinum was examined depending on Pt concentration, layer thickness and catalyst support. The results pointed out that presence of Pt^{2+} ions is connected with higher porosity of catalyst layers.

Finally, we took advantage gained knowledge and applied Pt-CeO_x/CN_x system on commercial nanoGDL used as a catalyst support. Possibility of an active surface area enlargement of the prepared catalyst layers was shown. Our very recent results have shown higher performance of these Pt-CeO_x/CN_x catalyst layers in fuel cell and better stability during durability tests. These systems are still under investigation and results will be published.

List of Figures

List of Tables

List of Abbreviations

ADF	Annular Dark Field
AEM	Analytical Electron Microscopy
AFC	Alkaline Fuel Cell
AFM	Atomic Force Microscopy
BF	Bright Field
BSE	Backscattered electron
CCD	Charge-Coupled Device
CDF	Central Dark Field
DC	Direct Current
DF	Dark Field
DFT	Density Functional Theory
DM	Digital Micrograph
DMCF	Direct Methanol Fuel Cell
EBID	Electron beam-induced deposition
EDX	Energy Dispersive X-ray spectroscopy
EELS	Electron Energy Loss Spectroscopy
FC	Fuel Cell
FEG	Field Emission Gun
FFP	Front-focal Plane
FFT	Fast Fourier Transformation
FIB	Focused Ion Beam
GIF	Gatan Imaging Filter
GIS	Gas Injection System
GDL	Gas Diffusion Layer
HRTEM	High Resolution Transmission Electron Microscopy
IBID	Ion beam-induced deposition
JEMS	Java Electron Microscopy Software
LMIS	Liquid-metal Ion Source
MCFC	Molten Carbonate Fuel Cell

MEA	Membrane Electrode Assembly
PAFC	Phosphoric Acid Fuel Cell
PEM	Proton Exchange Membrane
PEMFC	Proton Exchange Membrane Fuel Cell
RF	Radio Frequency
SE	Secondary Electron
SEM	Scanning Electron Microscopy
SI	Secondary Ion
SOFC	Solid Oxide Fuel Cell
STEM	Scanning Transmission Electron Microscopy
TEM	Transmission Electron Microscopy
UHV	Ultra High Vacuum
UHR	Ultra High Resolution
XPS	X-ray Photoelectron Spectroscopy